GAS-LIQUID FLOWS IN ADSORBENT MICROCHANNELS

A Thesis
Presented to
The Academic Faculty

By

Bryce Moore

In Partial Fulfillment
Of the Requirements for the Degree
Master of Science in Mechanical Engineering

Georgia Intitute of Technology

May 2013

GAS-LIQUID FLOWS IN ADSORBENT MICROCHANNELS

Approved by:

Dr. Srinivas Garimella, Adviser
G.W. Woodruff School of Mechanical Engineering
Georgia Institute of Technology

Dr. S. Mostafa Ghiaasiaan
G.W. Woodruff School of Mechanical Engineering
Georgia Institute of Technology

Dr. Sheldon Jeter
G.W. Woodruff School of Mechanical Engineering
Georgia Institute of Technology

Date Approved: 11/12/2012

DEDICATION

To my family

ACKNOWLEDGEMENTS

I would like to thank my adviser, Dr. Garimella, for his support and instruction though the process of this work. I would also like to thank the Exxon-Mobil corporation, who provided funding and support, and the members of the Sustainable Thermal Systems Laboratory, in particular Thomas Robbins, Brendon Keinath, Anand Nagavarapu, Adrienne Little, Darshan Pahinkar, and Sampath Kommandur, all of whom contributed to this study and this thesis.

Finally, I would like to thank my committee members, Dr. Sheldon Jeter and Dr. Seyed Mostafa Ghiaasiaan, who provided guidance in the course of this work.

TABLE OF CONTENTS

LIST OF TABLES

LIST OF FIGURES

LIST OF SYMBOLS AND ABBREVIATIONS

Symbols

A	Area [m^2]
Bo	Bond number [-]
C	Mole fraction [mol mol^{-1}]
c	Concentration [mol m^{-3}]
c_p	Specific heat [kJ kg^{-1} K^{-1}]
D	Diameter [m]
f	Friction factor [-]
g	Gravity [m s^{-2}]
H	Height [m]
L	Length [m]
k	Thermal conductivity [W m^{-1} K^{-1}]
m	Mass [kg]
M	Molar mass [kg kmol^{-1}]
N	Number of nodes [-]
P	Pressure [Pa]
Per	Perimeter [m]
$\dot{Q}'''$	Heat generation [W m^{-3}]
R	Mass transfer resistance [s m^{-1}]
R_U	Gas constant [J kg^{-1} K^{-1}]
Re	Reynolds number [-]
$\dot{S}'''$	Mass transfer source term [mol m^{-3} s^{-1}]
t	Time [s]
T	Temperature [K]
U	Uncertainty [-]
v	Velocity [m s^{-1}]
V	Volume [m^3]
We	Weber number [-]
x	Position [m]
X	Mass fraction [kg kg^{-1}]
X_{tt}	Martinelli parameter [-]

Greek

α	Void fraction [-]

Δ	Change or discrete step [-]
δ	Thickness [μm]
ε	Adsorbent layer void fraction [-]
μ	Viscosity [kg m^{-1} s^{-1}]
ρ	Density [kg m^{-3}]
σ	Surface tension [Pa m] or standard deviation [-]
θ	Angle [rad]
ω	Mass fraction of adsorbent in the wall [-]

Superscripts and Subscripts

A	Species A
ads	Adsorption
c	Cross-sectional
crit	Critical
cond	Conduction
conv	Convection
EQ	Equivalent
G	Gas phase
h	Hydraulic
i	Spatial step index
in	Inlet
L	Liquid phase
m	Mass transfer coefficient
out	Outlet
prev	Previous iteration
s	Surface
S	Superficial
t	Time step index
T	Heat transfer coefficient
TOT	Total
w	Wall

SUMMARY

A study of two the sequential displacement of gas and liquid phases in microchannels for eventual application in temperature swing adsorption (TSA) methane purification systems was performed. A model for bulk fluid displacement in 200 μm channels was developed and validated using data from an air-water flow visualization study performed on glass microchannel test sections with a hydraulic diameter of 203 μm. High-speed video recording was used to observe displacement samples at two separate channel locations for both the displacement of gas by liquid and liquid by gas, and for driving pressure gradients ranging from 19 to 450 kPa m^{-1}. Interface velocities, void fractions, and film thicknesses were determined using image analysis software for each of the 63 sample videos obtained.

The bulk fluid displacement models for fluid velocity were found to be in good agreement with experimental results for the displacement of gas by liquid, with a mean absolute error of 11%. For this displacement case, 90% of the predicted interface velocities are within 20% of the experimentally observed values. For the displacement of liquid by gas, the mean model error was 20%. In this case, only 64% of the predicted data points are within 20% of the experimental values. This lower model accuracy for the displacement of liquid is attributed to the presence of several different flow patterns at the liquid-gas interface.

The flow patterns observed during the displacement of liquid by gas were dry-wall, thin-film, ring-film, intermittent, and rivulet flows. During the displacement of gas by liquid, only one flow pattern was observed, in which a single liquid slug cleanly

displaced the gas in the channel with little interaction at the liquid-gas interface. For each test case, spatially-averaged and centerpoint liquid film thicknesses for the recorded frame were measured at 50 millisecond intervals over a 1 second time interval following displacement. Liquid films were observed with thicknesses as large as 30 µm. Film thickness data exhibit considerable scatter, and no patterns or trends were discernible beyond initial displacement. Immediately after displacement, the film thickness data were more coherent, but also did not exhibit trends amenable to physically based correlations. It was found that to ensure a dry channel wall after displacement, which would provide optimal conditions for mass transfer in an actual adsorption system, the maximum allowable interface velocity would be 0.16 m s^{-1}.

Coupled 2-D heat and mass transfer models were developed to simulate a TSA gas separation process in which impurities in the gas supply were removed through adsorption into adsorbent coated microchannel walls. These models were used to evaluate the impact of residual liquid films on system mass transfer during the adsorption process. Continuous annular liquid films thicker than 1 µm were found to have a significant detrimental impact on system mass transfer, and liquid films greater than 5 µm were found to decrease pure methane output by more than 85%. It was determined that the presence of liquid rivulets on the channel wall is preferable to the presence of continuous films, and that in the case of rivulet flow, mass transfer performance is less sensitive to film thickness. It was determined that rivulet flow will preserve the mass transfer performance of the channel even in the presence of large amounts of residual liquid, with a 10 µm film covering 50% of the channel causing only a 4.4% reduction in purified methane output.

It was determined that for a TSA methane purification system to be effective, it is necessary to purge liquid from the adsorbent channel. This intermediate purge phase will benefit the mass transfer performance of the adsorption system by removing significant amounts of residual liquid from the channel and by causing the onset of rivulet flow in the channel. The existence of the remaining dry wall area, which is characteristic of rivulet flow, improves system mass transfer performance in the presence of residual liquid.

The commercial viability of microchannel TSA gas separation systems depends strongly on the ability to mitigate the presence and effects of residual liquid in the adsorbent channels. While the use of liquid heat transfer fluids in the microchannel structure provides rapid heating and cooling of the adsorbent mass, the management of residual liquid remains a significant hurdle. In addition, such systems will require reliable prevention of interaction between the adsorbent and the liquid heat transfer fluid, whether through the development and fabrication of highly selective polymer matrix materials or the use of non-interacting large-molecule liquid heat transfer fluids. If these hurdles can be successfully addressed, microchannel TSA systems may have the potential to become a competitive technology in large-scale gas separation.

CHAPTER 1

INTRODUCTION

Investigations of multiphase flow in small-diameter tubes have been largely driven by interest in the design of compact heat exchangers for highly efficient heating and cooling systems. However, the same characteristics that make microchannel geometries desirable for these applications, namely large surface area for heat and mass transfer and high heat and mass transfer coefficients, also make them potential candidates for use in temperature-swing adsorption (TSA) gas separation applications. This work investigates the use of microchannels as heat and mass exchangers in a TSA system designed for the purification of methane gas.

Adsorption-based gas separation systems rely on preferential attraction between gas mixture components and chemical groups on solid surfaces, as well as the ability to cyclically manipulate the thermodynamic state of the system. These processes are actuated by varying the system pressure, temperature, or both to selectively adsorb and desorb mixture components. Pressure-swing adsorption (PSA) processes achieve this selective adsorption and desorption of gas mixture components by manipulating the pressure of the gas mixture in the adsorbent region; increasing the system pressure increases the adsorbed equilibrium concentration of the target gases, and vice versa. TSA processes achieve the same effects by varying the system temperature; however, the rapid heating and cooling of adsorbent beds has proven to be difficult due to the low effective thermal conductivity of adsorbent materials. As a result, TSA systems have not been actively considered for industrial gas separations, which currently favor pressure-swing adsorption (PSA), absorption, or membrane diffusion separation methods (Aaron and Tsouris, 2011). However the incorporation of adsorbent-laden microchannels as an alternative to the traditional packed bed adsorbent configuration has the potential to greatly improve the heat transfer performance of these systems. Commercially viable large-scale TSA systems may be possible through the use of microchannels for heat transfer enhancement.

One potential implementation of microchannels in adsorption-based gas separation uses adsorbent-coated microchannels with diameters on the order of 200 µm, arranged as in Figure 1.1. Feed gas flows through these channels, allowing gaseous contaminants to be removed via adsorption. Temperature swings are provided by the flow of hot or cold liquid through adjacent microchannels; heat exchange between the liquid and the adsorbent occurs via conduction through the channel walls. Such a gas and liquid microchannel system can be fabricated in monolithic arrays containing thousands of channels.

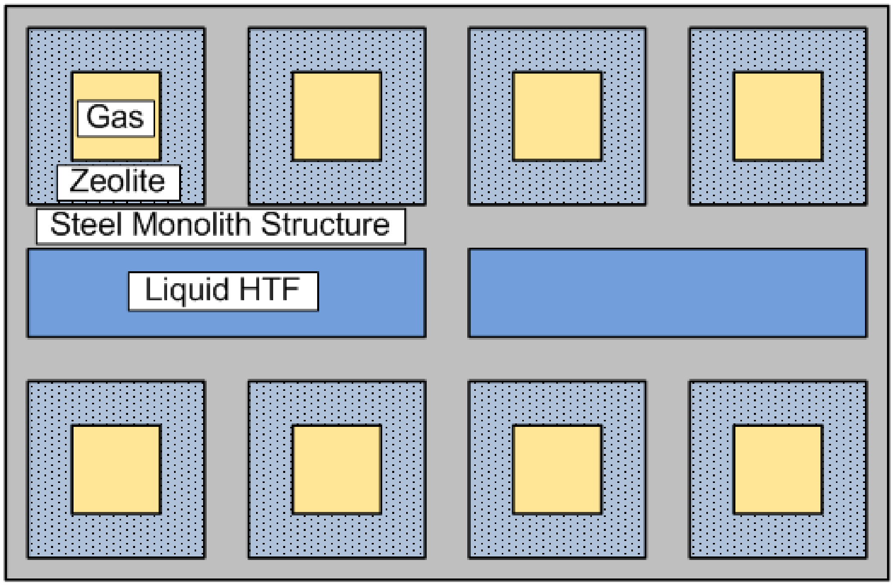

Figure 1.1: One potential implementation of a microchannel-based monolithic adsorption system.

This system can provide improved heat transfer performance compared to heat conduction through large adsorbent beds, but suffers from several key drawbacks. First, the need for separate channels for gas and liquid lead to a large system footprint for the total adsorbent loading capacity, especially compared to the relatively compact nature of packed bed PSA systems. In addition, fabrication of the channel monoliths is challenging due to the need to selectively plumb thousands of sub-millimeter channels for their respective fluid streams. Finally, while heat transfer performance is improved through the use of microchannels, significant heat transfer resistances still exist due to the need to conduct heat through the channel walls. Ultimately, this results in slow mass transfer and poor system performance compared to PSA systems.

The TSA system under consideration in the present study addresses these limitations through the use of dual-use adsorbent channels arranged in monolithic blocks. In this design, the feed gas mixture and the liquid heat transfer fluid are conveyed alternately through the same adsorbent microchannels, eliminating the need for dedicated gas and liquid channels. In this process, gaseous contaminants are removed from the feed mixture by passing this mixture through microchannels lined with an adsorbent material. A diagram of such a channel is shown in Figure 1.2. The process consists of the following steps:

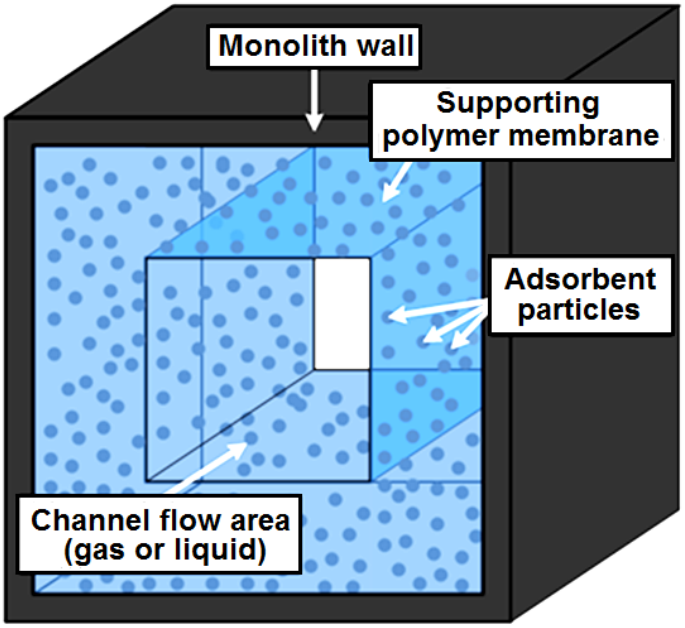

Figure 1.2: Diagram of the adsorbent-laden channels under consideration in the present study.

Step 1 – Adsorption: Feed gas composed of a $CH_4/CO_2/H_2S$ mixture is passed through the microchannels in the axial direction, allowing the gas mixture to diffuse into the polymer region. H_2S and CO_2 are removed via kinetic separation and adsorption onto the surfaces and pores of the zeolite particles embedded in the polymer. Purified methane is captured at the channel outlet. The high mass transfer coefficients in the channel create a sharp front of adsorbed concentration that progresses axially in the co-current direction. When this concentration front nears the channel outlet, the effluent purity decreases and the flow of feed gas is cut off.

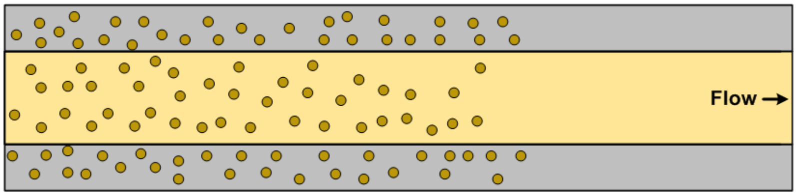

Figure 1.3: Diagram of the adsorption process step. Brown dots represent gaseous contaminants to be removed.

Step 2 – Gas displacement and desorption: Desorption is achieved by flowing hot liquid heat transfer fluid (HTF) through the inside of the channel, in direct contact with the polymer layer. Heat is transferred much more effectively from the liquid to the adsorbent than in the case of dedicated channels for feed gas and HTF due to the elimination of the conduction resistance through the monolith walls. The flow of hot water is continued until the adsorbent is sufficiently heated and desorption is complete.

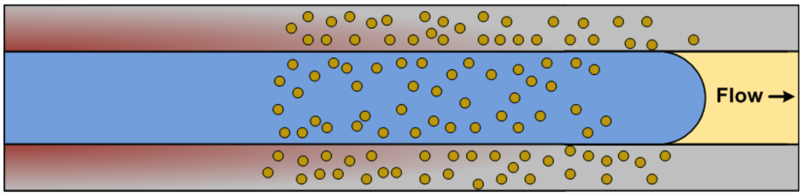

Figure 1.4: Displacement of gas with hot HTF, causing simultaneous desorption of contaminants from the adsorbent walls.

Step 3 – Cooling/Regeneration: Cold water is then passed through the channels to cool the adsorbent in preparation for the next adsorption step. Once again, because the fluid is in direct contact with the polymer, the heat transfer characteristics are favorable. Once the adsorbent is cooled to the adsorption temperature, the flow of HTF is shut off.

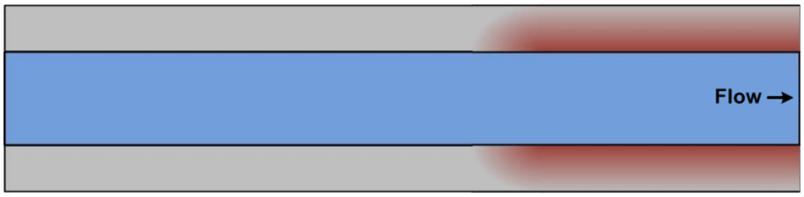

Figure 1.5: Cooling of channel walls with flow of cold HTF.

Step 4 – Liquid displacement and liquid purge: Liquid remaining in the channel is displaced by the inflow of gas. If a continuous liquid film remains on the channel walls after displacement, a purge step may be necessary to remove this film, because such liquid films would present a problematic mass transfer resistance, hindering diffusion into the walls. This purge step could be accomplished with an inert gas or with pre-purified methane gas.

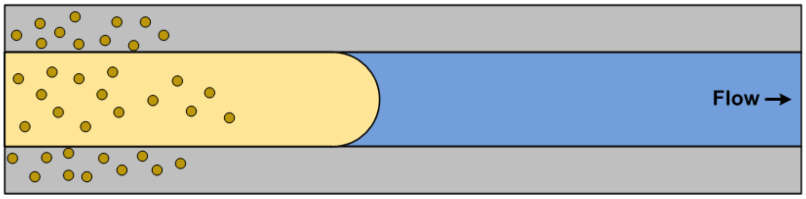

Figure 1.6: Displacement of liquid with feed gas, removal of liquid, and restarting of the adsorption

This concept reduces system size, allowing for more adsorbent capacity per system volume, simplifies fluid header designs, and eliminates conductive heat transfer resistances through the channel walls, instead placing the heat transfer fluid in direct contact with the adsorbent-laden polymer matrix. Despite these clear advantages, the presence of both liquid and gas in the same channels presents a new and unique set of challenges to be investigated.

First among these challenges is the effective modeling of the displacement of liquid by gas and the displacement of gas by liquid in the adsorbent microchannels. While in the past considerable work has been devoted to the study of two-phase flow behavior in microchannels, the body of work currently available is concerned primarily with the steady-state flows of condensing vapor simultaneously supplied, or well-mixed adiabatic gas-liquid mixtures through microchannels. In contrast, the two-phase flow present in the proposed gas separation concept is an inherently transient and sequential process, and the effectiveness of the process is strongly dependent on the ability to *prevent* mixing of the two phases at the liquid-gas interface and to quickly remove one phase with another. The ability to model bulk fluid displacement in microchannels is essential to predictions of cycle times and mass transfer performance.

The second major challenge presented by the dual-use channel design is the ability to predict, account for, and minimize the presence of residual liquid films on the channel walls. As the bulk of the liquid heat transfer fluid is displaced from the channel by gas, a thin film of liquid may remain on the channel walls after the bulk of the liquid is forced out. This liquid film has the potential to greatly decrease the effectiveness of the gas separation process by introducing additional mass transfer resistance, depending on how the residual film distributes itself across the channel cross-section. Because the primary means of transferring heat into the channel is the liquid itself, any removal or redistribution of liquid in the channel must occur hydrodynamically, a task which is typically very difficult. Realistic mass transfer modeling and the preservation of system mass transfer performance require an understanding of the behavior of liquid films on the channel walls and the determination of process parameters and improvements for the minimization or elimination of residual liquid films.

1.1 Scope of Current Research

The above discussion outlines some of the primary challenges associated with the use of dual-use adsorbent channels in adsorption-based gas separation systems. The ability to model transient liquid-gas interface movement during fluid displacement and to predict and minimize residual liquid films after displacement is needed in order to fully understand, evaluate, and design the process. The present work investigates two-phase fluid behavior during the displacement of liquid by gas and the displacement of gas by liquid in channels with 200 µm diameter using both computational and experimental methods.

An air-water two-phase flow visualization study was performed using transparent 200 µm glass microchannels. High-speed video recordings of both displacement processes were obtained and analyzed, both qualitatively for flow pattern identification, and quantitatively for interface velocity, void fraction, and liquid film thickness using image analysis software. These experiments and analyses were repeated for a wide range of driving flow conditions.

Computational models were developed for the prediction of bulk fluid movement during the displacement processes. These models were developed from fundamental physical principles and validated using data obtained from the flow visualization study. Further modeling efforts included the development of preliminary coupled heat and mass transfer models for the investigation of the impact of residual liquid films on overall mass transfer performance.

1.2 Thesis Organization

This thesis is organized as follows:

- Chapter 2 provides a review of the literature on multiphase flow in channels of several sizes, including heat transfer, void fraction, flow regime, and pressure drop studies. In addition, this section includes a brief discussion of adsorption technologies and their applications.

- Chapter 3 describes the development of the computational models for two-phase bulk fluid movement and adsorbent layer heat and mass transfer.
- Chapter 4 describes the experimental apparatus and procedures for the flow visualization study, analysis procedures used in data reduction, and the results obtained.
- Chapter 5 contains a detailed discussion of experimental and modeling results, comparisons of model predictions with data, and discussion of the impact of these results on the system under consideration in the present study.
- Chapter 6 summarizes important conclusions and provides recommendations for future work.

CHAPTER 2

LITERATURE REVIEW

The objectives of this chapter are twofold. First, this section outlines the current state of gas separation technology, with emphasis on systems and techniques for the purification of methane gas, and to thereby establish the context and significance of the gas separation system under consideration here. The relative advantages and disadvantages of existing methane gas separation systems are discussed to illustrate the novelty and the need for the proposed system. Furthermore, the present concept relies on the incorporation of technologies and methods used in existing gas separation systems, most notably the use of mixed-matrix polymer-zeolite materials developed for use in membrane diffusion systems. For this reason, an understanding of the existing (and competing) technologies is valuable both for understanding the operating principles of the system, and for the assessment of its potential significance in the gas separation industry.

The second objective of this section is to understand the existing body of work pertaining to two-phase flow regime classification and prediction in adiabatic gas-liquid flows, with particular focus on channels in the sub-millimeter range. As discussed in Chapter 1, the presence of both liquid and gas phases in the adsorbent microchannels allows for simpler system operation and smaller system footprint. However, the effectiveness of process mass transfer is expected to be extremely sensitive to the mechanics of the gas-liquid interactions in the adsorbent channels during displacement. While no studies to date have addressed the transient sequential displacement of one phase with another in microchannels, the two-phase flow phenomena observed in the microchannel literature lend valuable understanding to the present case. The survey of two-phase flow literature included in this section demonstrates the need for the present investigation of multiphase displacement flow in 200 μm channels.

This chapter is organized as follows:

- Section 2.1 contains a review of current methane separation technologies, with a focus on the relative advantages and disadvantages of each technology, especially in relation to the proposed TSA system.
- Section 2.2 contains a review of two-phase flow regime studies for several tube size ranges, illustrating the effects of channel diameter and geometry on the relative influence of viscous, gravity, and surface tension forces.
- Section 2.3 discusses deficiencies in the literature, both in gas separation systems and in the two-phase flow phenomena relevant to the system under consideration here.
- Section 2.4 outlines the research objectives of the current study based on the needs identified through the literature review.

2.1 Methane separation technology

The purification of methane (CH_4) on a commercial scale has been the subject of study for several decades. As the use of natural gas combustion becomes more widespread as a primary energy source in transportation, power generation, and space conditioning, and as environmental concerns for combustion and purification become more important, methane purification systems capable of producing higher purity and greater volume will be in great demand. Whether extracted directly from underground reservoirs, distilled from heavier hydrocarbon mixtures, or captured from coal mines and bio-reactors, raw (or "sour") natural gas stock typically contains contaminants such as N_2, CO, CO_2, and H_2S in concentrations of 10-30% (Baker, 2002; Abatzoglou and Boivin, 2009). The more benign of these impurities (such as N_2) merely decrease the energetic potential of fuel combustion without creating dangerous or destructive side effects. For this reason, and because the means of separating N_2 from natural gas mixtures is very energy intensive, nitrogen-rich methane streams are often simply mixed with methane stock of higher purity to produce an acceptable product. It is worth noting, however, that mixing is only feasible up to N_2 contents of about 10%; because of this, an estimated $30 billion worth of US natural gas reserves (10 trillion standard cubic feet) are currently untapped due to high (10-25%) nitrogen content (Baker, 2002).

The "sour" or acid gas contaminants (CO, CO_2, and H_2S), on the other hand, not only decrease the energetic potential of the fuel during combustion, but also pose serious and costly corrosion risks to pipelines and machinery, and generate harmful environmental emissions (Abatzoglou and Boivin, 2009). Additionally, because CO_2 has a relatively high freezing temperature, there is a possibility of freezing in natural gas pipelines, creating blocks of dry ice that clog pipelines and damage pumping equipment (Bernardo *et al.*, 2009). Removal of these acid gases is a high priority in commercial applications, and approximately 20% of all domestic natural gas requires extensive on-site acid gas removal before being sent to pipelines for transportation and further refinement (Baker, 2002).

The primary methods for separation of acid contaminants from natural gas belong to three categories: absorption, membrane separation, and adsorption. Several other technologies are currently in use for smaller-scale applications; these processes include cryogenic distillation (sometimes used for air-rich mixtures) or controlled freeze separation (used for mixtures with especially high acid gas concentrations) (Parkera *et al.*, 2011). However the three primary methods (absorption, adsorption, and membrane separation) dominate the current commercial landscape. The subsequent sections will describe these common commercial-scale processes for acid gas removal from methane and outline their respective advantages and disadvantages.

2.1.1 Absorption separation

The most widely utilized large-scale process for the removal of acid gases from methane involves the absorption of gaseous contaminants into liquid solvents or aqueous solutions with strong chemical affinities to acid gases (Bernardo *et al.*, 2009). The application of such processes is not limited to methane separations; absorption gas separations are also generally regarded as one of the more viable processes for carbon capture from flue gases (Yang *et al.*, 2008). The scalability and continuous nature of absorption processes make them very attractive for large industrial scale applications; however, absorption systems have high capital and operating costs and occupy large footprints, making them less desirable for small and medium applications such as offshore platforms and wellsite pre-pipeline acid removal (Aaron and Tsouris, 2011).

The most common family of absorption processes utilizes monoethanolamine (MEA) as the liquid solvent because of its strong affinity to acid gases over methane (or oxygen and nitrogen, in the case of flue gas carbon capture). Impure methane gas meets the MEA solvent in a liquid-gas contactor, where CO_2 and H_2S are absorbed into solution and removed, leaving the remaining methane-rich mixture to flow out of the contactor to be stored or transported. The CO_2 and H_2S-rich MEA solution then flows to a regeneration column or “stripper”, where heat is applied to the solution to desorb the CO_2 and H_2S. The solvent is then recycled and pumped back to the contactor to absorb more acid gas. A schematic of this process is shown in Figure 2.1.

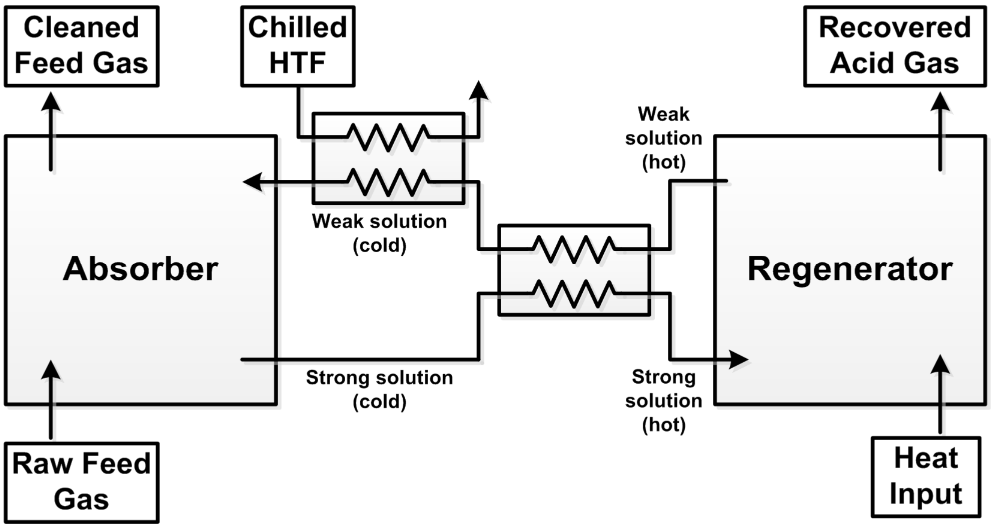

Figure 2.1: Schematic of a basic MEA absorption gas separation system.

Because absorption systems use a liquid solvent, which can be pumped in a loop, absorption processes can be operated continuously, stopping only to replace solvent, which is gradually degraded by non-regenerable reaction with strongly reactive trace impurities that may be present, such as SO_X (SO_2, SO_3, and SO_4) and NO_X (NO_2 and NO_3) (Baker, 2002; Aaron and Tsouris, 2011).

This continuous nature of the process makes absorption systems easily scalable to suit applications of all sizes, however because the baseline capital costs of MEA absorption systems are comparatively high, they are typically only applied to large-scale applications (Baker, 2002). In addition to high capital costs, the need to periodically replace solvent, the corrosive effects of the solvent on the system hardware, and the large amount of energy required for solvent regeneration (desorption) make the overhead costs for system operation similarly high (Yang *et al.*, 2008). Chakma and Tontiwachwuthikul (1999) reported that when applied for CO_2 capture applications, the cost of operation, including energy usage, equipment maintenance and labor, and solvent replacement, were in the range of \$40-\$70 per ton of CO_2. Gottlicher and Pruschek (1997) reported that energy usage for an MEA absorption process was 0.342 kWh/kg CO_2 (\$13.95 per ton in 1997). For comparison, energy costs for a pressure-swing adsorption (PSA) separation system in similar carbon capture applications are reported to be \$6-\$30 per ton of CO_2 (energy cost depends strongly on CO_2 concentration in the feedstock), and solid adsorbents are typically far more regenerable, resulting in relatively low replacement costs (Aaron and Tsouris, 2011).

There are several challenges in the efforts to make absorption processes more energy efficient and economically competitive. The first of these challenges is the trade-off between solvent selectivity and regenerability: solvents with strong affinities to acid gases have large loading capacity, but require large desorber heat inputs to overcome the strong solvent-solute attraction, whereas solvents with lower affinities are easily regenerated, but suffer from low loading capacity (Aaron and Tsouris, 2011). The choice of solvent and the conditions for adsorption and desorption must be optimized for each application based on the feed concentrations, desired purity, and other system parameters. Another avenue of exploration is the development of new solvents with greater resistance to degradation, lower corrosiveness, lower energy requirements for regeneration, and higher loading capacities. Examples of these improved solvents include proprietary solvents such as the Econamine FG, PSR, and KS families (Chapel *et al.*, 1999).

The second challenge is the problematic and expensive degradation of solvent at high temperatures and in the presence of fly ash and strongly acidic gases (SO_X, NO_X, etc), which cause the formation and precipitation of insoluble salts when in contact with solvents. In existing CO_2 capture systems, about 1.6 kg of solvent is lost per ton of CO_2 captured (Chapel *et al.*, 1999). These solvent losses are often combated by flue gas precoolers, the use of non-regenerable solid gas scrubbers, or hybrid systems (membrane or adsorption pretreatment before MEA polishing), all of which are often more cost-effective than purchasing new solvent. However, conventional scrubbers are typically incapable of removing sufficient amounts of SO_X and NO_X to eliminate the problem of degradation completely (Bhide *et al.*, 1998; Aaron and Tsouris, 2011). As mentioned previously, new solvents are also being investigated as potential solutions to the problem of degradation, but MEA remains the dominant solvent for nearly all industrial acid gas removal applications.

Despite these considerable hurdles and drawbacks, MEA absorption remains the most widely used technology in natural gas separations. This is largely due to the fact that MEA absorption systems have been in use in the chemical industry for over 60 years and the technology is extremely well established; numerous large-scale systems are in operation and the mechanisms and thermodynamics involved are well understood (Yang *et al.*, 2008). As alternate methods (most notably pressure swing adsorption and membrane processes) become more competitive, the development of new solvents and feed gas pre-treatment methods will be important to keep absorption processes economically favorable.

2.1.2 Membrane separation

Membrane separation systems have gained a solid foothold in smaller-scale methane separation applications (<40 million standard cubic feet per day) in which remote location, lack of available footprint, or energy usage are concerns. Membrane separation systems have the advantages of very low energy input, small footprint, and extremely simple machinery with few moving parts (none in some cases), making them ideal for use on offshore platforms, in purification for on-site use, and in locations where the acid gas content of the feed gas is high enough to prevent piping to larger treatment facilities (Koros and Mahajan, 2000; Bernardo *et al.*, 2009). While membrane systems have problems with scalability due to system costs and difficulties with fabrication of large modules, advancements in membrane technology continue to make membrane technology more viable on larger scales, and several medium-sized treatment facilities use membrane separation technology. Additionally, membranes are often used in conjunction with other processes as pretreatment or reclamation systems, and advances in membrane chemistry and materials science have been adopted for use in other process families, such as adsorption systems (Bhide *et al.*, 1998).

Membrane separation systems are extremely simple to operate, and require only a small driving pressure gradient across the membrane to actuate separation. This driving pressure is typically provided by a fan, compressor, or the gas wellhead itself (Bernardo *et al.*, 2009). Membranes are typically packaged into compact modules and can be fabricated in flat-plate, spirally-wound, or hollow-fiber configurations, depending on the application and the mechanical properties of the membrane material. Feed gas enters the module and is passed over the membrane surfaces, allowing one species to preferentially permeate through the pores of the membrane. The bulk gas flow bypasses the pores and continues parallel to the membrane surface until it is ultimately captured at the module outlet (Koros and Mahajan, 2000). A diagram of a typical membrane separation process is shown in Figure 2.2.

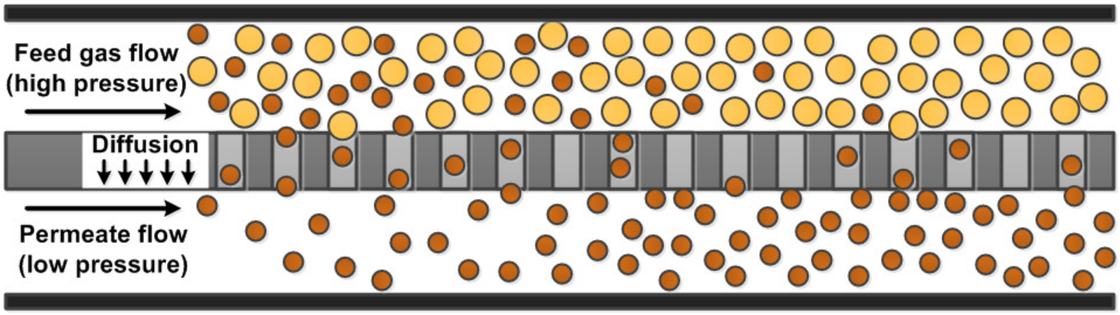

Figure 2.2: Schematic of a membrane diffusion separation process. Purity of methane (large yellow dots) on the high pressure side increases from left to right, while the contaminants (small brown dots) permeate the membrane to the low pressure side.

The selectivity and productivity of a membrane system are primarily dependent on the material properties of the membrane at the operating conditions and the thickness of the membrane. Thinner membranes allow greater flux through their thickness (higher productivity), requiring less material area for a given output flux and reducing overall system cost. Similarly, membranes with greater selectivity require lower driving pressure ratios for separation, reducing compressor loads and lowering the system operating cost

(Koros and Mahajan, 2000). Selectivity of a membrane is derived from the manipulation of several different physical mechanisms. Membranes are classified into five main families based on the particular mechanisms used to create a preference for one gas species over another.

Polymeric solution-diffusion membranes: The first of these membrane types is the polymeric solution-diffusion membrane, typically composed of glassy polymers such as cellulose acetate, polyimides, or polyamides. Of all the membrane types in use, these polymeric membranes have the most commercial applications and are dominant in industrial membrane separations of methane (Bernardo *et al.*, 2009). A membrane assembly is typically composed of a thin (0.1 μm) selective glassy polymer layer bonded to a thicker macroporous layer with low permeation resistance for mechanical support (Baker, 2002). Solution-diffusion membranes differentiate between gas species based on the penetrant size, and transport is postulated to occur based on the thermally-induced motion of polymer chain segments, which causes transient gaps to form and fade in the polymer layer. The smaller molecules (penetrant molecules) are able to diffuse through the membrane layer as these gaps are created. Polymeric membranes are generally the most economical option in membrane separation due to their flexibility and ability to be easily spun into hollow-fiber modules or spiral-wound sheet modules. However, solution-diffusion membranes do suffer from loss of stability and performance at high temperatures and pressures or in the presence of strongly sorbing components, which can clog pores and cause the membrane to swell and plasticize. In addition, the same chain flexibility that allows for the creation of transient gaps also limits the ability of the polymer to differentiate between molecules of similar sizes (Koros and Mahajan, 2000).

Molecular sieving membranes: Molecular sieves are similar to solution-diffusion membranes in that they separate species based on particle size, but are distinct in that the selectivity is derived from the existence of static, rigid micropores or nanopores rather than the transient creation of flexible pores. The pores in molecular sieving materials are sufficiently small to allow certain molecules to penetrate while excluding others, making them extremely selective, in some cases up to five or ten times more selective than their polymeric counterparts (Koros and Mahajan, 2000). In addition, the membrane materials are extremely rigid, giving them greater stability than polymeric materials at temperature and pressure extremes or in the presence of strongly adsorbing substances. This same rigidity also makes the membranes much more brittle, fragile, difficult to process, and expensive to fabricate The cost per gram of common molecular sieving materials such as carbon matrices or nanotubes can be from 10 to 100 times higher than those of polymeric materials (Koros and Mahajan, 2000; Baker, 2002). Despite their excellent selectivity and separation characteristics, molecular sieves have only been adopted in niche applications in membrane separation, largely due to high cost and fabrication difficulties (Bernardo *et al.*, 2009).

Surface selective flow membranes: Also called “reverse selective” or “solubility controlled” membranes, surface selective flow membranes are unique in that they can preferentially permeate larger molecules, as opposed to the membrane technologies mentioned previously, which only allow the smaller molecules to permeate. This is accomplished through the use of nanoporous membranes with strongly selective adsorption properties. The permeant adsorbs strongly onto the pore inner surface and moves to the low pressure (collection) side of the membrane via surface diffusion. In a manner similar to the way that strongly adsorbing species cause pore clogging in polymeric membranes, the strong adsorption of the permeant on the pore walls presents a hindrance to transport of the smaller, non-adsorbing molecular species. These transport characteristics are typically found in rubbery polymers such as PDMS and other silicon rubbers. These materials provide very high permeability and are attractive in scenarios such as the separation of CO_2 from lighter gases or methane from higher hydrocarbons (Yang *et al.*, 2008; Bernardo *et al.*, 2009).

Zeolite membranes: Zeolites are nanoporous crystalline aluminosilicates that selectively permeate gas species based on a combination of molecular sieving effects (attributable to their highly uniform rigid pore structures) and preferential strong adsorption and surface diffusion. Zeolite membranes have high selectivities and are much less susceptible to performance loss at high temperatures or in harsh chemical environments than polymeric materials. The costs of zeolite membrane modules compare favorably with those of molecular sieving materials, and zeolite membranes have achieved some use in the separation of CO_2/N_2 mixtures and light hydrocarbons (Yang *et al.*, 2008). In addition to their use in membrane processes, zeolites are now commonly employed in adsorption separation processes due to their large adsorbate loading capacities and strong preferential adsorption characteristics. These applications are discussed in greater detail in subsequent sections.

Complex sorption-diffusion membranes: Complex sorption-diffusion membranes are similar to the solution-diffusion family of membranes, but involve a chemical reaction step in addition to simple penetrant solution and diffusion. The most common type provides facilitated transport for molecular species by through the use of an aqueous carrier solution with which the penetrant reacts reversibly. In addition to simple diffusion through the pores, the penetrant can react with the carrier solution and diffuse down the liquid gradient as well, a transport mechanism that is not available to the non-reacting gas. The reaction is then reversed on the low pressure side of the membrane to capture the penetrant (Yang *et al.*, 2008; Bernardo *et al.*, 2009). These membranes can have excellent selectivity and permeability with a low driving pressure and concentration gradient; however, several problems such as membrane dryout and the loss of carrier species over time must be resolved for these membranes to be usable on large scales (Koros and Mahajan, 2000).

Mixed-matrix membranes: Mixed matrix membranes are a hybrid membrane technology developed to combine the ease of fabrication and flexibility of polymers with the selectivity and resistance to harsh environments of molecular sieves. This is accomplished by mixing microparticles or nanoparticles of inorganic molecular sieving materials (discrete phase) into a polymeric matrix (continuous phase) and spun into spirally-wound or hollow-fiber modules. One common type of mixture is that of zeolite particles or flakes added to flexible rubbery polymer materials such as PDMS. In the case of zeolite 5A and PDMS, the addition of zeolite particles significantly improved the separation properties of the PDMS membrane for CO_2/CH_4 and O_2/N_2 separations. Similar experiments were performed with glassy polymer materials such as cellulose acetate; however, due to the greater rigidity of glassy polymers, there were significant problems with particle adhesion, as high interfacial stresses between the two materials often resulted in voids through which gases could bypass the zeolite particles (Bernardo *et al.*, 2009). In addition to membrane separation applications, rubbery polymer-zeolite mixtures are also being investigated as possible candidates for adsorption separation modules.

Table 2.1 provides a list of the membrane technologies discussed above, along with a summary of the advantages and disadvantages of each.

Table 2.1: Summary of membrane types, advantages, and disadvantages.

Membrane Type	Advantages	Disadvantages
Polymeric solution-diffusion	• Inexpensive and most commonly used • Flexible and easily fabricated into large spirally-wound or hollow-fiber modules (Koros and Mahajan, 2000)	• Loss of stability and performance at high temperatures and pressures (Baker, 2002) • Pore blockage and plasticization in the presence of strongly sorbing or reactive components (Bernardo *et al.*, 2009) • Limited selectivity due to polymer chain flexibility (Koros and Mahajan, 2000)
Molecular sieving	• Rigid nanopores exclude large molecules (Koros and Mahajan, 2000) • Selectivity 5 to 10 times higher than polymeric membranes (Bernardo *et al.*, 2009) • High stability at temperature and pressure extremes • Maintain performance in reactive environments	• Can be 10 to 100 times more expensive than polymeric membranes (Baker, 2002) • Brittle and fragile; difficult to fabricate in large sheets and modules (Bernardo *et al.*, 2009)
Surface selective flow	• Separation based on adsorption characteristics rather than particle size • Can be used to separate heavy molecules from mixtures of lighter ones (Yang *et al.*, 2008) • Can be made with flexible rubbery polymers (Bernardo *et al.*, 2009)	• Only useful for niche applications
Zeolites	• Highly selective (similar to molecular sieves) • Less expensive; cost competitive with polymeric membranes (Yang *et al.*, 2008) • Strong preferential adsorption characteristics; also used in adsorption applications (Cavenati *et al.*, 2004)	• Brittle and fragile; difficult to fabricate in large sheets modules (Bernardo *et al.*, 2009)
Complex sorption-diffusion	• High selectivity and productivity with low driving pressures (Koros and Mahajan, 2000)	• Only useful in niche applications; strongly dependent of chemical differences between components • Relies on liquid carrier solution; membranes prone to dryout and carrier solution must be replaced (Yang *et al.*, 2008)

Table 2.1 (continued)

Membrane Type	**Advantages**	**Disadvantages**
Mixed-matrix	• Combines the flexibility of polymers with the selectivity and resilience of molecular sieves • Can be spun into spiral or hollow-fiber modules (Lively *et al.*, 2011) • Also used in adsorption applications (Cavenati *et al.*, 2004)	• Some difficulties with sieve-polymer pairing and adhesion; loss of adhesion causes loss of selectivity (Bernardo *et al.*, 2009)

Membrane systems, primarily cellulose acetate and other glassy polymers, continue to be competitive in many small and moderate scale operations, especially in remote locations or places where small system footprint is a requirement. In smaller applications, the simplicity and compactness of membrane systems make it the obvious choice for gas treatment and pretreatment, and in multistage systems, membranes are capable of achieving 95% methane recovery with comparatively low energy input and maintenance. Membrane systems also have a much smaller environmental impact than absorption systems, which require the use and disposal of toxic solvents. While plasticization and swelling of polymers remain serious issues, new materials with superior mechanical, chemical and thermal properties, such as polyimides and polyamides, may provide solutions to these problems (Bernardo *et al.*, 2009).

In addition, in some cases, membrane systems have also provided a cost-effective method of gas pre-treatment in large scale hybrid systems. Since 1994, a plant in Mallet, TX has used a hybrid system utilizing membrane separations for bulk removal of CO_2, H_2S, and heavy hydrocarbons and a methyl-diethanolamine (MDEA) absorption system for polishing. Together, these systems are capable of purifying feeds with compositions of up to 90% CO_2 and heavy hydrocarbons. While a hybrid process such as this one has greater complexity and capital cost than a standalone MDEA absorption system, it was reported that the hybrid system reduced operating costs by 30% compared to the standalone MDEA system (Bhide *et al.*, 1998).

For membrane separation technology to become competitive on larger scales, membranes with greater selectivities and resistance to high temperatures and pressures and harsh chemical environments must be developed. The cellulose acetate membranes currently in use have selectivities of 12 to 15; it was predicted by Baker (2002) that the development of a usable membrane with a selectivity of 40 could drastically change the competitiveness of membrane processes, making them viable candidates for large-scale separations. It was estimated that an increase in selectivity from 15 to 40 could reduce membrane area by 40%, compressor load by 35%, and methane loss by 75%. Membranes with selectivities of approximately 40 have been demonstrated in laboratories, but significant improvement is needed to maintain their material properties in real-world industrial processes. The use of mixed-matrix materials shows some promise in this area; these materials have shown improved ability to maintain selectivity in harsh conditions (Koros and Mahajan, 2000).

A parallel area of development with great potential for improving membrane processes is the fabrication of larger membrane modules. For a plant that uses large compressors (instead of wellhead pressure), membrane modules constitute only about 10-25% of the total plant cost, with the other 75-90% being the compressors, valves, instrumentation, etc; large membrane plants can have up to 400 pressure vessels and 2000 modules, each requiring valves and sensors. Larger membrane modules have the potential to reduce the complexity, footprint, and valve and instrumentation requirements for new plants (Baker, 2002).

2.1.3 Adsorption separation

The final method of methane purification currently in use is adsorption gas separation. Adsorption processes take advantage of the fact that gas molecules can be selectively attracted and trapped by exposed chemical groups or microscopic cracks, pores, and defects on the surface of a solid. This attraction causes the molecules to condense on the material surface and reside in a liquid phase at saturation pressures lower than that of the pure liquid. Several material-dependent surface effects and mass transfer phenomena can be manipulated to enhance the selectivity and loading capacity of an adsorbent material. The overall adsorption process uses a combination of several mass transfer phenomena described previously, namely molecular sieving and surface diffusion effects, as well as physisorption and capillary condensation phenomena (Kapoor and Yang, 1989).

Physisorption, also called physical adsorption, is the attraction and adsorption of molecules onto a material surface via van der Waals forces. This is distinct from other adsorption mechanisms in that the electronic structures of the molecule and surface group are only slightly perturbed by adsorption, as opposed to chemisorption (also called reactive adsorption), in which surface and gas molecules form covalent or ionic bonds with one another. This is significant from a process standpoint because the weak molecular interactions inherent to physisorption allow for the manipulation of adsorption and desorption with far smaller energy inputs than in a chemisorption process. Gas molecules can also physisorb onto other adsorbed molecules via the same van der Waals forces, causing multilayer adsorption. In small capillary pores, cracks, and defects, this can lead to the filling of the capillary and formation of a meniscus separating the liquid and gas phases. This is called capillary condensation.

Like absorption separation processes, the sorption and desorption of gas species are effected by manipulating the thermodynamic state at different points in the process. Adsorption processes are characterized as pressure-swing adsorption (PSA) or temperature-swing adsorption (TSA) processes. In both processes, adsorption is achieved by placing the feed gas in contact with adsorbent particles at high pressures, causing the gas mixture components to separate based on differences in condensability, polarity, molecule size, and surface interaction (Yang *et al.*, 2008). PSA and TSA processes differ in the method used for desorption of adsorbed mixture components. In PSA processes, the system pressure is reduced, in some cases to near-vacuum pressures, causing the regeneration of the sorbent as the adsorbed molecules re-enter a gaseous state. TSA processes achieve desorption and regeneration by raising the system temperature, causing a corresponding decrease in vapor pressure of the adsorbed components.

Unlike absorption or membrane separation processes, which can be operated continuously (aside from pauses for the replacement of fouled membranes or degraded solvent), the reliance of adsorption processes on solid sorbents requires them to be operated in repeated, discrete cycles requiring precise control. Adsorbents are typically held in large packed beds (e.g., pressure vessels filled with adsorbent pellets), or in some implementations currently in development, monoliths of adsorbent-coated microchannels. Quasi-continuous process output can be achieved by operating several beds in parallel, out of phase with one another, so that the feed and effluent flows remain fairly constant (Cen *et al.*, 1985).

A cycle for an individual adsorbent bed typically consists of the steps listed below. For the purpose of this explanation, it is assumed that the contaminants are strongly adsorbed. However it should be noted that processes do exist in which methane is the less inert gas (this is true for $CH_4/N_2/O_2$ separations, for example). In these cases, the methane species is adsorbed and the contaminants remain in the gaseous state (Cen *et al.*, 1985; Olajossy *et al.*, 2003). A diagram of a basic adsorption process is shown in Figure 2.3.

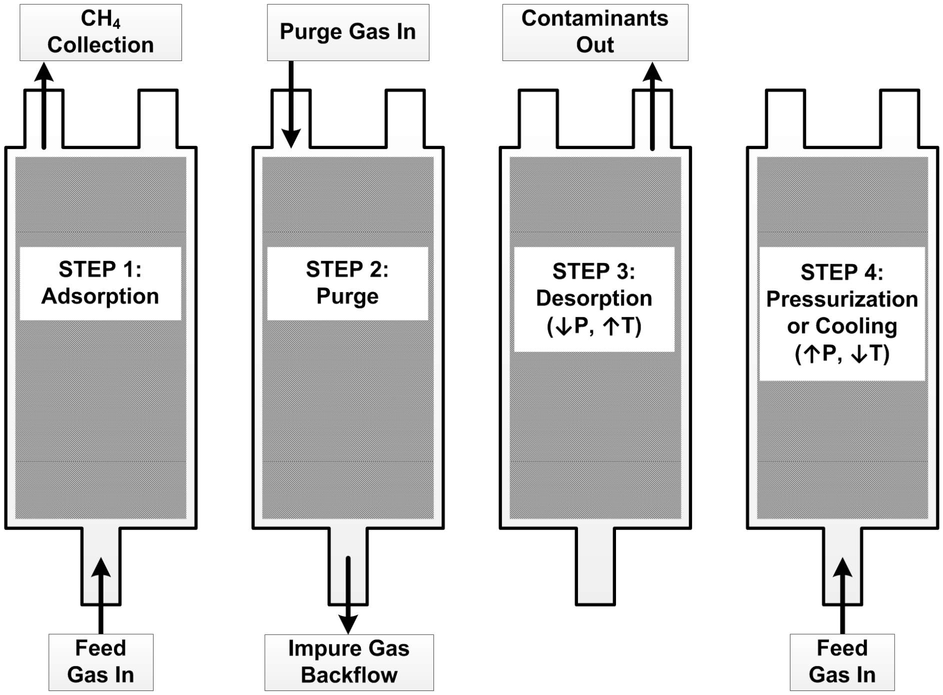

Figure 2.3: Diagram of and adsorbent bed during a basic adsorption gas separation process.

Step 1 – Adsorption: Feed gas enters the adsorbent bed at the high pressure (feed pressure), causing contaminants to adsorb onto particle surfaces. Gas is typically pumped slowly from the feed side of the adsorbent bed to the collection side (this is called the co-current direction), creating a wave of adsorbed concentration that moves in the co-current direction until it reaches the end of the bed. The effluent gas purity at the collection side is high (typically greater than 95%) while the adsorbed concentration wave moves along the bed length, but drops rapidly as the wave reaches the end of the bed. The adsorption step is stopped at this point. Decreasing the raw gas feed rate improves the outlet gas purity and the sharpness of the adsorbed concentration wave, but the increased cycle time decreases the overall productivity of the cycle (Cen *et al.*, 1985). Feed rates are optimized based on the system parameters and product purity requirements.

Step 2 – Countercurrent purge: To aid in methane recovery, the remaining methane feed mixture residing in the void spaces of the adsorbent bed is displaced back into the feed line using either an inert gas or the methane-rich effluent from previous cycles. This process is stopped when the bed voids are effectively filled with contaminant gases (Olajossy *et al.*, 2003).

Step 3 – Desorption: In PSA processes, the desorption phase is effected by rapidly depressurizing the bed, in some cases to near-vacuum pressures, though most processes utilize a fairly small pressure swing to reduce pumping requirements (Olajossy *et al.*, 2003). This decrease in pressure regenerates the adsorbent loading capacity and preparing it for the next adsorption cycle. In TSA processes, this step is achieved by heating the adsorbent bed to reduce the vapor pressure of the adsorbed phase. The major fraction of the contaminant is desorbed and the effluent is removed. However, because the bed remains at the high pressure, significant amounts of contaminant gas still remain in the voids (Riemer *et al.*, 1994). These gaseous contaminants will re-adsorb when the adsorbent is cooled, causing an effective decrease in adsorbent loading capacity. For this reason, TSA processes may incorporate another purge phase at this point to displace the gaseous contaminants.

Step 4 – Pressurization (PSA) or Cooling (TSA): The pressurization step (for pressure-swing processes) and the cooling step (for temperature-swing processes) bring the system back to the initial thermodynamic state, which allows adsorption to occur again. In a PSA cycle, repressurization is often accomplished by filling the vessel with the feed gas, a simple process. In TSA cycles, the process of cooling the adsorbent to the adsorption step temperature often proves to be more complicated; in fact, the use of TSA for industrial gas separations has not been considered feasible. This is due to the difficulties associated with heating and cooling adsorbent materials, which typically have extremely low effective thermal conductivity due to their low material conductivities, high porosity, and, as in packed beds, the existence of significant void spaces (Riemer *et al.*, 1994).

While the transfer of heat through adsorbent beds has proven problematic, the appeal of TSA cycles in gas separation lies mainly in the fact that no large pressure swings are necessary, which, in theory, allows for simpler valve and compressor operation and reduced compressor loads. Efforts to make TSA processes viable for general application (including gas separation) have included the incorporation of finned-tube or microchannel heat exchangers into adsorbent beds to provide more rapid heating and cooling, or the regenerative heating and cooling of adsorbent using process gas from parallel cycles operating out of phase (Miles *et al.*, 1993; Pons, 1997).

Another method investigated as a potential solution to the challenges associated with TSA processes is the use of microchannels for the enhancement of heat transfer in gas separation and carbon capture systems. Systems with monolithic arrays of adsorbent-coated microchannels or adsorbent-laden hollow fibers aimed to achieve temperature swings more quickly and effectively than packed adsorbent bed systems by capitalizing on the excellent heat and mass transfer characteristics of microchannel flows (Determan *et al.*, 2012).

The hollow fiber systems operate by passing feed gas over the outer surface of the adsorbent fiber while running hot or cold liquid heat transfer fluid (HTF), typically water, through the center of the fiber. Similarly, adsorbent-coated microchannel arrays would be constructed with adsorbent-coated microchannels adjacent to channels for liquid heat transfer fluid. In both cases, temperature swings for desorption and regeneration could then be achieved more quickly than in packed bed systems by alternating the flow of hot and cold water through the heat transfer fluid channels.

While these solutions provide desirable heat transfer characteristics compared to packed bed systems, they face challenges in fabrication and material design. Successful fabrication of molecular sieve loaded mixed-matrix hollow fibers has been achieved on several occasions, but waterproofing them has proven difficult, and when the polymer becomes waterlogged, diffusion mass transfer through the walls is severely hindered (Lively *et al.*, 2011; Lively *et al.*, 2012). The microchannel monolith designs suffer primarily from fabrication difficulties associated with adsorbent and polymer adhesion to the monolith walls as well as plumbing such sets of alternating small channels to carry different phases.

Despite the difficulties associated with heating and cooling adsorbent materials, TSA cycles can be used in small-scale cooling and space conditioning applications, where a low-cost source of driving heat is available (such as gas-fired, solar, or waste heat driven systems), system sizes and process timescales can be sufficiently long to heat and cool the beds (as long as 24 hours in the case of a solar-actuated system). TSA cycles are even discussed as potential options for carbon capture from post-combustion flue gas, a scenario in which waste heat for desorption is abundant (Chapel *et al.*, 1999; Aaron and Tsouris, 2011; Determan *et al.*, 2012; Lively *et al.*, 2012).

Despite the aforementioned advances in TSA process design, PSA gas separation processes are regarded as superior to those using TSA. Riemer *et al.* (1994) reported that in carbon capture applications, the cost per ton of CO_2 captured was, on average, 66% higher in TSA systems than in PSA systems, and that this was due to the large energy penalty and poor speed of regeneration involved with TSA processes. PSA methane separation processes are a very well established technology and have been used for several decades; large-scale PSA separation operations have existed since the mid-1980s (Ritter and Yang, 1991). Operating costs of PSA systems compare favorably with absorption processes; a study of flue gas carbon capture using PSA reported that total operating costs equated to \$28 per ton of CO_2 captured, compared to \$40-70 per ton of CO_2 using MEA absorption (Aaron and Tsouris, 2011). The bulk of the operating cost savings are due to the fact that adsorbent materials are highly reusable and do not degrade as quickly as liquid solvents. In addition, the energy requirements for PSA process operation are relatively low; Gottlicher and Pruschek (Gottlicher and Pruschek, 1997) reported energy consumption of 0.17 kWh kg^{-1} in PSA processes, whereas Aaron and Tsouris (2011) report an energy consumption of 0.34 kWh kg^{-1} for MEA processes.

The large-scale use of PSA for gas separation does, however, have several drawbacks; because of the non-continuous nature of the adsorption process, precise and complex controls are necessary. Not only does this require numerous valves and a great deal of instrumentation, but process design is very strongly dependent on modeling for the determination of valve timing. Most adsorption processes are at least partly kinetic in nature, meaning that the selectivity of the adsorbent material is a result of the difference in diffusion rates for each molecule species through the adsorbent pores. Feed gas residence time in the adsorbent bed must be optimized to maintain both the methane recovery rate and the cycle productivity. While models are able to predict cycle output and purity effectively, usually to within about 3%, operation of adsorption facilities remains complex (Kapoor and Yang, 1989; Cavenati *et al.*, 2004). In addition, like absorption processes, it is often necessary to put feed gas through some pretreatment, such as dehydration and removal of heavy hydrocarbons.

While absorption remains dominant due to its scalability and ease of operation, the low operating cost and energy requirements of PSA processes allow adsorption to remain viable as a method for medium-to-large scale methane purification. Because most modern systems make use of molecular sieve adsorbents or polymer-zeolite mixed-matrix materials for their high selectivity, the improvement of adsorption processes is closely tied to the development of membrane technology. As materials become more selective, higher productivity and product purity will be possible.

Table 2.2 shows a summary and comparison of the three main separation processes discussed here. While adsorption and membrane separation processes show promise for significant technological improvement, neither seems immediately poised to replace absorption systems in high-volume methane treatment applications. However, as the use of natural gas for primary energy generation, space conditioning, and transportation becomes more ubiquitous, applications of small- and medium-scale systems for wellsite pretreatment and treatment of harsh and previously unusable feed stock will become increasingly important. These scenarios may show the most promise for the future of membrane and adsorption separations systems. Still, as membrane chemistry and fabrication technology advance, these systems will probably become more economically competitive on large scales, especially as energy costs become an increasingly important factor in system design.

Table 2.2: Summary of advantages and disadvantages for each of the major methane separation methods.

Process	Advantages	Disadvantages	Areas of Future Development
Membrane separation	• Small footprint (Bernardo *et al.*, 2009) • Low energy input; only small driving pressure gradient required • Well-suited to remote and pre-pipeline treatment locations (Koros and Mahajan *et al.*, 2000) • Can be inexpensive to fabricate (Baker, 2002) • Can have extremely high selectivity • Mixed-matrix membranes overcome many drawbacks of inorganic membranes (Bernardo *et al.*, 2009) • Useful as pretreatment step in hybrid separation systems (Aaron and Tsouris, 2011)	• Membrane performance degrades at high pressures and temperatures and in the presence of highly reactive components; gas may require pretreatment (Koros and Mahajan *et al.*, 2000) • Highly selective membranes typically have poor mechanical properties and are difficult to fabricate (Bernardo *et al.*, 2009) • Poor scalability due to difficulties in fabricating large membrane modules (Baker, 2002)	• Fabrication of larger membrane modules to reduce system capital costs (Baker, 2002) • Improved resilience at undesirable temperature, pressure, and chemical conditions • Fabrication of defect-free mixed matrix membranes and hollow-fiber skins (Lively *et al.*, 2012) • Higher membrane selectivity • High volume (low cost) production of highly selective membranes

Table 2.2 (continued)

Process	**Advantages**	**Disadvantages**	**Areas of Future Development**
Absorption separation	• Most widely used and well-understood separation process (Yang *et al.*, 2009) • Scalable for use in large-scale industrial chemical and carbon capture applications (Baker, 2002) • Fully continuous operation • New generation of solvents provide reductions in energy requirements, degradation, and corrosion (Chapel *et al.*, 1999)	• High capital and operating cost; desorption and cooling of adsorbent are energy intensive (Yang *et al.*, 2008; Chakma and Tontiwachwuthikul, 1999) • Solvent degradation occurs quickly and replacing solvent is expensive • Solvents are typically very corrosive • Large system footprint • Trade-off between solvent-solute attraction (selectivity) and regenerability (energy requirements) (Aaron and Tsouris, 2011)	• New solvents with greater regenerability, lower cost, and reduced corrosiveness (Chapel *et al.*, 1999) • Combination with pretreatment systems to minimize solvent loss • Efficient heat and mass exchanger design
Adsorption separation	• Inexpensive operation; PSA is less energy intensive than absorption, and solvent replacement is less expensive (Aaron and Tsouris, 2011) • Can be scaled up for large operations (Ritter and Yang, 1991) • Quasi-continuous operation can be achieved by placing parallel systems out of phase (Miles *et al.*, 1993; Pons, 1997) • Benefits from parallel advances in membrane technology	• Batchwise (non-continuous) transient process; requires in-depth modeling and precise valve and compressor operation (Kapoor and Yang, 1989; Cavenati *et al.*, 2004) • Often requires pretreatment for removal of strongly-sorbing components (e.g., heavy hydrocarbons, water) (Cavenati *et al.*, 2004) • TSA processes suffer from difficulties heating and cooling porous adsorbent masses, and fabrication of hollow-fiber mass exchangers is challenging (Riemer *et al.*, 1994)	• Improved sorbents with higher selectivity and more favorable kinetic adsorption behavior • Incorporation of microchannel heat and mass exchanger designs to improve TSA and temperature-boosted PSA processes • Microchannel heat and mass exchanger fabrication (e.g., hollow fiber monoliths, sorbent-coated metal monoliths)

2.2 Two-phase flow regimes

The study of two-phase flow regimes through flow visualization experiments has been central to the accurate modeling of heat transfer and pressure drop in adiabatic, boiling, and condensing systems. The spatial distribution of liquid and gas or vapor phases within tubes, channels, or rod bundles has a significant impact on the exchange of heat and momentum within the channel. The first step in the development of heat transfer and pressure drop correlations in multiphase systems is the identification of flow regimes and the conditions at which these regimes occur. Not only are these flow regimes dependent on the properties and flow rates of each phase, they are also strongly affected by the relative magnitudes of shear, surface tension, and gravity forces.

The balance between these forces changes greatly with channel size, and as a result, the transition between regimes, or even the existence of these regimes, in sub-millimeter channels is drastically different from those in larger diameter tubes. However, while the specifics of flow regimes in large tubes may have little value in making precise predictions of fluid behavior in small channels, valuable insight can still be gained by understanding the phenomena at work in various tube sizes, and how those phenomena are affected by reductions in tube dimensions. This section discusses the literature on multiphase flow visualization, with the specific focus of understanding the effect of channel size on flow regime. From this understanding, it is possible to develop reasonable inferences for gas-liquid interaction during displacement in 200 μm channels.

2.2.1 Conventional tubes ($D_h \geq 25$ mm)

Flow regimes in relatively large diameter tubes (D_h ~ 25 mm) have been studied for air-water and air-oil fluid pairs in both horizontal and vertical tubes. Experimental studies for vertical flow in 25 mm channels noted five major flow regimes: bubbly flow, slug flow, churn flow, annular-dispersed flow, and dispersed bubbly flow. These flow regimes are governed by the interaction of shear and gravity forces, with surface tension forces having relatively little influence in such large channels. The flow regimes for flow in vertical tubes are described below, along with the key mechanisms at work in within each regime (Ghiaasiaan, 2008).

Bubbly flow consists of deformed spherical bubbles moving through a continuous liquid phase and is observed at low gas flow rates and low-to-moderate liquid flow rates. The bubble diameters are smaller than the channel hydraulic diameter, and the bubbles have little interaction with each other. As the gas flow rate in the channel increases, the bubbles become more numerous, and the tendency for these bubbles to collide and coalesce with one another increases. As these bubbles coalesce to form larger bubbles, transition to the slug flow regime occurs.

Slug flow is observed at moderate gas flow rates and low to moderate liquid flow rates, and consists of significantly larger bubbles called Taylor bubbles, which have diameters approximately equal to the hydraulic diameter of the channel. These bubbles are formed by the coalescence of smaller bubbles, and it is possible for these smaller bubbles to exist in the liquid regions (called slugs) between the Taylor bubbles. The Taylor bubbles are separated from the channel walls by a continuous liquid film. Similarly to bubbly flow, as the gas flow rate increases, these Taylor bubbles have an increased tendency to coalesce, forming longer Taylor bubbles. As the gas flow rate increases still further the liquid slugs separating these long gas regions become unstable, causing the transition to annular flow.

Another regime occurring in vertical co-current upward flow is what is called churn flow. Churn flow is considered to be the entrance condition for slug flow, and is characterized by the chaotic motion of irregular gas pockets. The liquid-gas interface in this regime has no discernible shape, but both phases are, for the most part, continuous. This flow regime is similar to the annular flow regime in that a central core of gas is surrounded by liquid on the walls, but differs in that large surface waves form and periodically flow backwards due to gravity. This produces the “churning” motion for which the flow regime is named. Churn flow is not observed in countercurrent vertical flows or co-current downward flows, however these flow configurations are less relevant to the present study and are not discussed here (Taitel and Barnea, 1982).

Annular flow occurs at high gas flow rates regardless of liquid flow rate. This flow regime consists of a continuous core of gas flowing through the channel center, surrounded by a thin layer of liquid on the channel walls. The flow regime is also called annular-dispersed flow for tubes in this size range, because dispersed liquid droplets are often observed in the gas core in the center. These liquid droplets constantly impinge upon and depart from the liquid film surface. Velocity slip in this regime is very high due to the fact that the gas phase is continuous and has no direct contact with the walls.

Finally, dispersed bubbly flow (also called “finely dispersed bubbly flow”) is observed at high liquid velocities and low to moderate gas velocities, as this flow regime requires the total void fraction in the channel to be sufficiently low to allow a continuous liquid phase (Taitel *et al.*, 1980; Ghiaasiaan, 2008). Under these conditions the liquid phase is completely turbulent, and the turbulent forces in the channel drive apart any Taylor bubbles or deformed spherical bubbles. The resulting gas bubbles are very small, on the same size scale as turbulent eddies in the liquid phase. Because these dispersed bubbles are so small, they are also extremely rigid, making them resistant to deformation and coalescence. This resistance to coalescence prevents the formation of Taylor bubbles or larger deformed spherical bubbles. Dispersed bubbles are carried along in the liquid flow with very little velocity slip, and the gas slip velocity is typically very small relative to the large liquid velocity.

Because of the influence of gravity forces, horizontal tubes lead to flow regimes different from those described above, as well as two flow regimes not observed in vertical tubes. In horizontal tubes, the bubbly, annular dispersed, and slug flow still appear and are similar to their vertical flow equivalents, but because of gravity, the gas phase tends toward the top of the channel. In the annular regime, the gas core rises slightly towards the top of the channel, causing the liquid film on the bottom of the channel to be thicker than the film on the top. Similarly, in bubbly flow, the deformed spherical bubbles tend towards the top of the channel, but the liquid phase remains continuously in contact with the upper wall of the channel.

The two flow regimes unique to horizontal channels are the stratified smooth and stratified wavy regimes. These regimes are characterized by the separation of the liquid and gas phases into the bottom and top of the channel, respectively. These regimes are only possible for low liquid flow rates; the liquid flow rate must be small enough that the liquid phase height in the channel with no gas flow would fill less than half the channel diameter (Taitel and Dukler, 1976). The stratified smooth regime occurs under low gas flow conditions, where the interfacial shear between the gas and liquid phases is insufficient to disturb the liquid surface. Stratified wavy flow occurs as gas flow rate increases. The increased shear between the two phases causes the creation and amplification of surface ripples.

The mechanisms for transition into the slug flow regime in horizontal channels are affected by liquid flow rate. At low liquid flow rates, slug flow occurs as the surface waves in the stratified wavy regime increase in amplitude. These surface waves eventually reach the top wall of the channel, forming periodic gas bubbles that have dry contact with the top wall. At higher liquid flow rates, the mechanism for transition to the slug flow regime occurs in a manner similar to that in vertical tubes. Deformed spherical bubbles coalesce to form larger gas slugs, and a liquid film is maintained between the gas bubbles and the wall.

Several authors have developed flow regime transition criteria, either empirically from experimental data and flow regime maps, or from basic physical considerations and assumptions about the flow phenomena. These physical considerations are generally more useful in understanding the phenomena responsible for flow regime transitions.

Some well-known examples of these mechanistic flow regime transition criteria are those from Taitel *et al.* (1980), who proposed criteria for upward vertical flow, and those from Taitel and Dukler (1976), who proposed similar criteria for horizontal flow. These criteria reliably predict flow regime transitions in relatively large diameter vertical and horizontal tubes based on physical and geometric assumptions. These criteria also led to the derivation of five key dimensionless parameters, denoted by the variables *T, Y, F, K,* and *X* (also called the Martinelli parameter). Several of these parameters are defined in subsequent sections. Combinations of these parameters are compared against one another or against empirical constants to predict flow regime transitions. These dimensionless groups, both in their original forms and in modified forms, have achieved widespread use.

In Taitel *et al.* (1980), the transition from bubbly to slug flow is predicted by assuming that the transition occurs when the deformed spherical bubbles are too numerous to avoid coalescence into Taylor bubbles. The quantitative assumption made here is taken from two-phase flow visualization experiments by Griffith and Wallis (1961), who showed that the transition from bubbly to slug flow typically occurs at a void fraction of 0.25 (Mishima and Ishii (1984) made a similar assumption of $\alpha = 0.30$). This assumption was used along with the fact that the difference between the phasic velocities of gas and liquid in bubbly and slug flow is equal to the bubble rise velocity in stagnant liquid. These assumptions were used to formulate a transition criterion based on fluid properties and the superficial velocities of gas and liquid. The same work proposed a second criterion for the existence of bubbly flow in vertical tubes. It was experimentally observed that in small tubes, bubbly flow does not occur beyond the hydrodynamic entrance region, and instead becomes the entrance condition for slug flow. The criterion states that, given the hydraulic diameter of the channel, if the rise velocity of a Taylor bubble is slower than that of a regular bubble, bubbly flow cannot be maintained.

The transition for bubbly or slug flow to dispersed bubble flow was thought to happen under two key conditions: (1) that the flow must be fully turbulent and (2) that the void fraction must be less than 0.52 (Taitel *et al.*, 1980). These criteria are derived from several key assumptions. The first assumption is that the turbulence in the liquid phase breaks up large bubbles into smaller bubbles in the size range of turbulent eddies. The second assumption is that because these bubbles are so small, they are also rigid and resistant to coalescence. The final assumption, which leads to the maximum void fraction value, is based on the maximum packing volume for spherical bubbles in a simple cubic configuration. When the void fraction exceeds this maximum packing volume, it is no longer possible to sustain a continuous liquid phase and the bubbles are forced to coalesce, causing the transition into the annular regime.

As discussed previously, in the upward vertical flow configuration, churn flow is considered to be the hydrodynamic entrance condition for slug flow. For this reason, the transition from churn flow to slug flow is determined from a modified hydrodynamic entry length based on the equilibrium slug length. Finally, the criterion for transition from slug, churn, or dispersed bubble flow to annular dispersed flow is based on the fact that the drag force on a liquid droplet in the gas core must be strong enough to overcome the weight of a droplet and carry it downstream. This criterion is developed based on the droplet diameter as determined by the critical Weber number for the liquid phase.

Taitel and Dukler (1976) proposed transition criteria for the horizontal tubes as well, most of which are similar to those discussed above. The transition for stratified-smooth flow to stratified-wavy flow is based on wave generation at the liquid-gas interface. The criterion for transition from stratified flow to either bubbly, intermittent, or annular flow is based on the Kelvin-Helmholtz instability, which predicts the growth of infinitesimally small surface disturbances as a result of drag forces and reduction in cross-sectional area for gas flow.

These mechanistic criteria lend useful physical insight to the flow regime transitions, and were found to have good agreement with the data from Mandhane *et al.* (1974). Several other reliable transition criteria are based on adjustments of the criteria discussed here, empirical correlations based on flow visualization data, or simply curve fits designed for greater convenience in evaluation of the criteria, as in the work by Wong *et al.* (1990). These criteria are often created to compensate for the effect of fluid properties and tube diameter on regime transitions, or simply to create more accurate criteria for specific fluid pairs (Weisman *et al.*, 1979).

It is worth noting that many studies further divide the flow regimes discussed here into numerous sub-regimes or flow patterns. These flow patterns can be qualitatively, and sometimes quantitatively, distinguished from the main flow regimes. While this can lead to difficulties in comparing data from different studies (many studies use different terminology to refer to similar flow regimes), in some cases these minor distinctions can yield more accurate correlations for heat transfer and pressure drop. These minor distinctions are not discussed here, as they are generally not relevant to flows in small tubes.

2.2.2 Two-phase flow in minichannels (1 mm < D_h < 10 mm)

Generally speaking, the flow regimes and transition mechanisms described in the previous section hold true for tube diameters down to about 10 mm, and while the transition regions may change, all of the flow regimes discussed in the previous section are still observed in minichannels (Fukano and Kariyasaki, 1993). The reduction of tube diameter below around 10 mm marks a significant departure from the flow behaviors observed in larger diameter tubes, namely the increased influence of surface tension and viscous forces and the decreased influence of gravity.

This increased influence of surface tension was evident in the work of Barnea *et al.* (1983), who studied air-water flow in horizontal tubes with diameters of 4 to 12 mm.

In this tube diameter range, the transitions proposed by Taitel and Dukler (1976) accurately predicted all flow regime transitions, with the exception of those pertaining to the stratified flow regimes. At these small scales, a simple modification to the criterion for transition from stratified to intermittent flow was sufficient to compensate for the effect of reduced diameter. This modified criterion included surface tension in the calculation of gas phase height. In addition to this modification, this work proposed an alternate mechanism for the transition from stratified to slug flow. While in larger channels, the occurrence of slugs was attributed to the growth of surface waves due to Kelvin-Helmholtz instabilities, Barnea *et al.* (1983) observed that gas slugs were formed as capillary forces and surface adhesion caused wetting liquid to climb the walls of the channel, eventually forming liquid bridges that divide the gas region.

With a further reduction in channel diameter, even more significant deviations from the large diameter tube results were observed. Damianides and Westwater (1988) noted that in the 1 to 5 mm range, only the 5 mm tube produced results in agreement with the predictions of Taitel and Dukler (1976), and agreement was very poor with data obtained for 1 mm diameter tubes. The reduction of tube diameter coincided with increased prevalence of intermittent and annular flow regimes, with a corresponding decreased prevalence of stratified flow. They also observed that the Kelvin-Helmoltz instability mechanism did not accurately predict the stratified-intermittent flow transition, thus confirming the observations of Barnea *et al.* (1983). Yet another departure from conventional tube flow behavior was that the transition to dispersed flow occurred at higher liquid flow rates in smaller tubes, indicative of the laminarizing effect of these small channels.

The results from Coleman and Garimella (1999) further reinforced these observations in their study of horizontal air-water flow in tubes ranging from 1.3 to 5.5 mm in diameter. Their observations show a complete absence of stratified flow for tube sizes of 1.3 and 1.75 mm. Similar to the findings of Damianides and Westwater (1988), their study also noted increased liquid velocity for transition to dispersed flow with decreased tube size. The decreased tendency for stratification and gas bubble dispersion corresponds with the increased prevalence of slug and annular regimes in small tubes.

Mishima and Hibiki (1996) studied upward vertical flow in 1 to 5 mm diameter channels and noted that in smaller channels, slug bubbles become more rigid and less deformable, with leading interfaces that display strongly spherical shapes. These bubbles also occupy almost the entire channel cross section, and flow regimes in these channels were more axisymmetric than in larger channels. These axisymmetric tendencies were also noted in the work of Fukano and Kariyasaki (1993), who observed that gas slugs and cores tend towards the channel center and that liquid films become increasingly uniform in thickness as channel size decreases, even in horizontal flow. These observations are indicative of the increased influence of surface tension over gravity forces. In addition, due to the increased rigidity of bubbles with smaller diameters, it was common to see slugs and smaller bubbles separated by thin liquid films. These bubbles were found to resist coalescence more strongly than those in larger tubes.

Several studies also noted the effect of channel shape on flow regimes in this tube size range. Coleman and Garimella (1999) observed that in square channels, the transition to dispersed flow occurred at even higher liquid flow rates than in circular channels of equivalent diameter. This is probably due to the influence of capillary forces at the channel corners, which tend to draw up and retain liquid. This tendency to retain liquid in the channel corners also created a slight reduction in the gas flow rate required for annular flow transition. Zhao and Bi (2001) noted similar results in channels with equilateral triangular cross sections. The corners in the triangular channels created even greater resistance to dispersed flow than those in square channels due to their smaller acute angles.

All of the studies discussed here highlight the decreased significance of gravity and the increased influence of capillary forces as tube size decreases. However, it is important to note that the tube size ranges over which these trends occur is not uniform, and depend very strongly on the fluid pair used in the experiments. In the case of adiabatic flows (typically air-water), the relative significance of gravity can decrease to the point of being negligible for tube diameters of about 1 mm. On the other hand, experiments conducted with condensing liquid-vapor mixtures exhibit significantly different behavior due to the much smaller difference between liquid and vapor properties. For an air-water mixture, the ratio of liquid density to gas density is approximately 850 at standard conditions, but the liquid-vapor density ratios for common refrigerants at test conditions can be orders of magnitude lower (only 26 for saturated R-134a at 35 °C). For this reason, it should be noted that the studies discussed here, having been concerned mainly with adiabatic air-water mixtures, are not directly applicable to condensing fluids.

Tabatabai and Faghri (2001) proposed a flow regime map to compensate for these property differences, based not solely on superficial velocities of the individual phases, but rather on the relative magnitudes of shear, surface tension, and gravity forces on the fluids. Transition lines, and the axes for the flow regime map, were based on the ratio of pressure gradients due to surface tension and shear and the ratio of gas flow rate to liquid flow rate. The criteria were compared against the experimental results from several flow regime studies for tubes with diameters between 1 and 50.8 mm, and for both air-water and condensing refrigerant flows. Their flow regime map produced good agreement for all fluids in the map regions dominated by surface tension forces, with decreased accuracy in the regions dominated by gravity and shear forces. In addition, the criteria accounted well for the movement of transition lines with channel diameter.

2.2.3 Two-phase flow in microchannels (D_h < 1 mm)

There are several definitions for the term “microchannel”. These definitions may differ depending on the source and application, but the basic need for such a distinction stems from the inability of standard heat transfer, flow regime, and pressure drop correlations to accurately predict the behavior of channels beyond a certain size. In boiling applications, the microchannel definition may refer to the range in which the channel diameter is close to the diameter of a departing bubble (Thome *et al.*, 2004). Other useful microchannel definitions may describe the size range in which the effects of gravity and flow stratification no longer affect flow behavior (Fukano and Kariyasaki, 1993). As discussed in the previous section, such a definition clearly depends not only on the channel diameter but also on the properties of the fluid pair. Triplett *et al.* (1999) proposed the Laplace length scale, shown in Equation (2.1), as a microchannel definition. This length scale characterizes microchannels according to the mitigating effects of surface tension on Rayleigh-Taylor instability propagation in small channels. This definition yields a hydraulic diameter of 2.7 mm for air and water at atmospheric conditions and 0.66 mm for R-134a at 1500 kPa (Kandlikar *et al.*, 2006).

$$D_h < \sqrt{\frac{\sigma}{g\left(\rho_l - \rho_v\right)}} \qquad (2.1)$$

Kew and Cornwell (1997) assert that in boiling applications, microchannel flows are characterized by confined, elongated bubbles that occupy the major portion of the channel cross section (in contrast to conventional channels, in which multiple bubbles can occupy the cross-section). According to their definition, a microchannel is defined in relation to the size of a bubble. A number similar to the Laplace length scale, called the confinement number, was used. The confinement number is shown in equation (2.2), and the authors state that the transition criterion for microchannel consideration is $Co > 0.5$ (Kew and Cornwell, 1997). This definition yields microchannel definitions with twice the diameter of those predicted by the Laplace length scale. While these definitions are rigorous, they can be somewhat unwieldy to use; a change in operating temperature or pressure could affect the classification of a channel as a microchannel.

$$Co = \frac{1}{D_h}\sqrt{\frac{\sigma}{g\left(\rho_l - \rho_v\right)}} \tag{2.2}$$

Chung and Kawaji (2004) performed nitrogen-water flow visualization experiments in circular channels with diameters of 50 to 530 µm. For channels with hydraulic diameters of 250 and 530 µm, the flow characteristics observed were consistent in nearly every respect with those observed in the 1 mm studies described previously. Their study identified bubbly, slug, churn, slug–annular and annular flow regimes, and results for void fraction and frictional pressure drop multiplier showed good agreement with 1 mm channel results. These results were confirmed by those from Kawahara *et al.* (2005), who even suggested that channels with diameters of 250 µm and larger might be better classified as minichannels than as microchannels.

For the two smallest diameter channels studied, 50 and 100 µm, only slug flow (slug-ring and ring-slug regimes) was identified for the same range of flow conditions (liquid superficial velocities up to 10 m s^{-1} and gas superficial velocities up to 100 m s^{-1}) (Chung and Kawaji, 2004; Kawahara *et al.*, 2005). The absence of other flow regimes, namely bubbly, churn, slug–annular and annular flow, in these channels can be attributed to the greater viscous and surface tension effects in the liquid phase. This indicates the continuation of the trend described in the previous section. Furthermore, because the bubble diameters are dictated by the channel diameter, which is very small, slug bubbles are very rigid and resistant to coalescence. This is due to the fact that the pressure difference across a bubble surface, which corresponds to bubble rigidity, increases as the radius of curvature of the bubble decreases. This interfacial pressure difference must be overcome for bubbles to coalesce.

One very important observation to note is that all the studies observing flow in channels from 25 to 100 µm in diameter found that even at fixed flow rates of gas and liquid, the flow pattern in the channel is rarely constant (Kawahara, 2002; Serizawa *et al.*, 2002; Chung and Kawaji, 2004; Kawaji and Chung, 2004; Kawahara *et al.*, 2005). As opposed to studies in larger channels, in which flow regimes are relatively consistent at a given set of flow conditions, regimes typical to larger channels are rarely maintained in time; at a fixed flow condition, it may be possible to observe flow configurations sporadically changing back and forth between slug flow, annular flow, wavy annular flow, and several other patterns.

Based on the above discussion, the typical flow regime definitions are insufficient to describe flow in channels under 250 µm. As a result, some researchers have classified flows into several patterns and regimes are defined as probabilistic combinations of several flow patterns. For example, Kawahara *et al.* (2002) define four flow regimes: slug-ring, ring-slug, semi-annular, and multiple flow. These regimes are based on the time-averaged probability of three flow patterns, in this case “liquid alone”, “thin liquid film”, “ring liquid film”, “thick liquid film”, and “deformed liquid interface”. Void fraction definitions are comprised of the probability of each flow pattern and the overall mean void fraction. Several other flow pattern and flow regime names are used, depending on the author and study, and there is little uniformity in nomenclature; Serizawa *et al.* (2002) went so far as to name a flow pattern after skewered barbecue. For this reason, comparison of results between studies can be difficult.

There are several differences between microchannel flow patterns and their macrochannel equivalents. Xu et al (1999) studied flow in high aspect ratio rectangular channels with 300 µm gaps, and noted that in the slug flow pattern, more specifically a subset of slug flow the authors call slug-droplet flow, liquid droplets were observed adhering to the channel walls inside gas slugs. This indicates that at low slug velocities in these small channels it is possible for gas slugs to have dry contact with the channel walls, compared to slugs in larger channels, which are always surrounded by a continuous liquid film. This observation was confirmed by Serizawa *et al.* (2002), both in the observation of stationary slug bubbles and in slug flow at low gas flow rates.

However, at higher gas flow rates, dry contact between the gas region and the channel wall is lost, and continuous liquid films form between the gas slugs and the wall.

Another regime that differs from macrochannel flow regimes is a variation on annular flow called “liquid ring flow” (Kawahara, 2002; Serizawa *et al.*, 2002). This flow regime is distinguished from annular flow in larger channels by the fact that ring-shaped surface waves in the liquid film are carried down the length of the channel. In contrast with wavy-annular flow in larger channels, the magnitude of these surface waves can be quite large compared to the thickness of the annular film. This flow pattern is thought to form not by the perturbation of the liquid film surface, as seen in wavy-annular flow, but by gas slugs breaking through the liquid bridges between gas regions to form a long, semi-continuous gas region. The large liquid rings are the remnants of the ruptured liquid bridges.

If gas flow rate is increased further from this point, liquid ring flow is disrupted to form a new flow pattern not observed in channels that do not meet the microchannel criteria discussed earlier. This flow pattern occurs when the gas flow rate in the annular core of the liquid ring flow pattern is large enough to drive the liquid film on the walls into rivulets, leaving partially dry channel walls. This flow regime is called rivulet flow by Barajas and Panton (1993), and appears to be identical to the “rivulet” and “liquid lump” flows observed by Serizawa *et al*. (2002). In some cases this flow pattern can appear similar to the stratified flow regime found in larger channels, but it is important to note that rivulet flow is not affected by gravity and channel orientation. In fact, gravity and channel orientation are found to have no effect on flow pattern for channels smaller than 1 mm.

Rivulet flow was found by Barajas and Panton (1993) to be strongly affected by the channel surface characteristics and the surface tension of the fluid. Their study compared flow pattern transition boundaries for several surface-liquid pairings, using static contact angle for each pairing for comparison. It was found that contact angle and surface wettability had little effect on transition boundaries for slug, bubbly, and dispersed flows, but that rivulet flow only occurred in the presence of partially-nonwetting (contact angles greater than 90°) fluid-surface pairs, and in some cases for very high contact angle pairs, the liquid could be broken up into multiple rivulets. For partially-wetting fluid-surface pairs (contact angles less than 90°), rivulet flow was not observed and liquid ring flow took its place. High surface wettability facilitates the formation of continuous liquid films covering the entire channel surface. It was also noted that surface contamination with oils and debris created an artificial nonwetting effect, increasing the tendency for the liquid to form rivulets. These results were supported by those from Serizawa *et al.* (2002), who also observed effects of surface contamination.

Chung *et al.* (2004) studied the effect of channel geometry on flows in small channels by observing flows in 100 µm diameter circular channels and 96 µm hydraulic diameter square channels. The square channel results were found to be drastically different from those in circular channels due to the tendency for capillary forces to strongly retain liquid in the channel corners. This study also noted that standard void-quality correlations for larger channels did not sufficiently describe the void fraction in microchannels, which was found to be highly nonlinear due to high slip ratios. This result is supported by the results reported by Kawahara *et al.* (2002; 2005) for 50 and 100 µm diameter channels.

A summary of the two-phase flow studies discussed here is found in Table 2.3.

Table 2.3: Summary of two-phase flow literature discussed

Author(s) (Year)	D_h	Fluids	Orientation	Notes
Large channels (D_h > 25 mm)				
Griffith and Wallis (1961)			Vertical upward	• Bubbly-slug transition occurs at void fraction of ~0.25 • Transition void fractions based on packing factor of spherical bubbles • Entrance effects persist for lengths as long as L/D = 300 in two-phase flows
Fukano and Ousaka (1989)	26 mm	Air/water	Horizontal, near-horizontal	• Developed iterative physical model for prediction of annular film formation from stratified flow
Mishima and Ishii (1984)		Air/water Steam/water	Vertical	• Proposed transition criteria based on the two-fluid model and void fraction correlations • Criteria were compared with data and transition criteria from several air/water and steam/water studies; agreement was found to be satisfactory • Asserted that void fraction was a more reliable basis for regime prediction than superficial velocity or quality
Taitel and Dukler (1976)		Air/water	Horizontal	• Developed mechanistic flow regime transition correlations based on momentum balance on a stratified flow pattern and propagation of instabilities • Developed several useful dimensionless parameters based on the relative magnitudes of forces in the channel
Taitel *et al.* (1980)			Vertical	• Proposed mechanistic transition criteria for large vertical channels • Regime transition mechanisms based on bubble collision and packing, propagation of instabilities, and turbulent dispersion of large bubbles
Taitel and Barnea (1982)			Vertical countercurrent	• Developed mechanistic transition criteria for countercurrent flow of gas and liquid in large vertical pipes

Table 2.3 (continued)

Weisman *et al.* (1979)	12-51 mm	Air/water, Air/oil, Air/glycerin, Freon 113	Horizontal	• Flow regime maps and criteria developed for specific fluid pairs did not satisfactorily model the data from different fluid pairs and tube diameters • Major factor determining flow patterns in large diameter tubes was relative volumetric flow rates of gas and liquid
Wong *et al.* (1990)			Horizontal	• Developed model for prediction of CHF in horizontal flow, validated model with boiling data for water and Freon-12 • Developed curve fits and mathematical reductions of criteria from Taitel and Dukler (1976) for convenience
Minichannels (1 mm < D_h < 25 mm)				
Barajas and Panton (1993)	1.6 mm	Air/water	Horizontal	• Mapped flow regimes for four fluid/surface pairs, observed effect of contact angle and surface contamination on flow regime • Tendency for rivulet flow is strong for partially wetting fluid pairs and contaminated surfaces • Gravity effects not significant
Barnea *et al.* (1983)	4-12 mm	Air/water	Horizontal	• All transitions except for stratified to non-stratified were modeled well by criteria from Taitel and Dukler (1976)
Coleman and Garimella (1999)	1.3-5.5 mm	Air/water	Horizontal	• Tube diameter has significant effect on flow regime in tubes with D_h < 10 mm • Greater tendency for intermittent flow in smaller tubes • Compared results with criteria of Damianides and Westwater (1988), Fukano *et al.* (1989), and Weisman *et al.* (1979) • Transition mechanisms for larger tubes, such as those proposed in Taitel and Dukler (1976) may not apply in smaller tubes

Table 2.3 (continued)

Damianides and Westwater (1988)	1-5 mm	Air/water	Horizontal	• Fair agreement with Taitel and Dukler (1976) for 5 mm tubes, but poor agreement for 1 mm tubes • Noted smaller stratified flow region and decreased influence of gravity as tube diameter is reduced • Kelvin-Helmholtz model did not accurately predict transition out of stratified flow, suggesting a different transition mechanism than that for large diameter tubes • Dispersed flow transition occurs at higher velocities in smaller diameter tubes (laminarizing effect of small channels)
Fukano (1998)	1-19 mm	Air/water	Horizontal, vertical	• Observed liquid film thickness and void fraction using constant electrical current method (CECM) • Related flow pattern to void fraction signal • Developed void fraction/quality relations for several tube diameters
Fukano and Ousaka (1989)	1-4.9 mm	Air/water	Horizontal	• Flow maps and transition criteria from Mandhane *et al*. (1974), Taitel and Dukler (1976), and Weisman *et al*. (1979) cannot be applied to small tubes
Fukano and Kariyasaki (1993)	1-4.9 mm	Air/water	Horizontal Vertical upward Vertical downward	• Capillary forces become important in the range of D_h~5-9 mm • Little effect of channel orientation on flow direction; flow patterns axisymmetric at small D_h • Separated (stratified) flow not observed • Drift velocity not affected by flow direction

Table 2.3 (continued)

Ide *et al.* (1995)	0.5-6 mm circular, Rectangular channels w/ aspect ratios 1-9	Air/water	Horizontal Vertical upward Vertical downward	• Capillary forces important for channels with $D_h < 5$ mm • Flow pattern not affected significantly by flow direction/orientation • Separated (stratified) flow not observed under any conditions in horizontal flow; flow patterns were axisymmetric in circular tubes • Developed flow pattern maps for high-aspect ratio rectangular microchannels in several orientations • Transverse and longitudinal orientations did not significantly affect flow pattern in horizontal high-aspect ratio cannels
Kew and Cornwell (1997)	1.39-3.69 mm	R-141b	Vertical	• In boiling applications, the definition of a microchannel is characterized by confined, elongated bubbles that occupy the major portion of the channel cross section
Mishima and Hibiki (1996)	1-4 mm	Air/water	Vertical	• Flow regime boundaries reproduced by models from Mishima and Ishii (1984) • Predicted channel void fraction with drift-flux model using zero drift velocity and a diameter-dependent distribution parameter correlation
Tabatabai and Faghri (2001)	1-15.88 mm	Air/water, R-12, R-113, R-22, R-134a	Horizontal	• Flow regime maps with transition boundaries adjusted for relative effects of surface tension, buoyant forces, and shear • Criteria compared with data from several studies; yielded improved agreement for small channels
Thome *et al.* (2004)	0.77-3.1 mm	R-11, R-12, R-113, R-123, R-134a, R-141b and CO2	Vertical	• Developed three-zone model for evaporation of elongated bubbles in microchannels • Proposed microchannel definition based on the size of a departing bubble • Compared three-zone model results with data from several vertical tube boiling studies

Table 2.3 (continued)

Microchannels (D_h < 1 mm)				
Chung and Kawaji (2004)	50-530 µm	Nitrogen/ water	Horizontal	• Two-phase flow characteristics change significantly between 100 and 250 µm • Flow patterns in 250 and 540 µm channels were similar to those in 1 mm channels • Slug flow dominant in channels 100 µm and smaller • Void fraction/quality relationship is highly nonlinear in small channels
Chung *et al.* (2004)	100 µm circular 96 µm square	Nitrogen/ water	Horizontal	• Flow regimes are probabilistic; flow patterns not constant at constant flow conditions • Surface tension effects in square channels draw liquid into corners • Large velocity slip; void fraction/quality relationships are nonlinear
Kawahara (2002)	100 µm	Nitrogen/ water	Horizontal	• Intermittent, annular, ring-film flow patterns observed • Flow regimes defined as probabilistic combinations of flow patterns • Absence of bubbly and churn flows, gravitational effects also absent • Weak momentum coupling (high slip) between phases
Kawahara *et al.* (2005)	50-251 µm	Nitrogen/ water Nitrogen/ ethanol-water	Horizontal	• Void fraction for channels with D_h<100 µm agree with Kawahara *et al.* (2002) • Void fraction for channels with D_h~250 µm agree with Armand *et al.* (1946) • Liquid properties did not significantly affect void fraction
Kawaji and Chung (2004)	100 µm	Nitrogen/ water	Horizontal	• Compiled data from Kawahara *et al.* (2002), Chung *et al.* (2003), and others

Table 2.3 (continued)

Serizawa *et al.* (2002)	20-100 μm	Air/water Steam/water	Horizontal	• Uses numerous terms to define flow patterns; correcting for non-standard nomenclature, results show fair agreement with other studies with $D_h < 1$ mm • Claimed agreement with flow regime maps from much larger tubes despite apparent disagreement • Proposed several alternate transition mechanisms that differ from those in channels ~1mm • Surface tension effects dominant; bubbles highly spherical and rigid, resistance to coalescence • Noted appearance of what other authors have called rivulet flow; dry patches on walls at high gas velocities
Xu *et al.* (1999)	0.3-1 mm	Air/water	Vertical upward	• Bubbly flow absent in smallest channel • Used transition criteria from Mishima and Ishii (1984) for narrow rectangular geometry
Zhao and Bi (2001)	0.866-2.886 mm triangular	Air/water	Vertical upward	• Trends agreed with smaller diameter channel studies (e.g. Ide *et al*. (1997), Mishima and Hibiki (1996)) but not with those for larger diameters (e.g. Taitel and Dukler (1976) and Mishima and Ishii (1984)) • Strong surface tension effects due to acute angle corners in channel • Dispersed bubbly flow not observed in smallest channel

2.3 Deficiencies in literature and scope of the present work

Temperature swing adsorption cycles have thus far been considered inapplicable for industrial gas separations applications, primarily due to the difficulties associated with effectively heating and cooling large amounts of non-conductive adsorbent materials. Some attempts to improve heat and mass transfer performance of TSA systems have been successful, but these improvements have been insufficient to make TSA a viable technology for large-scale gas separations. Of the process modifications investigated, those making use of adsorbent-laden microchannels (in the form of monoliths or hollow fiber modules) in lieu of the more traditional packed bed configuration show the most promise for heat transfer enhancement. However, several of the most promising concepts face significant challenges in fabrication.

The concept investigated in the present work attempts to avoid these fabrication difficulties through the use of channels that convey both the feed gas and the liquid heat transfer fluid, thereby eliminating the need to plumb individual microchannels and greatly reducing system footprint. The potential advantages of this system are significant, but the use of adsorbent channels designed to accommodate both gas and liquid is a concept that has yet to be understood adequately. It is expected that the mass transfer performance of the channel will be significantly affected by the interaction of the liquid and gas phases during the process steps involving transient displacement of liquid by gas and gas by liquid in the 200 μm adsorbent channels. A thorough investigation of the TSA gas separation concept under consideration requires understanding of the liquid-gas interactions during displacement, the behavior of residual liquid on the channel walls after displacement, and the effect of these liquid films on system mass transfer performance.

Compared to the body of literature available for large diameter tubes and minichannels, there is a relative scarcity of knowledge about multiphase flow in channels with D_h ~ 100 μm. The available studies have investigated flow regime transitions, void fraction-quality relations, pressure drop, and heat transfer in these channels, but no studies to date have attempted to understand transient multiphase flow phenomena such as the sequential displacement of liquid and gas phases under consideration here. Furthermore, while some authors have made observations concerning liquid films and liquid-wall interactions in microchannel flow, none have attempted to quantify the behavior of these films.

2.4 Research objectives

The present study aims to address these gaps in the literature through the investigation of the multiphase flow phenomena at work during the displacement of liquid by gas and the displacement of gas by liquid in a vertical 200 μm channel. This includes the following:

- Modeling of bulk fluid movement during transient two-phase displacement.
- An air-water flow visualization study for the observation of interface velocity, flow pattern, and liquid film thickness during two-phase displacement in 200 μm channels.
- The measurement of liquid-gas interface velocity and residual liquid film thickness during the displacement processes. This is accomplished using the image analysis techniques described in Keinath and Garimella (2010).
- The assessment of the impact of residual liquid on system mass transfer performance. This is accomplished through the development of computational models for heat, mass, and momentum transfer in an adsorbent channel.

CHAPTER 3

MODELING

This section provides a detailed description of the modeling of two-phase fluid displacement in a microchannel, as well as coupled heat and mass transfer modeling for simulation of a microchannel adsorption process. First, fluid flow models for displacement were developed using an incompressible assumption for the gas phase. The purpose of this modeling effort was to obtain approximate fluid velocities for use in predicting flow regimes from correlations in the literature. A comparison of diffusion properties of polymer materials and fluids was performed to validate fundamental assumptions for the development of mass transfer models. More detailed models for the displacement of gas and liquid from the channel were then developed for use in full process simulations. These models used compressible flow calculations for the gas phase in the channel along with fully coupled solution of continuity, momentum, species conservation, and property variations through the respective processes. The results of these models are discussed, and in subsequent chapters, these models are validated by data from flow visualization experiments. Finally, the development of a heat and mass transfer model is outlined for the purpose of demonstrating the effects of residual liquid films retained on the channel walls. The effects of these films on mass transfer performance are discussed.

3.1 Incompressible flow modeling and flow regime predictions

Initial modeling efforts were directed toward determining approximate fluid velocities during the displacement of liquid by gas and gas by liquid for the purpose of predicting two-phase flow regimes based on correlations from the literature. By obtaining a range of likely velocities and knowing the properties of each fluid, it was possible to compare the flow parameters against available flow regime maps and transition criteria. The literature typically pertains to the behavior of simultaneously supplied mixed two-phase flows in microchannels, but to date, the transient two-phase displacement scenario in this study has not been addressed. Despite the differences in these flow configurations, an understanding of the flow regimes that occur at similar flow conditions provides some guidance on the applicable flow patterns during displacement, and the dominant forces at work.

For simplicity, properties for water and each of the feed gas components (CH_4, CO_2, and H_2S) were calculated using the thermodynamic functions available in Engineering Equation Solver (EES) (Klein, 1992-2012), and the feed gas mixture was assumed to be an ideal gas mixture, as shown in Equation (3.1) for the purpose of determining density. Mixture viscosity was calculated based on Equation (3.2). Table 3.1 shows the values used for these calculations. Channel inlet and outlet pressures were assumed to be 5500 and 5400 kPa, while feed gas concentrations were assumed to be 70% CH_4, 20% H_2S, and 10% CO_2 by mole fraction. (Thus, inlet and outlet pressures were both specified, and the flow rates required to satisfy these conditions were calculated.)

Table 3.1: Parameters used for calculation

Parameter	Value	Units
P_{in}	5500	kPa
P_{out}	5400	kPa
P_{avg}	5450	kPa
R_u	8.314	J mol^{-1} K^{-1}
T	25	°C
C_{CH4}	0.7	- (mole fraction)
C_{CO2}	0.1	- (mole fraction)
C_{H2S}	0.2	- (mole fraction)
M_{CH4}	16.04	kg mol^{-1}
M_{CO2}	44.01	kg mol^{-1}
M_{H2S}	34.08	kg mol^{-1}
μ_{CH4}	11.2×10^{-6}	kg m^{-1} s^{-1}
μ_{CO2}	17.3×10^{-6}	kg m^{-1} s^{-1}
μ_{H2S}	12.1×10^{-5}	kg m^{-1} s^{-1}

$$\rho_{mixture} = \frac{P_{avg}\left(C_{CH_4}M_{CH_4} + C_{CO_2}M_{CO_2} + C_{H_2S}M_{H_2S}\right)}{R_U T} = 50.68\ \mathrm{kg\cdot m^{-3}} \tag{3.1}$$

$$\mu_{mixture} = \frac{\sum C_n \mu_n \left(M_n\right)^{1/2}}{\sum C_n \left(M_n\right)^{1/2}} = 3.95\times10^{-5}\ \mathrm{kg\cdot m^{-1}s^{-1}} \tag{3.2}$$

Because both the liquid and the gas were assumed to be incompressible for the purpose of this initial modeling effort, it was possible to use a simple two-node model, with a single node assigned to each phase. A schematic of this model is shown in Fig. 3.1. The model also assumed no mixing or interaction of the two phases at the liquid-gas interface, essentially approximating the displacement of each phase as the movement of a piston down the length of the channel. The fluid motion was determined using the conservation of momentum, shown in Equation (3.3) below. Friction factors are calculated using the Churchill (1977) correlation, modified for the square channel cross-sectional geometry. The Churchill friction factor correlation and other correlations used can be found in Appendix A.

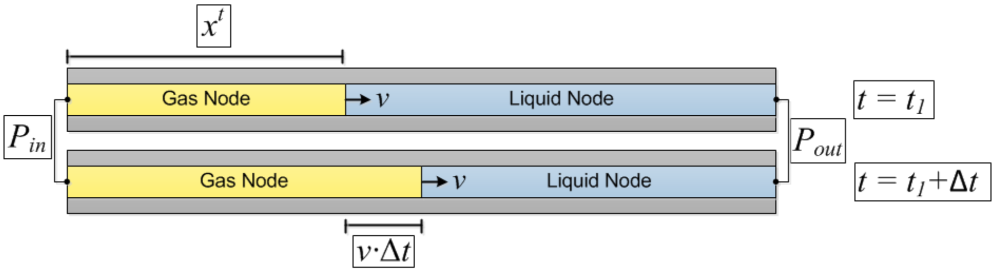

Figure 3.1: Schematic of the incompressible two-node displacement model.

$$\begin{aligned} \Delta P^{t+\Delta t} &= \left(\frac{dP}{dx}\right)_L \left(x^t + v\cdot\Delta t\right) + \left(\frac{dP}{dx}\right)_G \left(L - \left(x^t + v\cdot\Delta t\right)\right) \\ \left(\frac{dP}{dx}\right)_L &= f_L \frac{\rho_L v^2}{2D_h} \\ \left(\frac{dP}{dx}\right)_G &= f_G \frac{\rho_G v^2}{2D_h} \end{aligned} \tag{3.3}$$

The results obtained from this model are shown in Fig. 3.2 and 3.3. A constant driving pressure drop of 1 bar (100 kPa) was assumed and the channel length was taken to be one meter long. It was determined that the minimum and maximum fluid velocities are approximately 0.25 m s^{-1} and 4.6 m s^{-1}, respectively. It is important to note that the total pressure drop in the channel is dominated by the pressure drop in the liquid phase. Because the incompressible and no-mixing assumptions dictate that both fluids are moving at the same velocities at all times, and because the density and viscosity of the liquid phase are significantly higher than those of the gas phase, the pressure gradient in the liquid region is much larger than in the gas region. As a result, to maintain the same total pressure drop across the channel, the velocity increases sharply as more liquid is displaced from the channel, or decreases as more liquid enters the channel.

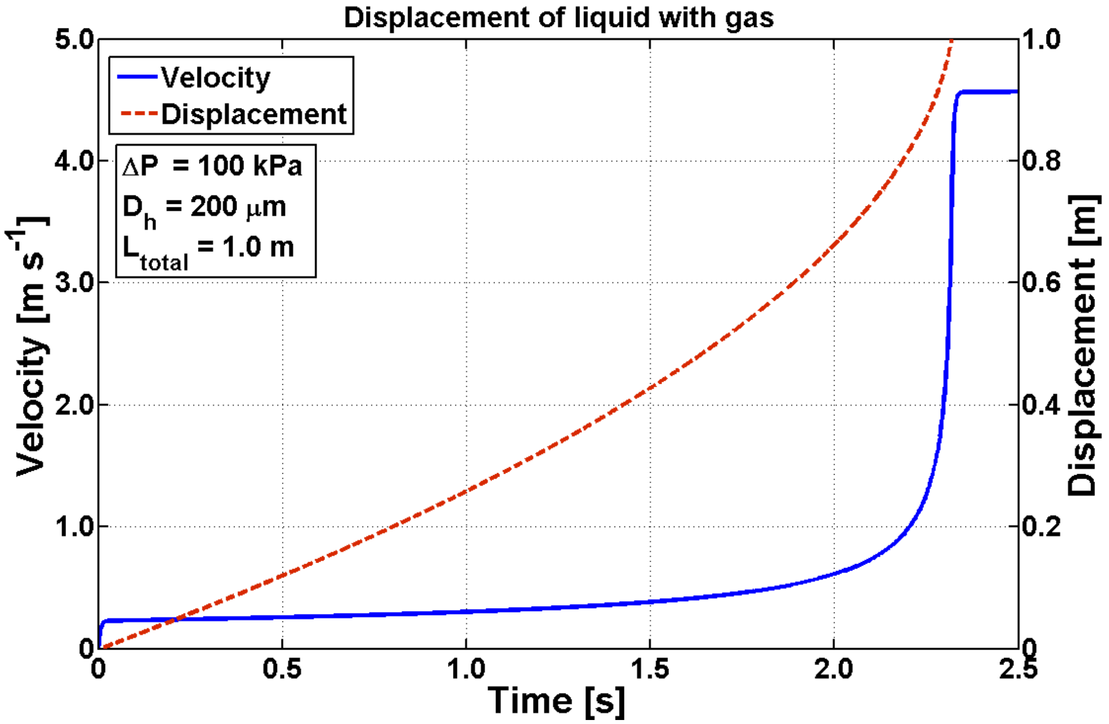

Figure 3.2: Fluid velocity and liquid-gas interface location during the displacment of liquid by gas using the incompressible flow model.

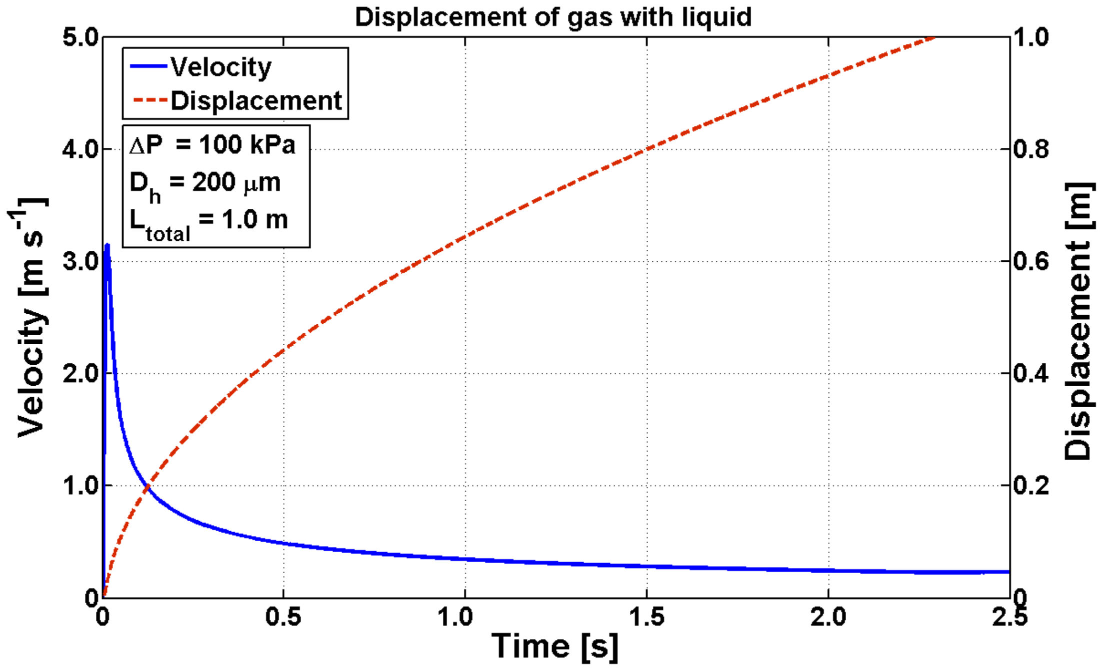

Figure 3.3: Fluid velocity and liquid-gas interface location during the displacment of gas with liquid using the incompressible flow

The approximate velocities obtained from the model were used to predict the two-phase flow characteristics at the liquid-gas interface based on the transition criteria and data from several sources in the literature for similar channel dimensions. One key assumption used here is that the liquid and gas superficial velocities are equal. Because the liquid and gas at the inlet are not simultaneously supplied, the superficial velocity of the displaced phase might be considered zero at any point in the gas-filled region, as shown in Figure 3.4. However, using the piston-displacement assumption, the flow rates of liquid and gas at the liquid-gas interface are equal. Because this is the only location at which the two phases interact, the superficial velocities of the two phases can be considered equal in the immediate vicinity of the interface.

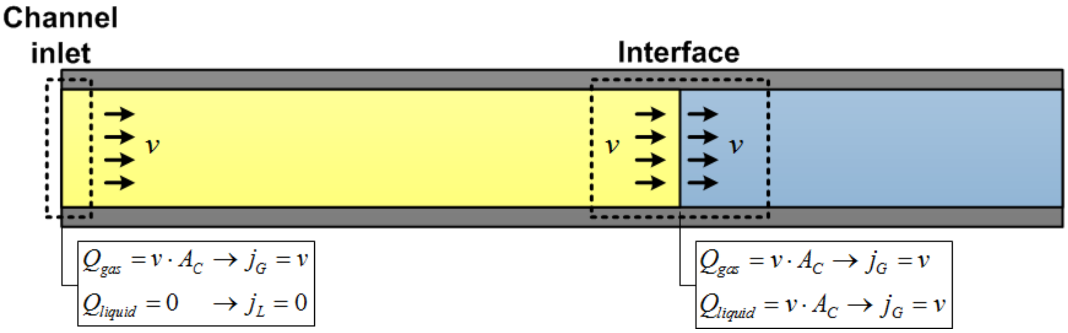

Figure 3.4: Illustration of superficial velocities of liquid and gas at the channel inlet and the liquid-gas interface.

The first study used for flow regime prediction was that of Coleman and Garimella (1999), who observed two-phase flow regimes in tubes as small as 1.3 mm in diameter. In this study, it was found that the flow regime transition criteria proposed by Weisman et al (1979), which included adjustments for tube diameter and fluid properties, provided the closest agreement with the data. These flow regime criteria are shown in the equations below; Equations (3.4), (3.5), and (3.6) indicate the conditions for transitions from annular to dispersed flow, stratified to intermittent flow, and stratified to annular flow, respectively.

$$1 \le \left(\frac{1}{9.7}\right)\left[\frac{(dP/dx)_L^S}{(\rho_L-\rho_G)g}\right]^{\frac{1}{2}}\left[\frac{D_h(\rho_L-\rho_G)g^2}{\sigma}\right]^{\frac{1}{4}} \tag{3.4}$$

$$1 \le \frac{4u_L^S}{\left(u_G^S\right)^{0.1}\sqrt{g\cdot D_h}} \tag{3.5}$$

$$1 \le \frac{1}{1.9}\left(\frac{u_L^S}{u_G^S}\right)^{\frac{1}{8}}\left[\frac{u_G^S\sqrt{\rho_G}}{\left(g(\rho_L-\rho_G)\sigma\right)^{\frac{1}{4}}}\right]^{0.2}\left(\frac{u_G^S}{g\cdot D_h}\right)^{0.18} \tag{3.6}$$

The modeled results were used for evaluation of these equations and it was found that the conditions for both annular and intermittent flow were satisfied over the entire range of predicted velocities. It should be noted that while this set of criteria produced greater agreement with the data than other available correlations, its agreement with the data decreased with tube diameter. As a result, while these transition criteria properly capture the general transition phenomena, their results are not definitive for tube diameters as small as 200 μm. Therefore, the flow conditions determined for displacement were also compared against the data of Coleman and Garimella (1999) for the smallest tube diameter (1.3 mm). Fig. 3.5 shows the flow regime map from Coleman and Garimella, obtained from air-water results for 1.3 mm diameter tubes. The region of interest based on the calculated values is highlighted by the red box. It should be noted that while the highlighted region on the flow regime map does not indicate a transition to annular flow, the axes of the flow map, which shows transitions for air and water, do not take into account fluid properties, while the transition criteria do. Because the gas in this case has properties very different from air (approximately 40 times the density of atmospheric air at 25°C), the transition criteria yield different results.

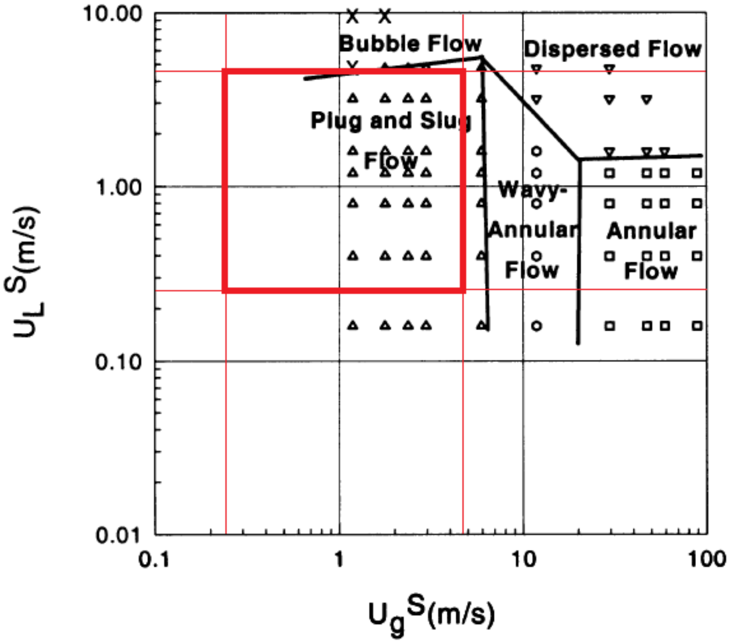

Figure 3.5: Flow regime map from Coleman and Garimella (1999), with box indicating relevant flow conditions superimposed in red.

The transition correlations from Weisman et al (1979) predict either annular or intermittent flow at the given flow conditions, but from the criteria alone it cannot be determined which of these regimes is more likely. The flow regime map indicates that for the fluid velocity range predicted by the incompressible displacement model the flow will be within the intermittent regime. This finding would seem to indicate that during the displacement process, the incoming slug of gas is likely to maintain a stable interface with the liquid with little mixing of the two phases. It is important to note that the 1.3 mm tubes observed by Coleman and Garimella (1999) are significantly larger than the 200 μm channels used in this work, and flow regime transitions may occur at different conditions.

Nema (2007) proposed flow regime transition criteria for condensing flow in microchannels based primarily on modified dimensionless parameters with relevance to flow in small channels. The key parameters used for the transition criteria relevant to this study are the Bond number (3.7), critical Bond number (3.8), Weber number (3.9), Martinelli parameter (3.10), modified Martinelli parameter (3.11), slug flow Martinelli parameter (3.12), and minimum liquid volume fraction for slug formation (3.13). Relevant transition criteria are listed in Table 3.2.

$$Bo = \frac{\left(\rho_L - \rho_G\right) g \cdot {D_h}^2}{\sigma} \tag{3.7}$$

$$Bo_{crit} = \left[\left(\frac{\rho_L}{\rho_L - \rho_G}\right) - \frac{\pi}{4}\right]^{-1} \tag{3.8}$$

$$We_G = \frac{\rho_G u_G^S D_h}{\sigma} \tag{3.9}$$

$$X_{tt} = \frac{\dot{m}_l}{\dot{m}_g}\sqrt{\frac{\rho_g}{\rho_l}} \tag{3.10}$$

$$X_{tt,mod} = X_{tt} - X_{tt,slug} \tag{3.11}$$

$$X_{tt,slug} = \begin{cases} X_{tt} & \text{if} \quad Bo \le Bo_{crit} \\ X_{tt,0} + \dfrac{X_{tt}\left(Bo - Bo_{crit}\right)}{Bo - Bo_{crit} + e} & \text{if} \quad Bo > Bo_{crit} \end{cases} \tag{3.12}$$

$$X_{tt,0} = 0.3521 \tag{3.13}$$

Table 3.2: Flow regime transition criteria from Nema (2007)

Transition	Criteria
Annular flow	$We_G > 6 \wedge Bo \le Bo_{crit}$ or $We_G < 6 \wedge Bo \le Bo_{crit} \wedge X_{tt} < X_{tt,0}$
Wavy flow	$We_G > 6$ or $We_G < 6 \wedge X_{tt} < X_{tt,0}$
Intermittent flow	$We_G < 35 \wedge X_{tt} > X_{tt,slug}$

These criteria predicted intermittent flow for fluid velocities less than 2.5 m s^{-1} (flow velocities are assumed to be equal for gas and liquid). For velocities greater than 2.5 m s^{-1}, the criteria predicted both annular flow and intermittent flow; however, Fig. 3.6 shows that when compared to data from several studies, the intermittent flow criterion returned false positives for intermittent flow at the upper end of the expected velocity range. This indicates that according to these transition criteria, annular flow is predicted for velocities greater than 2.5 m s^{-1}.

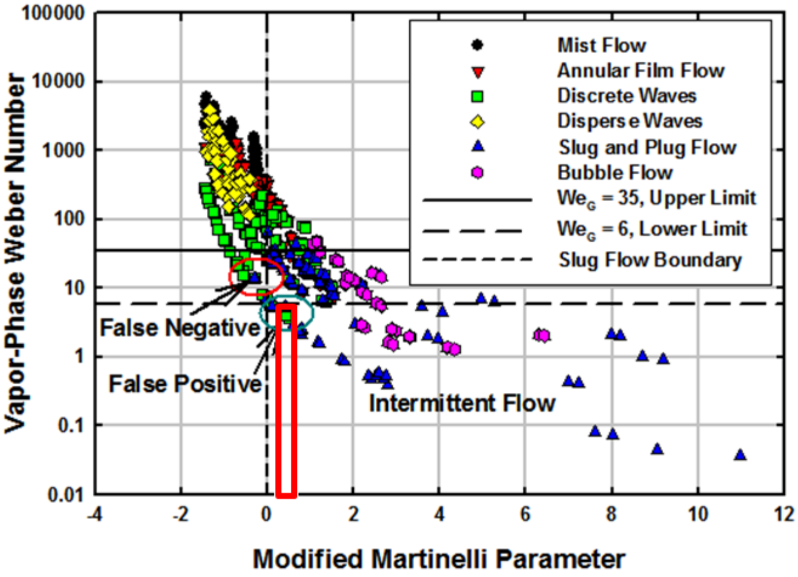

Figure 3.6: Experimental data from several studies, compiled by Nema and plotted along with flow regime transition lines. The expected range of flow conditions ($X_{tt,mod} = 0.34$, $0.5 < We_G < 11.8$) is highlighted by the red box.

The flow conditions were then compared with the experimental results obtained by Serizawa et al (2002) and Cubaud and Ho (2004). These two studies performed flow regime identification experiments on channels far smaller than those observed in the aforementioned studies, with hydraulic diameters from 25 to 525 μm, and with both square and circular channel geometries. While the experimental conditions from Cubaud and Ho (hydraulic diameters of 200 and 525 μm) did not extend to the flow conditions expected for displacement in the present study, they did note that the transition from slug/intermittent flow to annular flow occurs only when the gas superficial velocity is far greater than that of liquid; because the gas and liquid superficial velocities in displacement are considered to be equal, this would seem to indicate a tendency towards intermittent flow. Furthermore, this study reinforces the findings of other studies, which note a strong tendency towards intermittent flow in such small channels. Fig. 3.7 shows the experimental flow regime map from Serizawa et al. (2002), which also indicates that slug/intermittent flow is dominant in the relevant velocity range.

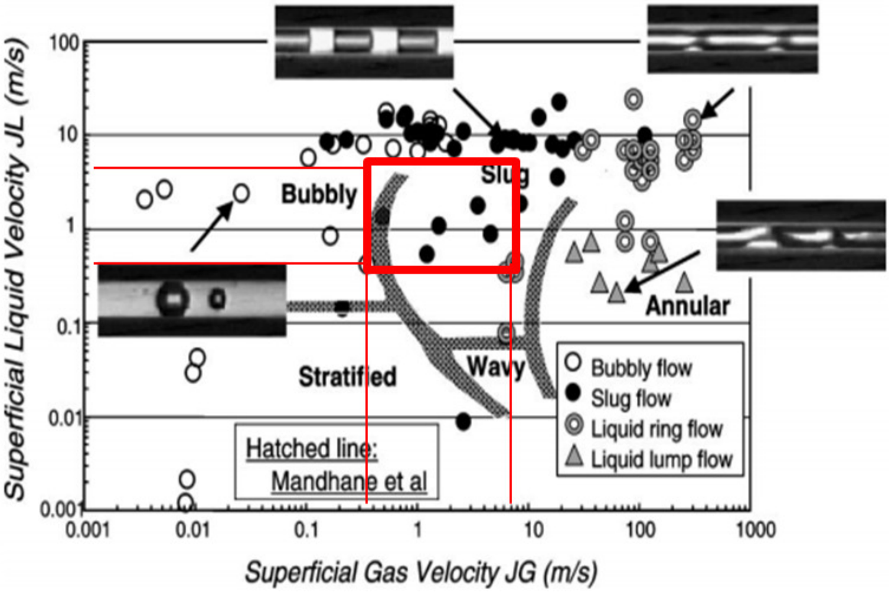

Figure 3.7: Flow regime map from Serizawa et al. (2001). The relevant flow velocity range is highlighted by the red box.

The above discussion indicates a high likelihood that the flow in the channel during displacement would remain within the intermittent flow regime, with the possibility of annular flow at the high end of the velocity range predicted by the incompressible displacement model. However, given the scarcity of data in the relevant velocity and hydraulic diameter range, and the lack of prior studies on the sequential flow of the phases, this finding is far from conclusive. Furthermore, while the literature indicates that slug-like behavior will be observed during displacement, these studies provide little insight into the presence or absence of liquid films between the gas slugs and the channel walls. The limits of the existing body of work reinforce the need for the flow visualization experiments discussed in the following chapter.

3.2 Heat and mass transfer resistance estimations

An order of magnitude analysis was performed to determine the relative magnitudes of the heat and mass transfer resistances in the channel. This comparison of major heat and mass transfer resistances provides important information about the heat and mass transfer pathways that govern or limit the adsorption process and those that can be effectively ignored in the development of a model.

Diffusion coefficients for CO_2 and H_2S through water and several common polymer membrane materials were collected from literature and analyzed (Hines and Maddox, 1985; Tamimi *et al.*, 1994). Because no specific material data were available for the membrane-adsorbent matrix to be used in the channels, polymer property data were obtained for several rubbery and glassy polymers commonly used in separations involving CO_2 and H_2S. These materials are listed in Table 3.3. Because diffusion properties are temperature-dependent, diffusion coefficients were evaluated over a range of temperatures.

Table 3.3: Materials analyzed in mass transfer resistance comparison.

Diffusing gas: H_2S		Diffusing gas: CO_2	
Material	**D at 30 °C ($m^2\ s^{-1}$)**	**Material**	**D at 30 °C ($m^2\ s^{-1}$)**
Water	22.0	Water	20.7
Nylon	3.0×10^{-6}	Isoprene acrylonitrile 74/26	4.15×10^{-4}
Plasticized cellulose acetate	2.2×10^{-5}	Butyl rubber	3.32×10^{-5}
Unplasticized cellulose acetate	1.0×10^{-6}	Poly(dimethyl butadiene)	1.08×10^{-4}
Poly(vinyl trifluoroacetate)	4.4×10^{-5}	Butadiene acrylonitrile	2.07×10^{-5}
Mylar A	8.1×10^{-7}	Polybutadiene	2.43×10^{-4}
Saran	8.0×10^{-7}		

Diffusion coefficients are shown in Fig. 3.8. Regardless of the polymer analyzed, diffusion of the gases through polymer membranes is found to be the dominant mass transfer resistance, with diffusion coefficients several orders of magnitude lower than those for diffusion through water. Practically, this means that in modeling efforts, the radial diffusion of species in the flow area of the channel is not significant, as the diffusion of CO_2 and H_2S through water is orders of magnitude faster than diffusion through the membrane material on the walls. This means that phenomena in the flow area of the channel can be safely modeled as one-dimensional, ignoring radial variations in concentration, which will be insignificant.

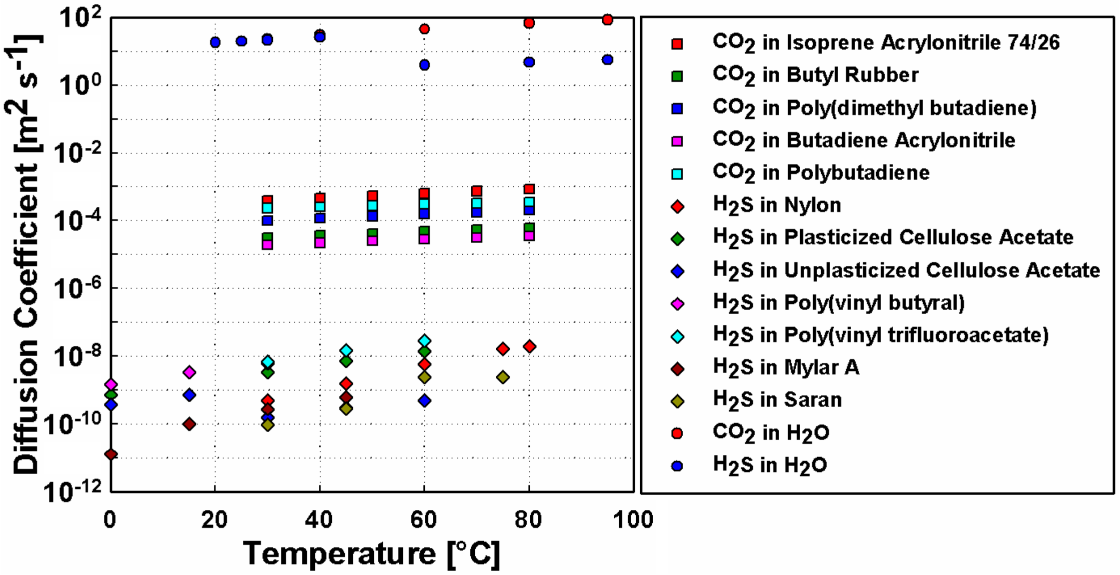

Figure 3.8: Diffusion coefficient for diffusion of CO_2 and H_2S through various polymer membrane materials and water.

For radial variations to be fully neglected in a discretized model, it is also necessary to verify that the heat transfer resistances in the liquid and the adsorbent have different relative magnitudes. To obtain a basic comparison of heat transfer resistances, heat convection resistances for internal flow of water in the channel were compared to heat conduction resistances through a typical adsorbent material. Fluid properties were determined using the property lookup routines in Engineering Equation Solver (EES) (Klein, 1992-2012). The thermal conductivity of the adsorbent material was taken to be 0.17 W $m^{-1}K^{-1}$, consistent with the data published by Hu *et al.* (1997), who tested thermal conductivity of adsorbent polymer-zeolite composites. Conductive thermal resistance was calculated according to Equation (1.15) using the formula for characteristic length shown in Equation (1.14).

$$\delta = \frac{V_{body}}{A_{surface}} = \frac{A_{cs,cond}}{P_{wetted}} = \frac{\left(D_h + t_{wall}\right)^2 - D_h^{\,2}}{4D_h} = 150\ \mu m \qquad (1.14)$$

$$R_{cond} = \frac{\delta}{k_{adsorbent}} = 8.8\times10^{-4}\ m^2K\cdot W^{-1} \qquad (1.15)$$

The convective heat transfer resistance was calculated using the maximum fluid velocity predicted by the incompressible flow model (4.6 m s^{-1}), and the flow was assumed to be fully developed. To verify this assumption, the hydrodynamic entry length was calculated and found to be 0.126 m, meaning that for a 1.0 m long channel, the flow is fully developed for approximately 87% of the channel length. This calculation is shown in Equation (1.16) and (1.17).

$$Re_{max} = \frac{\rho v_{max} D_h}{\mu} = \frac{4.6\left(2 \cdot 10^{-4}\right)}{1.002 \cdot 10^{-3}} = 1034 \tag{1.16}$$

$$x_{fd} = 0.1 Re_{max} \cdot Pr \cdot D_h = 0.13\, m \tag{1.17}$$

The convective heat transfer resistance was then calculated using the average of the fully developed Nusselt numbers for constant wall temperature and constant heat flux boundary conditions, as shown in Equation (1.18).

$$R_{conv} = \frac{1}{h_{fd}} = \frac{2D_h}{\left(Nu_{fd,T} + Nu_{fd,q}\right)k} = 8.2 \times 10^{-5}\ m^2 K \cdot W^{-1} \tag{1.18}$$

The heat conduction resistance in the adsorbent layer was found to be approximately 10 times greater than the heat convection resistance in the liquid flow, implying that heat transfer is much more effective through the water than through the adsorbent. Similarly to the mass transfer comparison, radial variations in temperature in the flow channel may be neglected.

3.3 Compressible flow modeling

Computational models were developed in the gPROMS platform to simulate the fluid flow behavior in the channel during the displacement processes (Process Systems Enterprise, 1997-2009). These models are valuable both as process modeling tools, providing predictions of interface velocities and cycle times, and as a framework for more detailed models incorporating fully-coupled process simulations of heat and mass transfer behavior. These models are validated using data obtained in the experimental flow visualization study described in the following chapter.

The model utilizes an implicit finite volume approach to iteratively solve one-dimensional fluid flow and species conservation equations for the displacement process. The movement of the fluid along the channel length is tracked using an axial discretization scheme that is updated at each time step to accurately model the movement and segregation of the gas and liquid phases.

Initial attempts to simulate the fluid behavior using a stationary mesh revealed several difficulties associated with the tracking of the liquid-gas interface and the numerical propagation of fluid property data across the liquid-gas boundary. In a fixed mesh domain, the liquid-gas interface does not necessarily coincide with control volume boundaries, making it necessary to compute average fluid properties in control volumes containing both liquid and gas. A schematic of this scenario is shown in Figure 3.9.

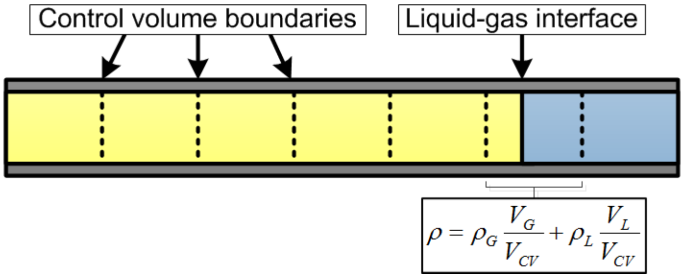

Figure 3.9: Schematic of a fixed mesh scheme during two-phase displacement. Properties in the control volume in the vicinity of the liquid-gas interface must be averaged.

The large difference in fluid densities and viscosities across the interface, as well as difficulty in precisely determining the interface location through numerous iterations, resulted in the propagation of erroneous data on either side of the interface and ultimately an inability to accurately represent fluid behavior in the channel. This effect can be seen in Figure 3.10, in which a stationary mesh was used and displacement was modeled as a compressible flow of a four-component mixture (CH_4, CO_2, H_2S, and H_2O), and properties in the interfacial control volumes were averaged on a volume basis according to the equation shown in Figure 3.9.

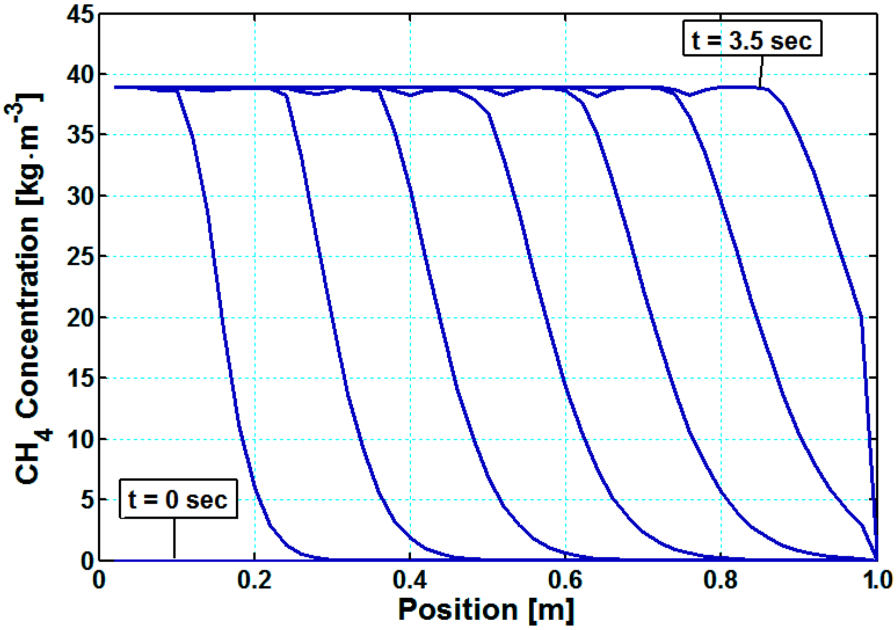

Figure 3.10: Methane concentration vs. time, as computed by the stationary mesh model. The change in CH_4 concentration across the liquid-gas interface becomes smoother and less distinct through time, indicating artificial diffusion of fluid property data.

The erroneous diffusion of property data across the liquid-gas interface can be seen in Figure 3.10 by the loss of interface resolution through time. While in reality the liquid-gas interface should appear as a step-like discontinuity in concentration, indicating the transition from the gas region (high concentration of CH_4) to the liquid region (near-zero concentration of CH_4), the liquid-gas interface appears as a rounded, gradual transition between the high and low concentrations. The liquid-gas interface becomes less distinct through time as the averaged property data spreads to neighboring control volumes.

A dynamic meshing technique was employed to minimize the problem of numerical diffusion and provide accurate interface tracking. This method re-discretized the computational domain after each time step to account for the movement of the interface. The region of the channel occupied by gas was divided into a fixed number of control volumes at all times, so that the size of the gas region changes in time and the control volumes stretch to accommodate the lengthening gas region. This discretization scheme is depicted in Fig. 3.11. Because the control volumes change size to fit the actual length of the gas-occupied region, the re-discretization process ensures that a control volume boundary always exists precisely at the interface location. This approach provides two essential benefits: (1) the ability to accurately and smoothly track the liquid-gas interface location without interpolation within a control volume, and (2) the ability to effectively segregate the fluid property calculations between phases, eliminating the propagation of erroneous data across the interface. Only a single control volume in necessary in the liquid region due to the fact that water is treated as an incompressible fluid, and as such, its properties do not vary along the channel length.

Figure 3.11: Illustration of the axial discretization scheme for two consecutive time steps. The control volumes in the gas region change size such that a discrete, well-defined boundary always exists at the liquid-gas interface.

This dynamic meshing technique addresses the key shortcomings of the fixed-mesh scheme discussed previously, but poses challenges in coupling the fluid flow calculations to heat and mass transfer calculations in the adsorbent wall. Because the control volume sizes and locations are not constant, coupling of the channel flow model to models for the adsorbent wall would require complicated spatial interpolations to properly account for the exchange of heat and mass between the stationary wall and the moving fluid. These spatial interpolations add complexity to coupled heat and mass transfer calculations, increase computational load, and may cause computational instabilities.

The boundary conditions for the channel are known values and can be expressed explicitly in the model. These include the inlet and outlet pressures, which are fixed, the inlet fluid temperature, and the inlet gas concentrations from the feed source. Other relevant known values include the channel dimensions and molar masses of each species. These too are expressed explicitly. These known values are shown in Table 3.4.

Table 3.4: Known values and properties.

P_{in}	5.5×10^6	Pa
P_{out}	5.4×10^6	Pa
T_{in}	25	°C
$C_{CH4,in}$	0.7	mol mol^{-1}
$C_{CO2,in}$	0.1	mol mol^{-1}
$C_{H2S,in}$	0.2	mol mol^{-1}
M_{CH4}	16.043	kg kmol^{-1}
M_{CO2}	44.010	kg kmol^{-1}
M_{H2S}	34.082	kg kmol^{-1}

Also defined explicitly are the discretization and calculation parameters, which include the number of spatial divisions, time step size, and the initial state. The assumed initial state consists of a 1.0 meter long, nearly liquid-filled channel (1 mm at the inlet end is occupied by gas), in which all the fluid is at rest. The average roughness of the channel is assumed to be 0.5% of the hydraulic diameter (1 μm), consistent with a smooth tube assumption. The parameter values used for the present sample calculation are summarized in Table 3.5.

Table 3.5: Calculation parameters

N_X	51	Number of axial divisions (50 gas, 1 liquid)
L_{TOT}	1.0 m	Total channel length
$L_{G,0}$	0.001 m	Initial gas region length
D_H	200 μm	Hydraulic diameter (square channel)
e/D_H	0.005	Relative roughness
v_0	0 m s^{-1}	Initial fluid velocity

Because the number of gas nodes is constant throughout time, all of the gas nodes are contained within the 1 mm long gas region in the initial time step. The lengths and locations of these gas control volumes change rapidly with respect to time as the liquid-gas interface begins moving; therefore, very small time steps are necessary to ensure computational stability. However, as the gas region elongates, the length of the channel occupied by gas, and consequently the gas node lengths, changes less rapidly with time, making such small time steps unnecessary. To ensure computational stability without creating an unnecessarily large computational load, gPROMS employs an adaptive time stepping algorithm that computes results for several time step sizes, reducing the step size until the calculation produces an acceptably small error. The step size is periodically reassessed and adjusted by the program as the calculation continues (Process Systems Enterprise, 1997-2009).

Once the explicitly defined values are specified, the conservation equations can be evaluated and solved iteratively for each timestep. Continuity, momentum conservation, species conservation, and the Peng-Robinson gas equations of state are iteratively solved at each node in order to determine the density, velocity, pressure, and concentration in each control volume (Peng and Robinson, 1976; Robinson *et al.*, 1985). Properties and mixing parameters used for solution of the Peng-Robinson equation of state are determined by the Multiflash property package in gPROMS (Process Systems Enterprise, 1997-2009). The iterative calculations and the advancement to subsequent time steps are performed in gPROMS. When the solution for a time step converges to a stable solution, the data are saved and the calculation for the next time step begins. Time step length is varied by gPROMS to maintain stability during rapid variation in calculated values. After a solution is complete, postprocessing calculations are performed using the calculated variable values to determine important process parameters such as outlet purity and mass flux at the channel outlet.

The following section outlines the iterative calculations involved in determining the solution for a single time step. First, to calculate the inlet density from the inlet pressure and concentrations, it is necessary to determine the equivalent molar mass of the gas mixture. Equation (3.19) determines the average molar mass of the gas mixture from the component molar masses and mass fractions. Equation (3.20) uses this result to calculate the gas mixture density from the Peng-Robinson equation of state.

$$M_{EQ} = C_{CH_4} M_{CH_4} + C_{CO_2} M_{CO_2} + C_{H_2S} M_{H_2S} \tag{3.19}$$

$$\rho_{in} = \rho_{Peng-Robinson}\left(P, T, C_{CH_4}, C_{CO_2}, C_{H_2S}\right) \tag{3.20}$$

Solution of the compressible pipe flow problem requires equations for pressure, density, and velocity at each node. At this point, all relevant properties are known at the channel inlet (the first node). Properties from the second gas node to the second to last gas node are evaluated using centrally-averaging forms of the conservation equations.

The first equation evaluated at each node is the conservation of momentum, which is used to determine pressure at the node of interest. The momentum balance for a control volume is shown in its differential form in Equation (3.21). Equation (3.22) shows the discretized form of (3.21) used in the model. This momentum balance states that the total pressure drop across a control volume, the term on the left side, is equal to the sum of the pressure losses due to temporal acceleration, convective acceleration across the control volume length (also called spatial acceleration), and the frictional pressure drop due to fluid shear against the channel walls.

$$-\frac{\partial P}{\partial x} = \frac{\partial(\rho v)}{\partial t} + v\frac{\partial(\rho v)}{\partial x} + f\frac{\rho v^2}{2D_h} \tag{3.21}$$

$$-\left(\frac{P_i^t - P_{i-1}^t}{\Delta x}\right) = \frac{\rho_i^t v_i^t - \rho_i^{t-1} v_i^{t-1}}{\Delta t} + \frac{\rho_{i+1}^t v_{i+1}^t - \rho_{i-1}^t v_{i-1}^t}{2\Delta x} + f_i^{\,t}\frac{\rho_i^t \left(v_i^t\right)^2}{2D_h} \tag{3.22}$$

The friction factor in Equation (3.22) is evaluated using the Churchill (1977) friction factor correlation along with a correction factor for the square channel geometry. Reynolds number is evaluated using the current values of density and velocity, as shown in Equation (3.23).

$$Re_i^t = \frac{\rho_i^t v_i^t D_h}{\mu_i} \tag{3.23}$$

Next, density is calculated from pressure, concentration, and temperature. This calculation is performed using the Peng-Robinson equation of state, which properly accounts for non-ideal gas behavior due to the high system pressure (5500 kPa). For greater accuracy and computational efficiency the equation of state is evaluated using the Multiflash property package in gPROMS (Process Systems Enterprise, 1997-2009). The continuity equation is then used to calculate the velocity at the node of interest. The differential form of the continuity equation is shown in Equation (3.24), while the discretized form used in the model is Equation (3.25). For the present case, it is assumed that there is no mass flux through the walls ($\dot{m} = 0\ kg\ s^{-1}$), but in full process simulations, the flux term is determined by calculations for diffusion mass transfer into the channel walls. The continuity equation states that the accumulation of mass in the channel, shown as the time derivative of density, is equal to the inflow and outflow of mass from the control volume. The inflow and outflow due to advection is expressed by the spatial derivative of the mass flux, and the mass flow from the channel walls is expressed by the far right term.

$$\frac{\partial \rho}{\partial t} = -\frac{\partial (\rho v)}{\partial x} + \frac{\dot{m}_{in}}{V_{CV}} \tag{3.24}$$

$$\frac{\rho_i^t - \rho_i^{t-1}}{\Delta t} = -\frac{\rho_i^t v_i^t - \rho_{i-1}^t v_{i-1}^t}{\Delta x} + \frac{\dot{m}_i^t}{A_C \cdot \Delta x} \tag{3.25}$$

Next, the species conservation equation is used to calculate the volumetric concentrations of CH_4, CO_2, and H_2S in each volume. The equation calculates the current concentration of species A based on the inflow and outflow of A in the channel and the addition or removal of A by mass transport through the walls (denoted by $\dot{m}_A$). The differential and discretized equation forms are shown in Equations (3.26) and (3.27). This equation is solved for all three species. Just as in the continuity equation, the mass flux of species A through the wall is assumed to be zero, but in future work, this term can be determined using diffusion mass transfer calculations.

$$\frac{\partial\left(\rho X_A\right)}{\partial t}=-\frac{\partial\left(\rho X_A v\right)}{\partial x}+\frac{\dot{m}_A}{V_{CV}} \tag{3.26}$$

$$\frac{\rho_i^t X_{A,i}^t-\rho_i^{t-1} X_{A,i}^{t-1}}{\Delta t}=\frac{v_{i-1}^{t-1}\rho_{i-1}^{t-1} X_{A,i-1}^{t-1}-v_{i+1}^{t-1}\rho_{i+1}^{t-1} X_{A,i+1}^{t-1}}{\Delta x}+\frac{\dot{m}_{A,i}^t}{A_C\cdot\Delta x} \tag{3.27}$$

The updated molar concentrations are calculated from the mass fractions using Equation (3.28), which is derived from the relations of mass fraction and mole fractions for each species. Knowing the molar concentrations allows for the evaluation of the molar mass, density, and viscosity of the gas. The mixture density and viscosity are calculated from pressure, temperature, and concentration using the Multiflash property package in gPROMS.

$$C_{A,i}^t=\frac{X_{A,i}^t M_C+\dfrac{X_{A,i}^t X_{B,i}^t M_C\left(M_B-M_C\right)}{M_B-X_{B,i}^t\left(M_B-M_C\right)}}{M_A-X_{A,i}^t\left(M_A-M_C\right)-\dfrac{X_{A,i}^t X_{B,i}^t\left(M_A-M_C\right)\left(M_B-M_C\right)}{M_B-X_{B,i}^t\left(M_B-M_C\right)}} \tag{3.28}$$

Equations (3.21) through (3.28), along with the Multiflash property evaluations, are applied to each node except for the last gas node, which is located adjacent to the liquid-gas interface. To ensure that fluid property and concentration data are not communicated across the liquid-gas interface the backward differencing forms of the previous equations are used for the final gas node.

The only nodal values left to compute are those for the liquid region. Only a single node is needed to accurately calculate pressure drop and velocity because the liquid region is assumed to be incompressible. As a result of this incompressible assumption, and the constant cross-sectional area of the channel, the fluid velocity at all axial locations in the liquid region must be equal to the velocity of the liquid-gas interface. This interface velocity is equal to the fluid velocity in the adjacent gas node.

Liquid density for the liquid region is calculated using Multiflash. Because the liquid density is constant, the outlet pressure can be found based on the momentum equation. The momentum equation for the liquid is shown in Equation (3.29). For an incompressible fluid the convective acceleration term is necessarily equal to zero, and is therefore not included.

$$-\left(\frac{P_i^t - P_{i-1}^t}{\Delta x}\right) = \frac{\rho_i^t v_i^t - \rho_i^{t-1} v_i^{t-1}}{\Delta t} + f_i^t \frac{\rho_i^t \left(v_i^t\right)^2}{2D_h} \tag{3.29}$$

Once a solution that satisfies the pressure conditions has been obtained, the location of the liquid-gas interface is reevaluated using the liquid velocity calculated using Equation (3.30). These values are saved and node lengths are recalculated to fit the gas region. Iterative calculations are then performed again for the next time step.

$$\frac{\partial L_G}{\partial t} = v_L \tag{3.30}$$

Several initial conditions are needed to close the system of equations for the first time step. The fluid is considered to be at rest to start the calculation, and the velocity at each node is set to zero. The initial pressure is set to the outlet pressure at all points, to be consistent with the zero velocity condition. The concentrations at each gas node are set to the inlet concentrations, equal to the feed gas mixture concentrations listed in Table. Finally, because the number of nodes in the gas region remains constant throughout the calculation, the gas region length must be initialized. Therefore, at the beginning of this process, the gas is assumed to occupy 1 mm of the 1 meter long channel, to approximate a liquid filled channel.

To ensure a physically realistic initial state, and one that would ensure computational stability, rather than instantaneously changing the inlet pressure to start flow an explicit exponential function of time was used to quickly transition from the low starting pressure to the known driving inlet pressure of 5500 kPa. This expression, shown in Equation (3.31), is also physically analogous to the actuation of a fast-operating valve;

the pressure change is 90% complete by 0.12 seconds and 99% complete by 0.23 seconds. This actuation time is consistent with those for commercially available high pressure solenoid valves (Engineering, 2012). The inlet pressure calculated by equation (3.31) is shown in Figure 3.12.

$$P_{in} = P_{in} - \left(P_{in} - P_{out}\right) e^{-20t} \tag{3.31}$$

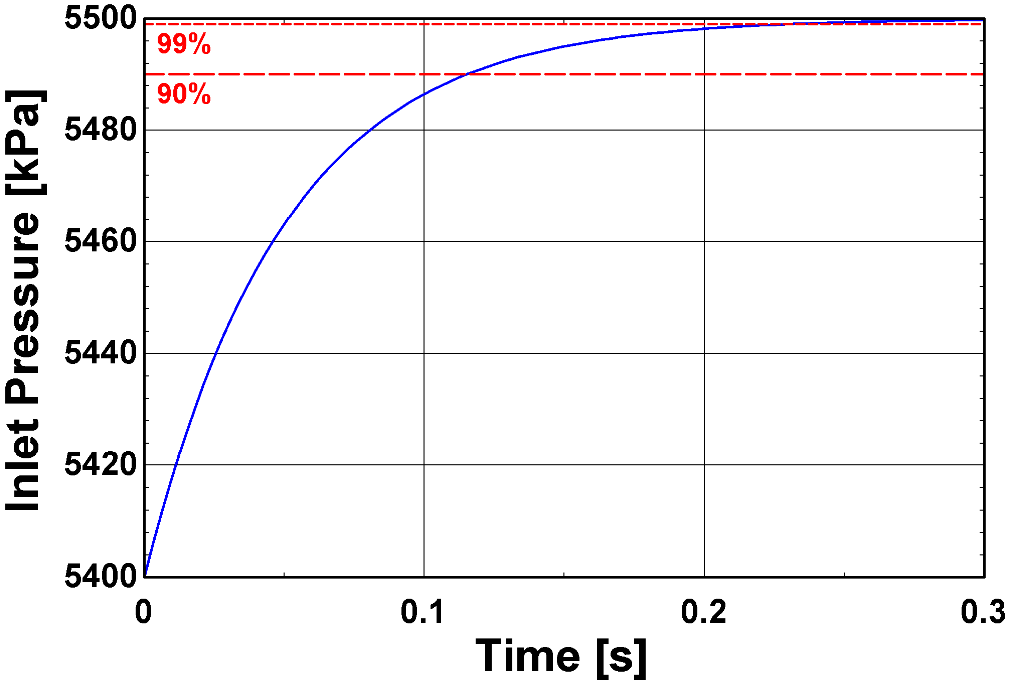

Figure 3.12: Inlet pressure vs. time for the valve equation given in Equation (3.31).

The results from the calculations described above are shown in Fig. 3.13. Once again, the pressure drop in the liquid phase is found to be dominant. The displacement of all liquid from the channel takes 3.26 seconds, and the maximum calculated velocity was found to be 3.15 m s^{-1}. In contrast, the incompressible model used previously for approximate velocity estimations predicted displacement times of approximately 2.25 seconds, with a maximum velocity of 3.75 m s^{-1}. This difference between the compressible and incompressible results is explained based on several factors: the presence of pressure drops due to convective acceleration, the use of more accurate non-ideal property evaluations, and the use of a non-instantaneous driving pressure increase.

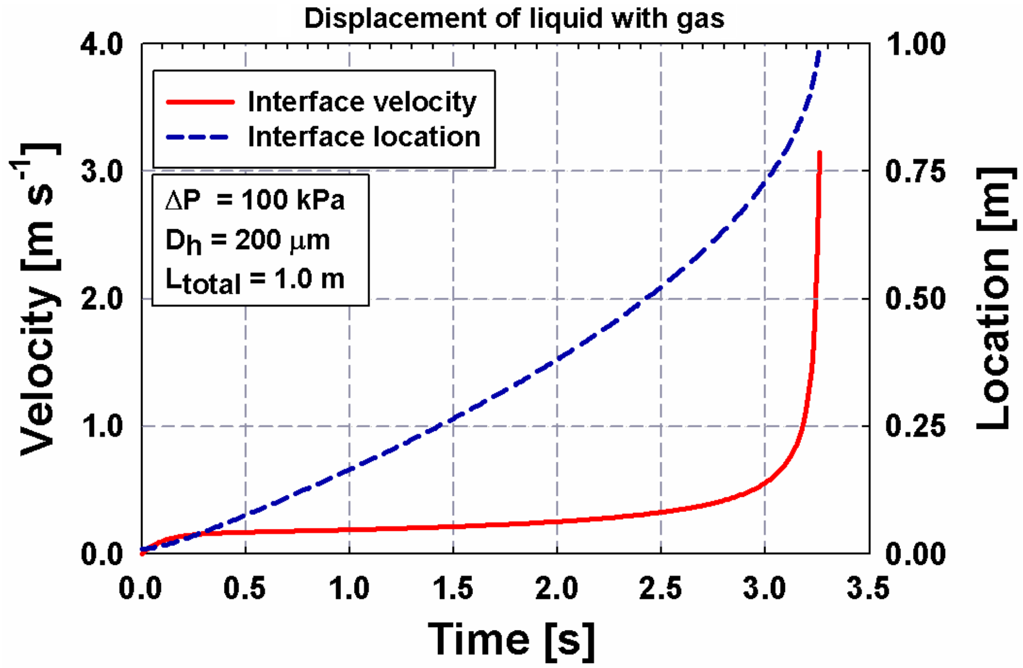

Figure 3.13: Interface velocity and location vs time during the displacement of liquid by gas.

Fig. 3.14 shows the total pressure gradient in the channel as a function of axial location, as well as the contributions of the frictional, convective acceleration, and temporal acceleration pressure losses to the total pressure gradient. The step change in channel pressure gradient indicates the location of the liquid-gas interface, as the fluid properties change abruptly at that point. Once again, it is demonstrated that the pressure drop in the liquid region dominates the total pressure drop in the channel, as can be seen from the fact that the total pressure gradient to the right of the liquid-gas interface is significantly higher than the pressure gradient to the left. For both phases, the total pressure losses are dominated by the frictional losses. Temporal acceleration losses (pressure loss due to the acceleration of the fluid mass) are found to be of the same order of magnitude as friction losses at early time steps, in which the comparatively large liquid mass is moved from rest. Finally, the pressure losses due to convective acceleration (pressure loss due to spatial variation in fluid velocity) are found to be relatively insignificant in the gas phase, and are three orders of magnitude less than those of frictional pressure losses. In the liquid region the convective acceleration is necessarily zero, as the fluid is incompressible.

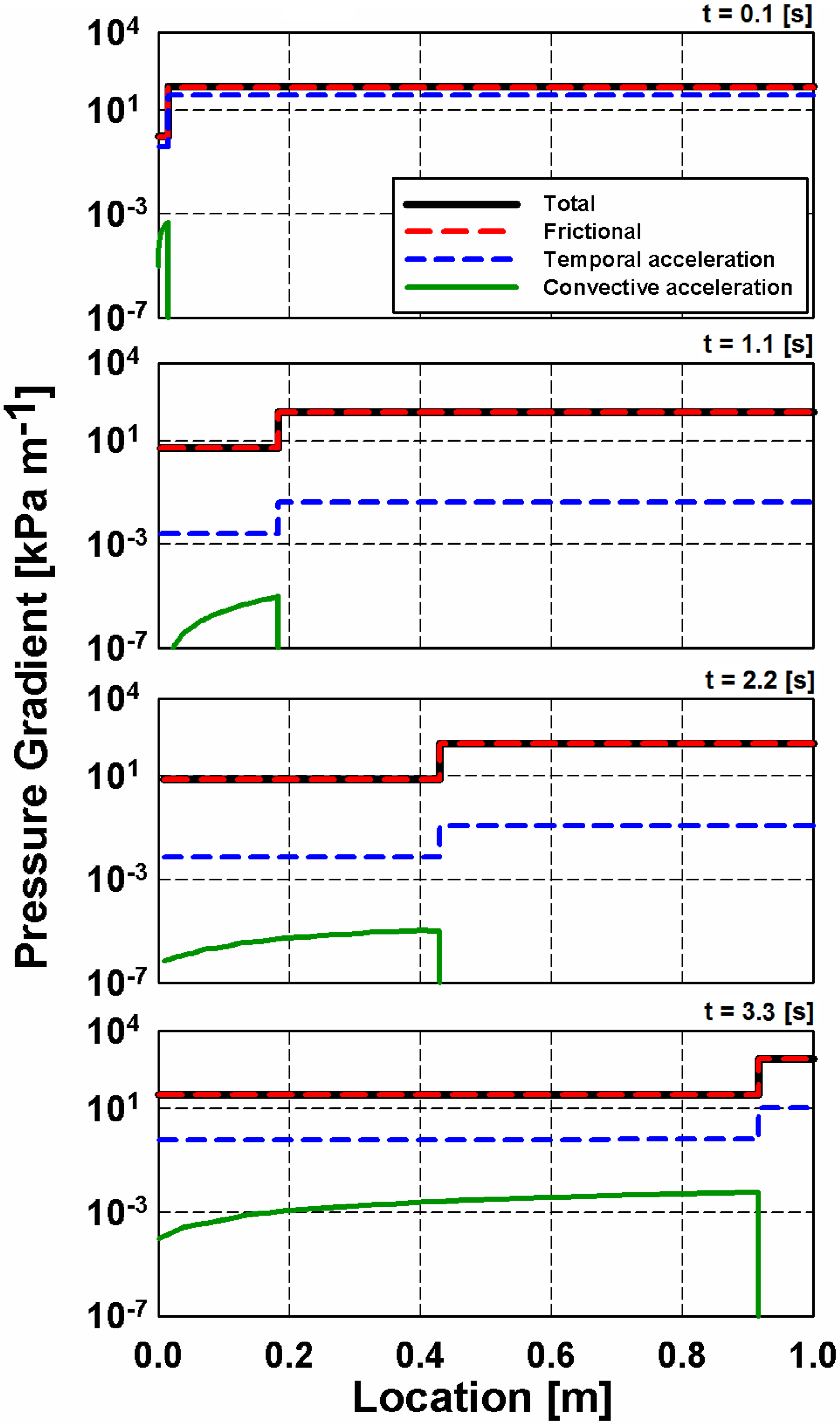

Figure 3.14: Total, frictional, temporal, and convective pressure drops (per unit length) in the channel at 0.1, 1.1, 2.2, and 3.3 sec during the displacement of liquid by gas.

The computational approach for the compressible displacement model described above was modified to model the displacement of gas by liquid. All of the equations and initial conditions described previously were the same, except that the channel was considered to be filled with stationary gas at the initial state. In this case, the single liquid node occupies a 1 mm long region at the channel inlet at the initial state, and the 50 gas nodes occupy 999 mm. Once again, at the initial state, the velocities are set to zero and the pressures everywhere in the channel are equal. The inlet pressure is increased according to the same explicit function of time used in the previous case, shown in Equation (3.31). The results of this calculation are shown in Fig. 3.15.

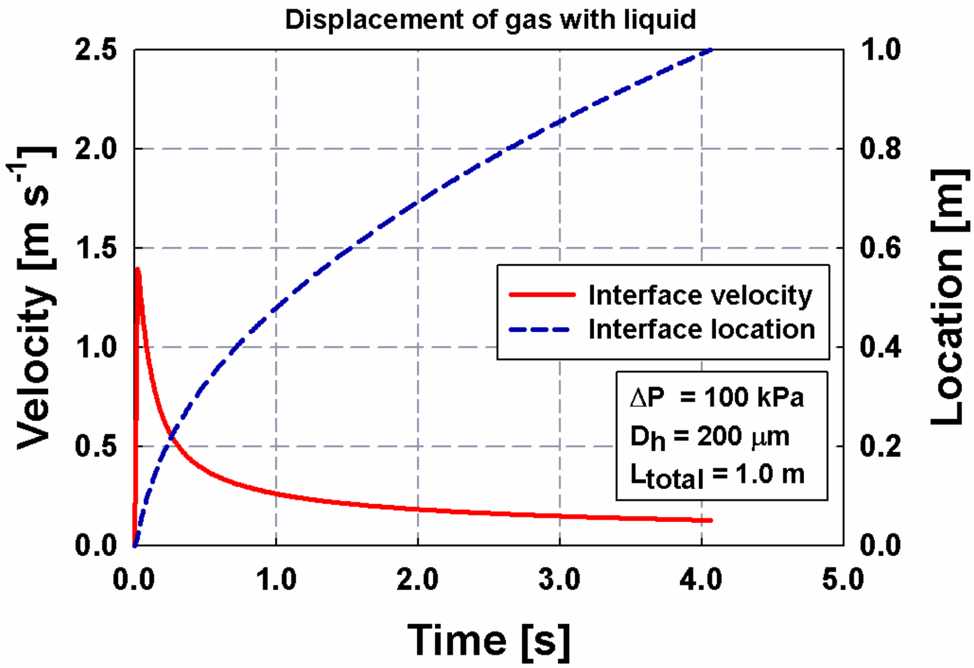

Figure 3.15: Interface velocity and location vs time during the displacement of gas with liquid.

The results show a fast initial increase in velocity as the channel inlet pressure is increased to the inlet pressure. The interface velocity reaches a maximum at 0.02 seconds, with a velocity of 1.39 m s^{-1}. After this, the entrance of more liquid into the channel causes the flow to rapidly slow down as the pressure drop in the liquid region becomes greater. By the time all the gas is displaced from the channel the interface velocity is 0.126 m s^{-1}. Displacement of gas from the channel takes 4.06 seconds.

The pressure gradients due to friction, temporal acceleration, and convective acceleration during the displacement of gas by liquid are shown in Figure 3.16. As in the case of the displacement of liquid by gas, viscous pressure losses in the liquid phase constitute the major portion of the total pressure drop, and convective acceleration losses in the gas phase are found to be negligible. Temporal acceleration losses in this case are found to have little influence on the total pressure drop, even in early time steps. This is due to the fact that the major portion of the channel is filled with gas at this point, leading to the amount of fluid mass contained in the channel being relatively small. Consequently, rapid changes in fluid velocity in the early time steps do not significantly contribute to the total loss of momentum. It should also be noted that because the fluid velocity decreases as more liquid enters the channel, the temporal acceleration pressure losses for most of the displacement process are negative.

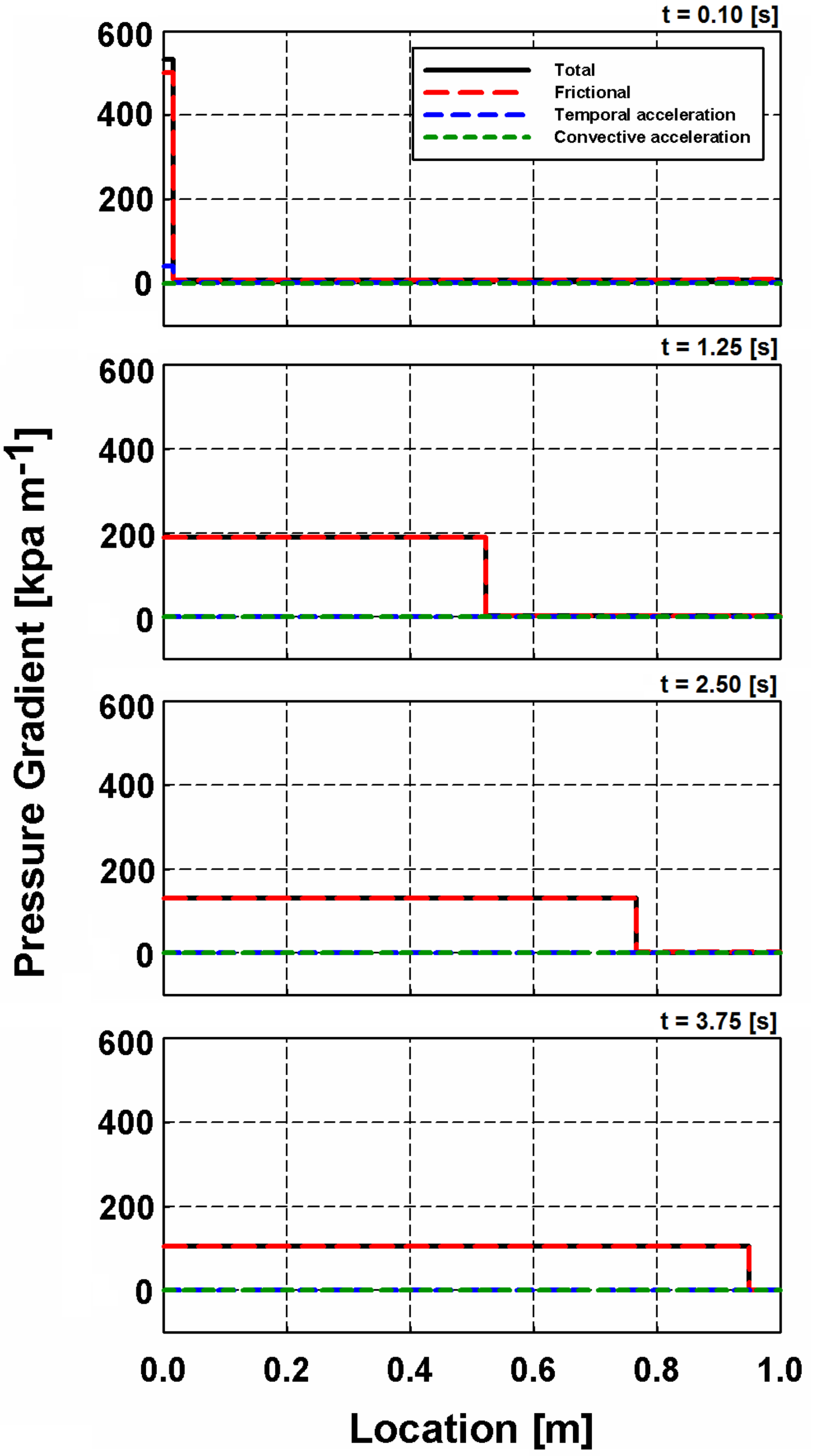

Figure 3.16: Total, frictional, temporal, and convective pressure drops (per unit length) in the channel at 0.10, 1.25, 2.50, and 3.75 sec during the displacement of gas by liquid.

As discussed previously, the dynamically meshed compressible model and the incompressible two-node model produce different predictions of fluid velocities and displacement times. Several factors contributed to these differences, including the incorporation of convective and temporal acceleration losses in the conservation of momentum, the use of a non-instantaneous driving pressure increase to simulate valve actuation, and the use of realistic non-ideal gas property evaluations. The results calculated by the compressible flow model are likely to be much more accurate, both because temporal acceleration losses were shown to be significant at early time steps and because at operating pressures as high as 5500 kPa, gases can be expected to exhibit significant non-ideal characteristics. While the dynamic discretization scheme used provides smooth, accurate interface tracking, the constantly changing mesh will create difficulties in coupling this model to other computational domains, such as the adsorbent wall.

3.4 Heat and mass transfer modeling

The final model to be discussed in this work is a coupled heat and mass transfer model for the prediction of mass transfer behavior and assessment of the impact of residual liquid films on adsorption system performance. The model uses an implicit finite volume approach and stationary meshes in the channel and adsorbent walls. Flow in the channel is coupled to calculations for heat transfer, adsorption, and diffusion mass transfer in the channel walls.

While a dynamic meshing scheme was used to model the two-phase displacement in the fluid channel, it is unlikely that a similar dynamic mesh scheme would be able to accurately model the heat and mass transfer behavior in the adsorbent wall without the use of extensive and complicated spatial interpolation calculations. The fluid channel mesh can be updated frequently with relative ease because the calculation depends solely on advection, whereby heat and mass are transferred axially only due to the bulk motion of the fluid in the channel. Conversely, heat and mass transfer in the wall occurs due to diffusion, and, as demonstrated in the order of magnitude analysis, spatial gradients of temperature and concentration are expected to be significant in the wall. Moreover, the storage of adsorbed mass is highly spatially dependent. Unlike the channel domain, in which all of the mass is moving, the wall domain involves the accumulation of mass and energy at stationary points.

As discussed previously, the coupling of a moving channel mesh to the stationary wall mesh would pose numerous difficulties in accounting for the exchange of heat and mass between the different domains. The development of a full-scale process model accounting for adsorption, desorption, and both fluid displacement processes is beyond the scope of this thesis. The heat and mass transfer models developed here are intended to assess the effect of the residual liquid films left behind after displacement on channel mass transfer performance during the adsorption phase of the process. For this purpose, it is sufficient to model the fluid domain as a gas-filled channel initially filled with pure methane. This enables the use of a static mesh in the fluid channel as well as the adsorbent wall, simplifying the calculation significantly. This gas-filled channel condition is consistent with the use of a purge step using pure methane gas, a common practice in adsorption systems, as discussed in Chapter 2 (Olajossy *et al.*, 2003).

The model is divided into two computational domains: the fluid channel and the adsorbent wall. These domains can be found in the diagram in Figure 3.17. The two computational domains are coupled through the use of source terms in the conservation equations at the domain boundaries. Calculations in the fluid channel domain are one-dimensional in the axial direction and account for fluid flow, heat transfer, and species exchange with the adsorbent wall through the solution of the mass, momentum, species, and energy conservation equations, as well as gas mixture property evaluations computed in Multiflash (Process Systems Enterprise, 1997-2009).

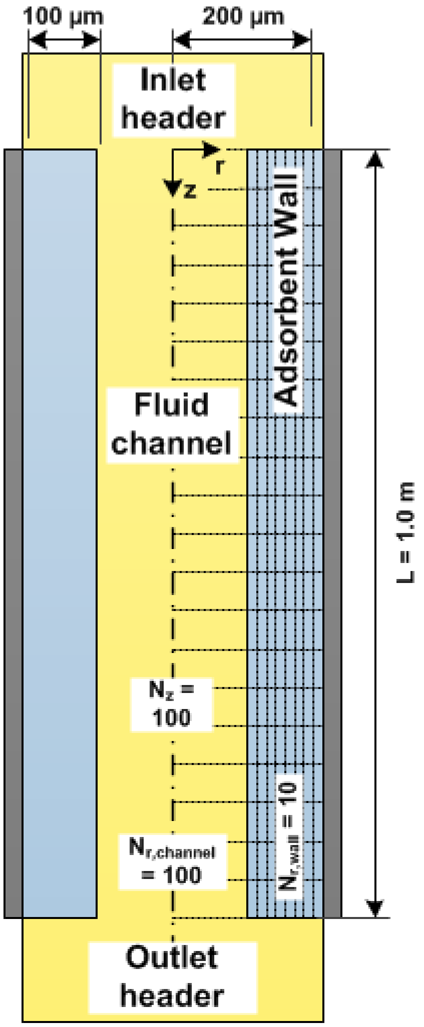

Figure 3.17: Mesh diagram for heat and mass transfer model.

Calculations in the two-dimensional adsorbent wall domain are discretized axially and radially. The species conservation equation for the wall region includes diffusion mass transfer and adsorption terms, and the energy equation includes the generation of heat due to adsorption. Both domains utilize a two-component model, accounting for concentrations of CH_4 and CO_2 at each location, while CH_4 is assumed to be non-adsorbing.

Solution in the fluid channel domain is similar to the gas phase portion of the displacement model described previously; however, because only one phase is present, it is not necessary to re-discretize the domain at each time step. The species, momentum, and energy conservation equations for the fluid channel are given by Equations (3.32) through (3.34). In these equations, the subscript g denotes values for the fluid channel, while the subscript w indicates values for the adsorbent wall. The subscript i denotes individual species. Figure 3.18 shows a sample control volume schematic for a gas channel node.

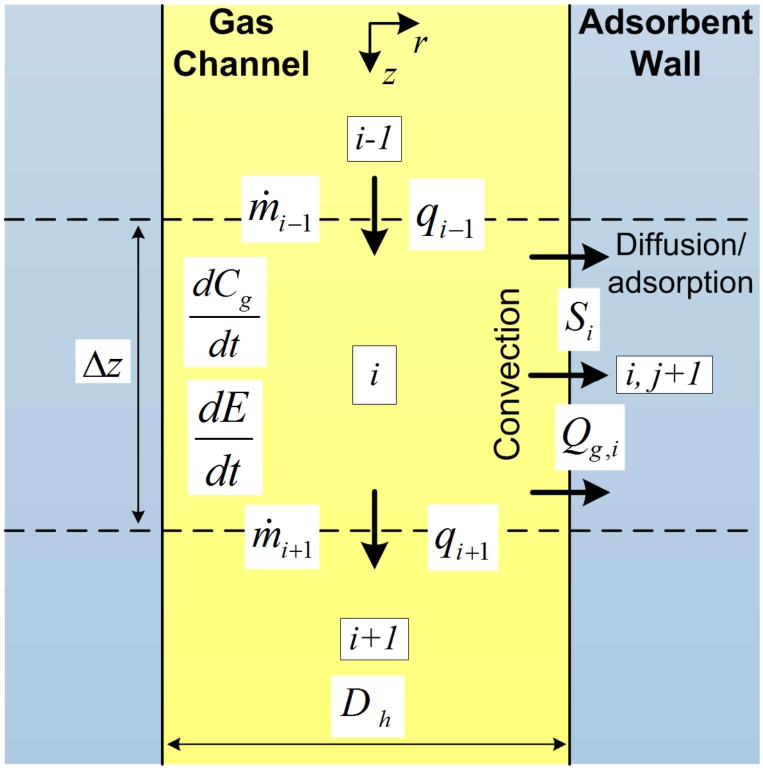

Figure 3.18: Control volume schematic for a node in the gas channel.

$$\frac{\partial c_{g,i}}{\partial t} + u\frac{\partial c_{g,i}}{\partial z} = -\dot{S}_i''' \tag{3.32}$$

$$\rho u\frac{\partial u}{\partial z} - \sum \dot{S}_i''' u = -\frac{\partial P}{\partial z} + \frac{4}{3}\mu\frac{\partial^2 u}{\partial z^2} - f\frac{\rho u^2}{2D_h} \tag{3.33}$$

$$\rho_g c_{p,g}\frac{\partial T_g}{\partial t} + \rho_g c_{p,g} u\frac{\partial T_g}{\partial z} = -\dot{Q}_g''' \tag{3.34}$$

In these equations the terms $\dot{S}_i'''$ and $\dot{Q}_g'''$ are the species removal rate and heat exchange rate, which, respectively, account for the removal of mass and heat from the fluid channel to the adsorbent wall via convection. These key coupling terms link the calculations for the fluid channel to those in the adsorbent wall, and are given in Equations (3.35) and (3.36) below. Convection heat and mass transfer coefficients are calculated using the correlations from Churchill (1977) for Nusselt number with the heat and mass transfer analogy used to obtain the Sherwood number. These correlations can be found in Appendix A.

$$\dot{S}''' = h_{m,conv} \frac{Per}{A_{CS}} \left(c_{g,i} - c_{w,i} \right) \tag{3.35}$$

$$Q_g''' = h_{T,conv} \frac{Per}{A_{cs}} \left(T_g - T_w \right) \tag{3.36}$$

As in the displacement models, the density of the gas mixture is determined using the Peng-Robinson equation of state (as computed by Multiflash). Mixture viscosity is also calculated in Multiflash using the Pedersen correlation, also found in Equation (3.2) (Pedersen and Fredenslund, 1984).

Computations in the adsorbent wall account for both axial and radial variations in concentration, density, and temperature. The species and energy conservation equations used in the wall region are shown in Equations (3.37) and (3.38) below. In these equations, ω is the volume fraction of the wall region occupied by the adsorbent material, and ε is the ratio of void space to wall volume in a unit cell of adsorbent wall material (this includes the space occupied by the non-adsorbent binding polymer). The subscript m denotes the properties of the adsorbent wall material. The term $\sum \dot{Q}_{ads,i}'''$ accounts for the latent heat of adsorption for each mixture component, which couples the energy and mass conservation calculations in the wall. Equation (3.39) shows the heat generation due to adsorption. Figure 3.19 shows a sample control volume schematic for a node in the interior of the adsorbent wall.

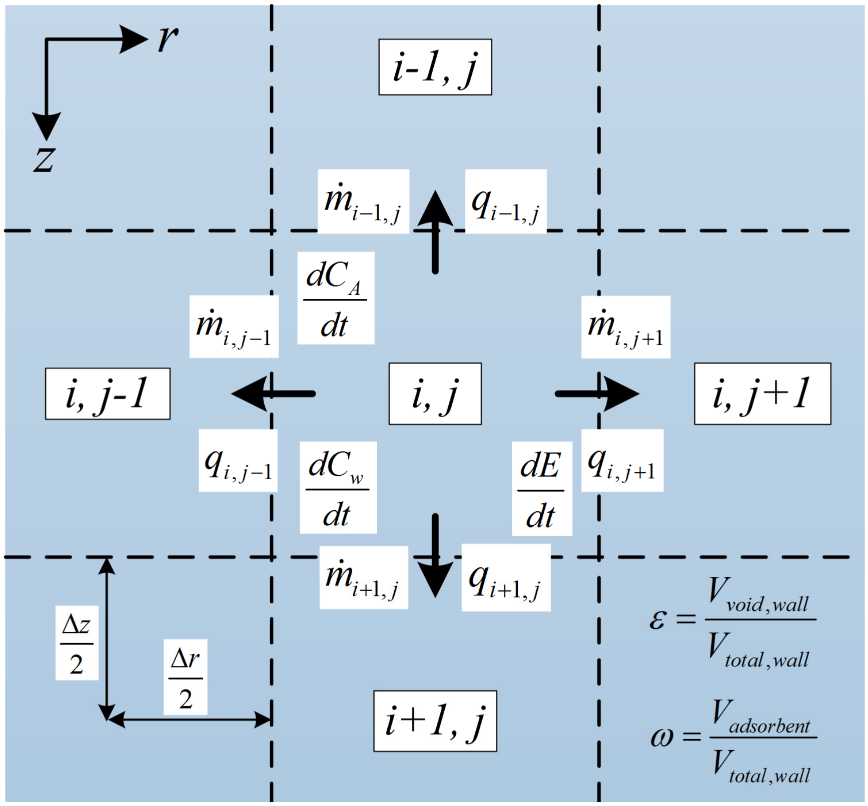

Figure 3.19: Sample control volume for an interior node in the adsorbent wall.

$$\frac{\partial c_{w,i}}{\partial t} + \frac{\omega}{\varepsilon}\frac{\partial c_{A,i}}{\partial t} = D\nabla c_{w,i} \tag{3.37}$$

$$\rho_m C_{p,m}\frac{\partial T}{\partial t} = k_m \nabla^2 T + \sum \dot{Q}_{ads,i}''' \tag{3.38}$$

$$Q_{ads,i}''' = \omega \cdot h_{ads,i}\frac{\partial c_{A,i}}{\partial t} \tag{3.39}$$

In these equations, $C_{A,i}$ is the adsorbed species concentration, as determined by the multisite Langmuir adsorption equations (Mathias *et al.*, 1996). The mass diffusion coefficient D_{eff} is determined by the correlation from Hirschfelder et al (1949). Values for polymer void fraction (ε) and tortuosity (τ) are assumed to be 0.55 and 2.0, respectively. The average molecular diameter (σ) and collision integral (Ω) are determined from tabulated values to be 3.782 and 1.31, respectively (Hines and Maddox, 1985).

$$D_{eff} = \frac{\varepsilon}{\tau}(D) = \frac{\varepsilon}{\tau}\frac{1.858\times10^{-27}}{P\sigma^2\Omega}\left(\frac{1}{M_{CO_2}} + \frac{1}{M_{CH_4}}\right)^{0.5} \tag{3.40}$$

Heat and mass transfer boundary conditions are applied to each boundary of the adsorbent wall region. At the adsorbent layer surface, which is in contact with the gas in the fluid channel, the heat and mass convection conditions described by Equations (3.35) and (3.36) are linked to the heat and mass diffusion rates into the wall. These boundary conditions are shown in Equations (3.41) and (3.42), and in Figure 3.20.

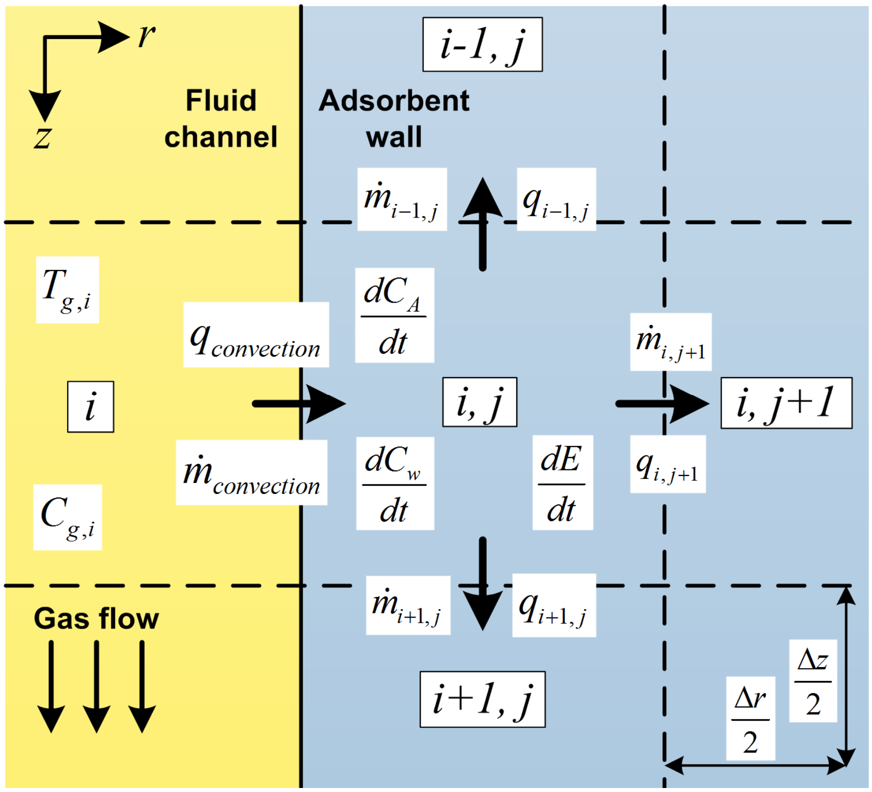

Figure 3.20: Diagram of an adsorbent wall control volume adjacent to the gas channel.

$$k_m \left.\frac{\partial T}{\partial r}\right|_{r=r_{inner}} = h_{T,conv}\left(T_g - T_w\big|_{r=r_{inner}}\right) \tag{3.41}$$

$$D \frac{\partial c_w}{\partial r}\bigg|_{r=r_{inner}} = h_{m,conv}\left(c_g - c_w\big|_{r=r_{inner}}\right) \tag{3.42}$$

At the outer radial limit of the channel, where the adsorbent material layer meets the monolith wall, the boundary is considered to have zero heat and mass flux. The boundary conditions are given by Equations (3.43) and (3.44), and a diagram is provided in Figure 3.21.

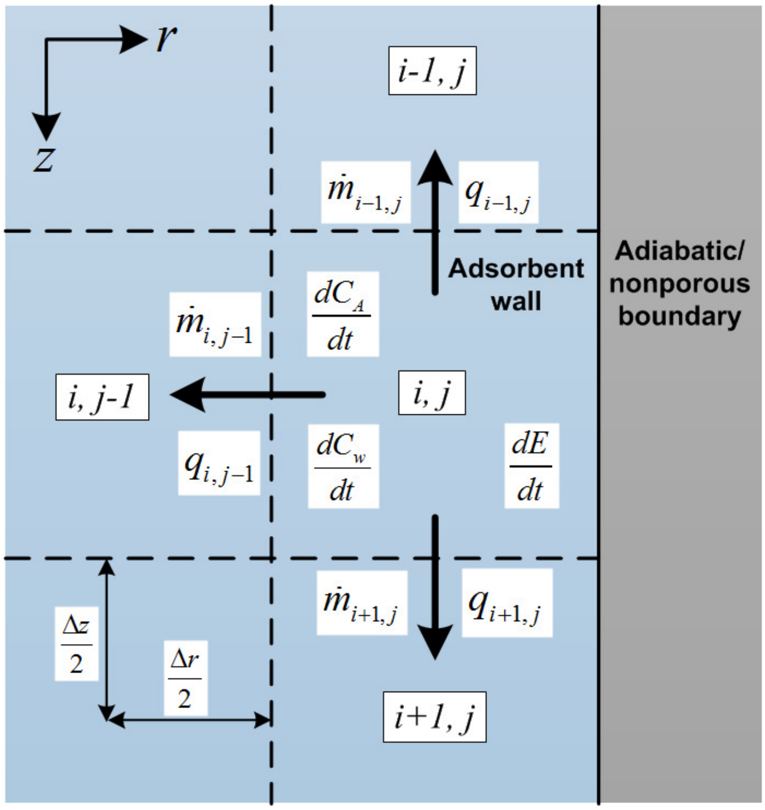

Figure 3.21: Diagram of an adsorbent wall control volume at the radial limit of the domain.

$$k_m \frac{\partial T}{\partial r}\bigg|_{r=r_{outer}} = 0 \tag{3.43}$$

$$D \frac{\partial c_w}{\partial r}\bigg|_{r=r_{outer}} = 0 \tag{3.44}$$

At the channel inlet, the adsorbent layer is exposed to the feed gas mixture occupying the fluid header, which provides flow to the channel. Because the fluid in the header is considered to be stationary, the convection coefficients used are for natural convection on an upward-facing surface. These convection correlations used were those of McAdams (1954) and Goldstein (1973), and values of heat transfer and mass transfer convection coefficients were found to be 33.9 W m^{-2} K^{-1} and 8.2×10^{-5} m s^{-1}, respectively. These correlations and their parameters are listed in Appendix A. The heat and mass transfer boundary conditions for the adsorbent layer at the inlet are given by equations (3.45) and (3.46). A diagram of this inlet header boundary condition is shown in Figure 3.22.

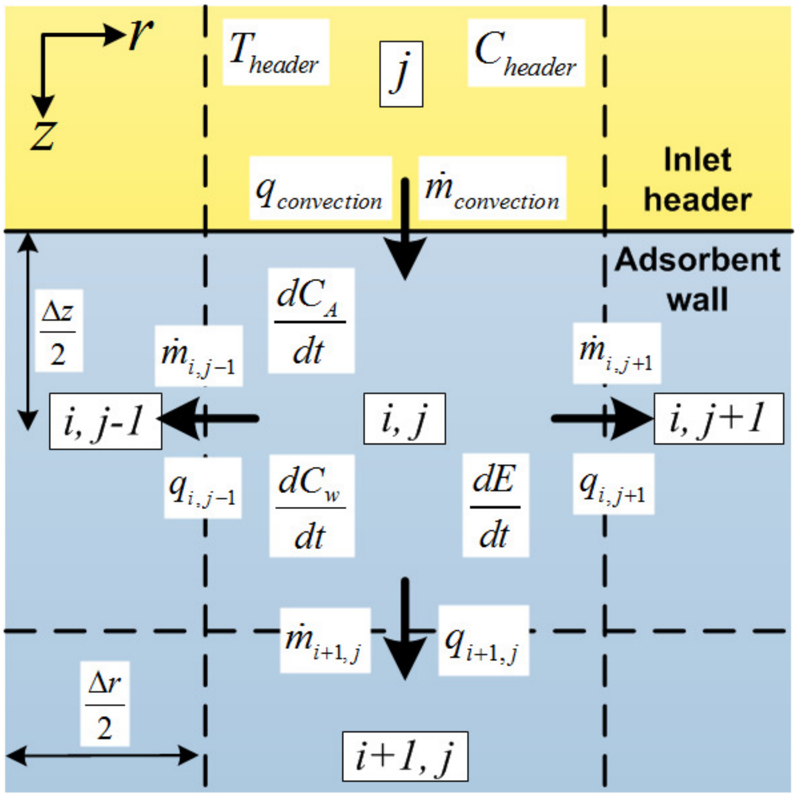

Figure 3.22: Diagram of an adsorbent wall control volume adjacent to the fluid inlet header.

$$k_m \left.\frac{\partial T}{\partial z}\right|_{z=0} = h_{T,nat,in}\left(T_{feed} - T_w\big|_{z=0}\right) \tag{3.45}$$

$$D \left.\frac{\partial c_w}{\partial r}\right|_{z=0} = h_{m,nat,in}\left(c_{feed} - c_w\big|_{z=0}\right) \tag{3.46}$$

Similar to the previously described condition, at the channel outlet, the adsorbent layer is in contact with the outlet header, which is filled with the effluent gas. Heat and mass transfer coefficients for natural convection on a downward-facing flat plate were used. The heat transfer coefficient was determined to be 18.2 W m^{-2} K^{-1} and the mass transfer coefficient was determined to be 4.34×10^{-5} m s^{-1}. The boundary conditions for the channel outlet are given by Equations (3.47) and (3.48), and a diagram of the outlet header boundary condition is shown in Figure 3.23.

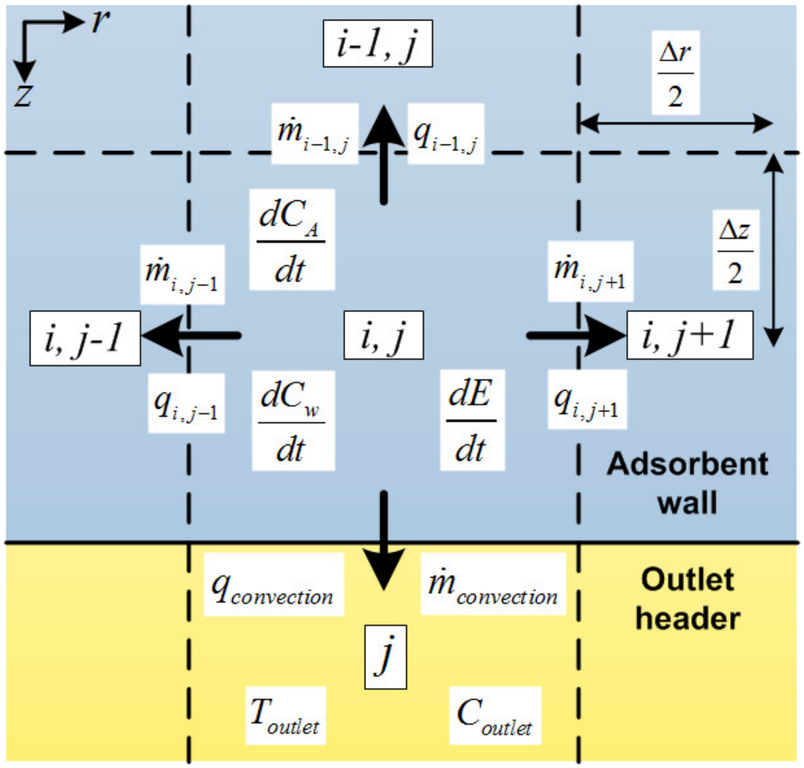

Figure 3.23: Diagram of an adsorbent wall control volume adjacent to the fluid outlet header.

$$k_m \left.\frac{\partial T}{\partial z}\right|_{z=L} = h_{T,nat,out}\left(T_{feed} - T_w\big|_{z=L}\right) \tag{3.47}$$

$$D \left.\frac{\partial c_w}{\partial r}\right|_{z=L} = h_{m,nat,out}\left(c_{feed} - c_w\big|_{z=L}\right) \tag{3.48}$$

The boundary and initial conditions at the fluid channel inlet and outlet are the same as those used in the displacement models, namely fixed outlet pressure and an explicit function of time to simulate the rapid pressurization of the channel inlet. This equation was given by (3.31). The temperature of the feed gas is taken to be 25°C, while the inlet concentrations are taken to be 70% CH_4 and 30% CO_2 on a molar basis.

As in the displacement models, the gas in the channel begins at rest with zero velocity and equal pressure at all points. In this case, the channel is assumed to be filled with pure methane at the initial state. This is analogous to the start of feed gas flow after a methane purge. It was assumed that the water used for desorption is at 200 °C, with the corresponding initial adsorbed concentration of CO_2 at 4937 mol m^{-3}, the equilibrium adsorbed concentration at that temperature and the pressure and gas concentrations at the inlet. Properties in the adsorbent wall region are calculated based on properties for 5X Zeolite and PDMS polymer (Li *et al.*, 2009). The simulation parameters and properties used in the model are listed in Table 3.6, and the same adaptive time stepping technique discussed previously was used for solution (Process Systems Enterprise, 1997-2009).

Table 3.6: Simulation parameters and material properties used for heat and mass transfer modeling

Parameter	Value	Units	Description
ε	0.55	-	Adsorbent layer void fraction
MF_{ads}	0.5	-	Adsorbent mass fraction in wall
ρ_{ads}	1600	kg m^{-3}	Adsorbent particle density
k_{ads}	4	W $m^{-1}K^{-1}$	Adsorbent thermal conductivity
$c_{p,ads}$	800	J $kg^{-1}K^{-1}$	Adsorbent specific heat
ρ_{poly}	1420	kg m^{-3}	Binding polymer density
k_{poly}	80	W $m^{-1}K^{-1}$	Binding polymer thermal conductivity
$c_{p,poly}$	1200	J $kg^{-1}K^{-1}$	Binding polymer specific heat
e	1×10^{-6}	M	Channel roughness
L	1	m	Channel length
P_{in}	5500	kPa	Inlet pressure
P_{out}	5400	kPa	Outlet pressure
t_{ads}	1×10^{-4}	m	Adsorbent layer thickness
$X_{CH4,in}$	0.7	-	Mole fraction of methane
$X_{CO2,in}$	0.3	-	Mole fraction of CO_2
D_h	2×10^{-4}	m	Channel hydraulic diameter
N_z	100	-	Number of axial discretization points
$N_{r,wall}$	10	-	Number of radial discretization points (wall)
$N_{r,channel}$	1	-	Number of radial discretization points (channel)

The model was executed using the conditions described above. Fig. 3.24 shows contour plots of the resulting adsorbed CO_2 concentration in the wall, and Figure 3.25 shows the corresponding CH_4 concentrations in the fluid channel. As is evident from Figure 3.24, a concentration front, a localized region of concentration increase, is formed in the adsorbent region as the CO_2 diffuses into the walls and adsorbs onto the zeolite particle surfaces. The slant in the concentration front is indicative of the fact that the CO_2 must diffuse farther into the wall to reach the outer region of the adsorbent layer. This gradient causes a portion of the adsorbent to go effectively unused by the time the concentration front reaches the channel outlet at approximately 1.5 seconds. At this point in time, the adsorbent is no longer able to sufficiently purify the gas in the channel and the methane purity at the channel outlet decreases.

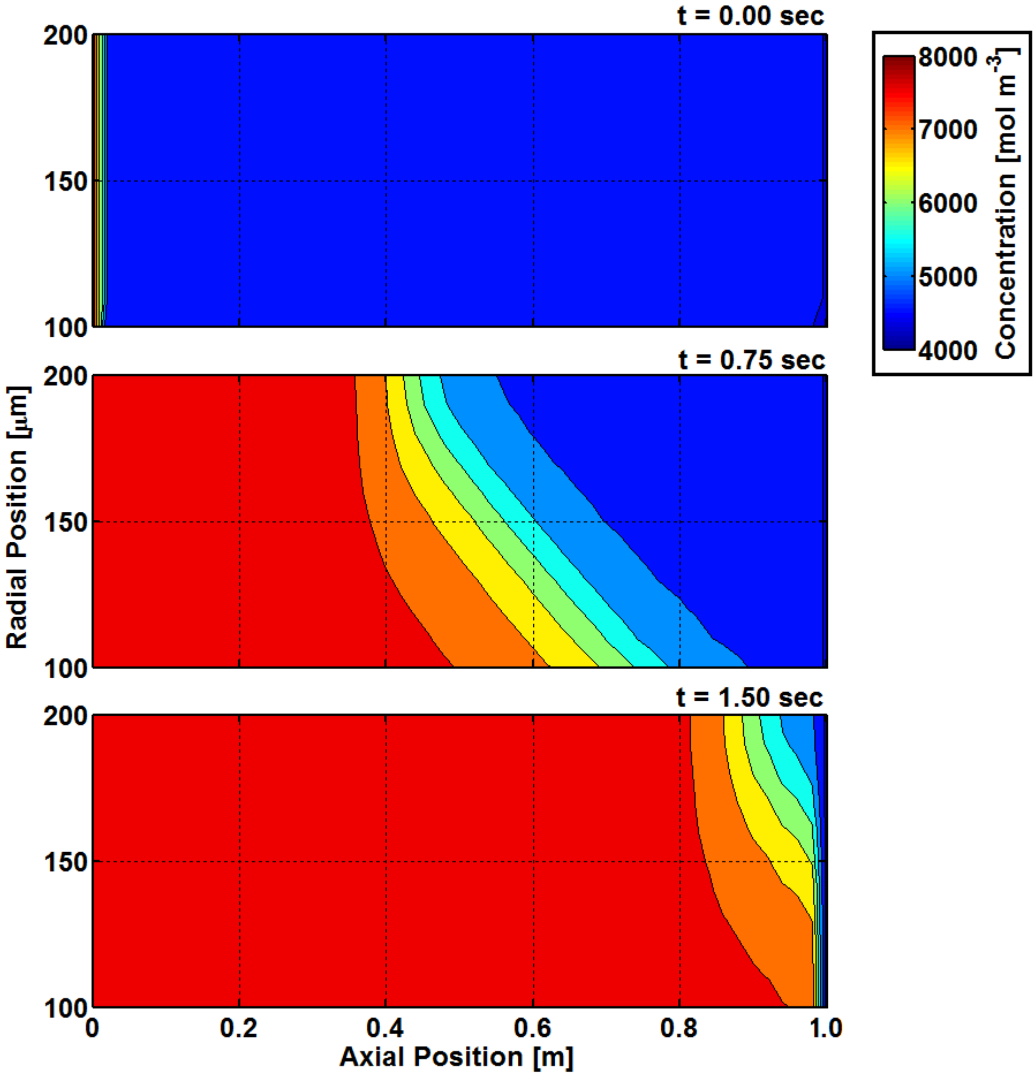

Figure 3.24: Contours of adsorbed CO_2 concentration in the adsorbent wall region, shown for the process start, 0.75 sec, and 1.50 sec.

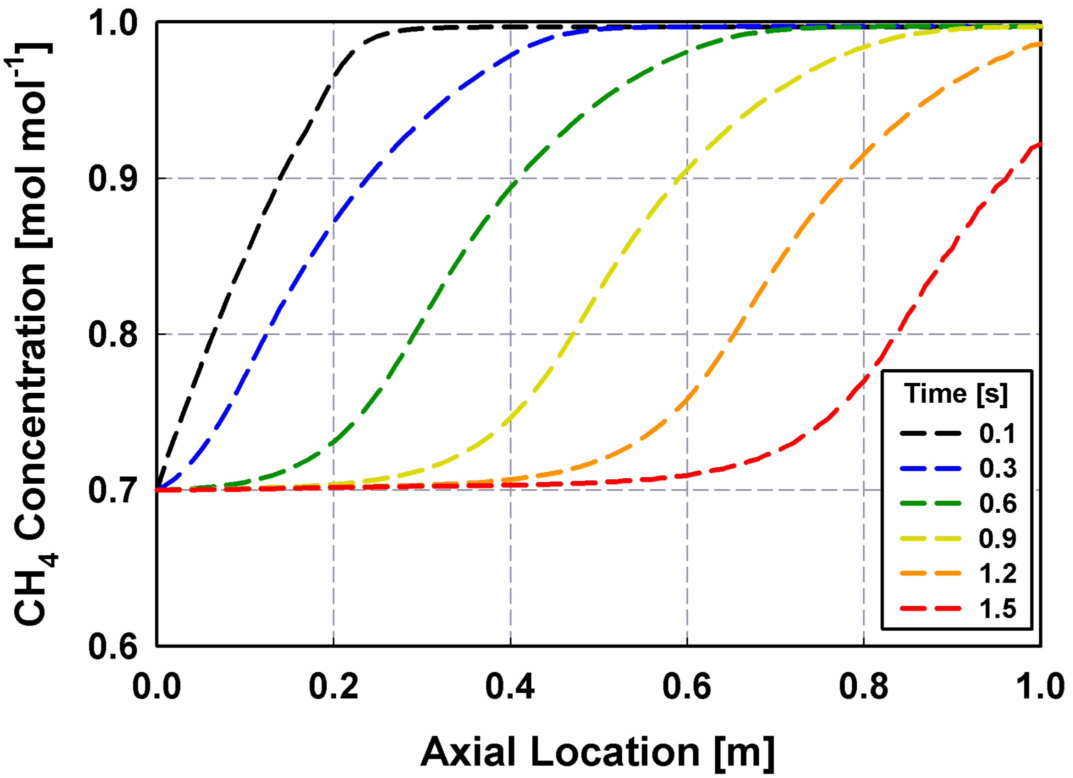

Figure 3.25: Axial profiles of CH_4 mole fraction in the fluid channel, plotted for several time steps.

Figure 3.26 shows contours of temperature for the same instances in time as pictured above, and Figure 3.27 shows the corresponding temperature profiles in the fluid channel. The localized rise in wall and fluid temperatures corresponds to the location of the adsorbed concentration front, as heat is generated due to adsorption of CO_2. However, following this initial temperature rise, the region behind the thermal wave is subsequently cooled by the inflow of fresh feed gas from the channel inlet, which enters at 25°C. The maximum wall temperature for any time step occurs axially at the center of the thermal wave, and radially near the adsorbent wall surface adjacent to the flow channel. The maximum temperature reached in the adsorbent layer during the entire adsorption process is 41°C.

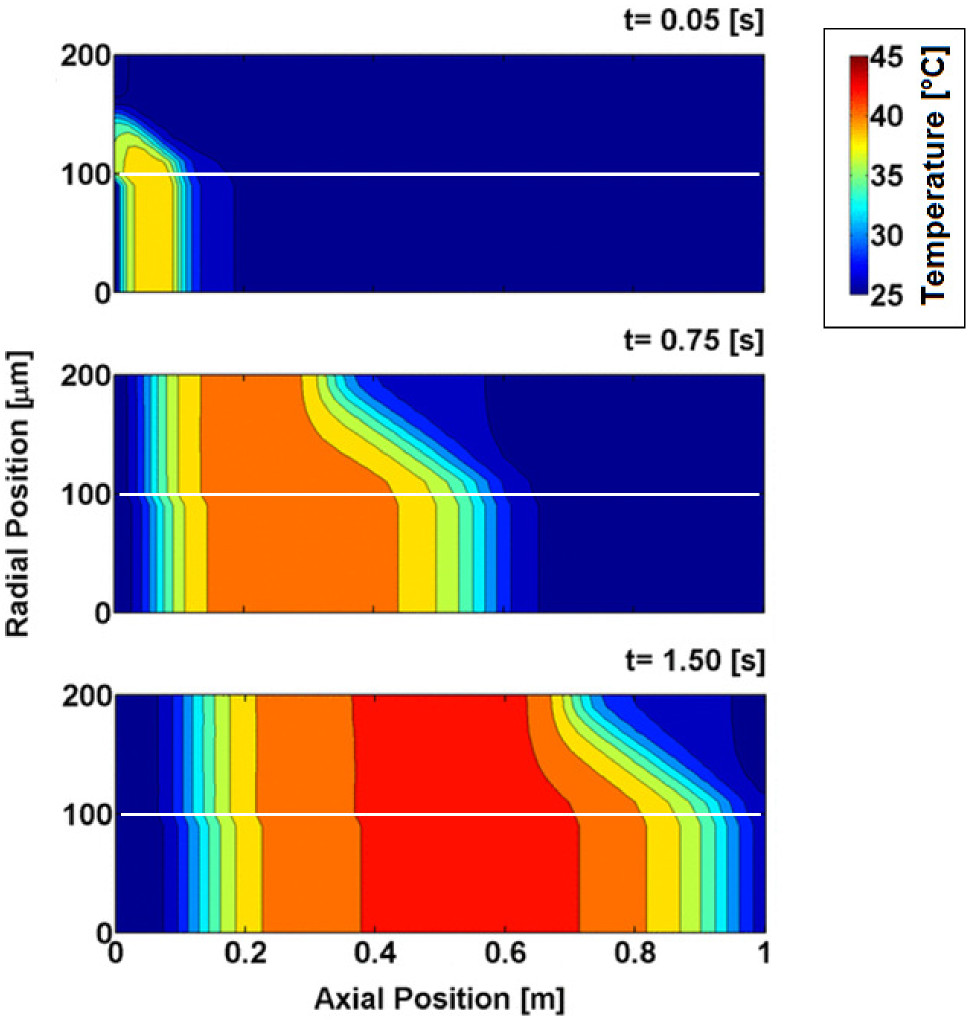

Figure 3.26: Contours of temperature in the adsorbent wall region (top) and fluid channel (bottom), shown for the process start, 0.75 sec, and 1.50 sec.

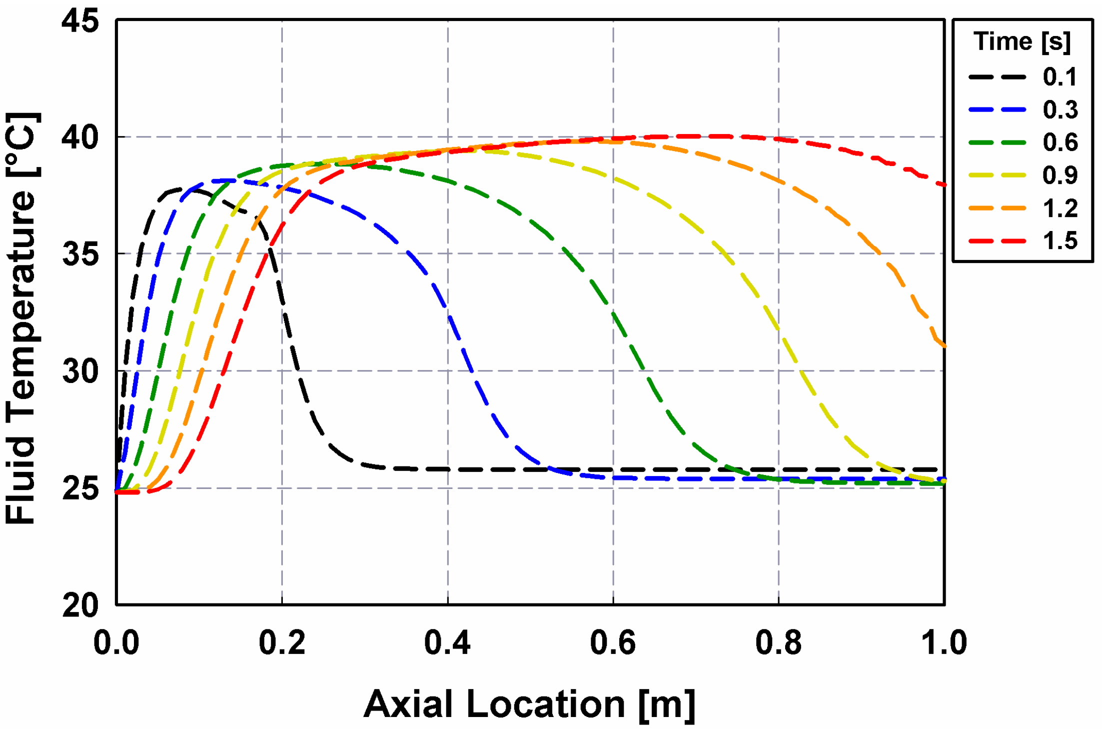

Figure 3.27: Axial temperature profiles in the fluid channel, plotted at several time steps.

The results shown above were obtained under the assumption that the inner walls of the channel were completely dry, with no liquid films retained on the channel walls. However as discussed previously, the two-phase flow characteristics during displacement do not guarantee this dry wall condition. As indicated by the review of the literature, the displacement of liquid from the channel during the process is likely to leave residual liquid on the walls of the channel, whether by transitioning into an annular flow regime or through the formation of thin films between the incoming gas slug and the channel walls.

To simulate the existence of such liquid films, the heat and mass transfer model was then slightly modified to include an additional radial diffusion mass transfer resistance to the convection mass transfer boundary condition in Equation (3.42). The modified boundary condition includes this additional diffusion mass transfer resistance for the diffusion of CO_2 and CH_4 through water. This diffusion resistance was placed in series with the existing convection resistance, and is shown in equation (3.49).

$$D\frac{\partial c_w}{\partial r}\bigg|_{r=r_{inner}} = \left(\frac{1}{h_{m,conv}} + \frac{t_{film}}{D_{H_2O}}\right)^{-1} \left(c_g - c_w\big|_{r=r_{inner}}\right) \tag{3.49}$$

The simulation was performed using this modified boundary condition and varying values of film thickness. The results of these simulations are shown in Figure 3.28, which depicts the total methane product purity versus time for a dry channel and for several liquid film thicknesses. Here total product purity is defined as the overall mass fraction of methane in the gas collected at the outlet, or the accumulated methane mass divided by the total mass outflow of gas:

$$Purity_{CH_4} = \frac{\int_0^t \left(uA_{cs} \cdot c_{CH_4}\big|_{z=L}\right) dt}{\int_0^t \left(\sum_i vA_{cs} \cdot c_i\big|_{z=L}\right) dt} \tag{3.50}$$

As is evident from Fig. 3.28, the existence of liquid films on the channel walls produces a significant change in effluent gas purity. With no liquid film present, the adsorbent channel system is able to yield outlet methane purities in excess of 95% for 2.5 seconds, with a maximum purity of 98.5%. However for liquid film thicknesses as small as 1 μm the ability of the system to meet minimum purity requirements becomes severely impaired. When continuous liquid films are present on the channel walls, the methane product purity drops almost instantaneously as the increased radial mass transfer resistance impedes diffusion into the channel walls, allowing the feed gas to essentially bypass the adsorbent layer.

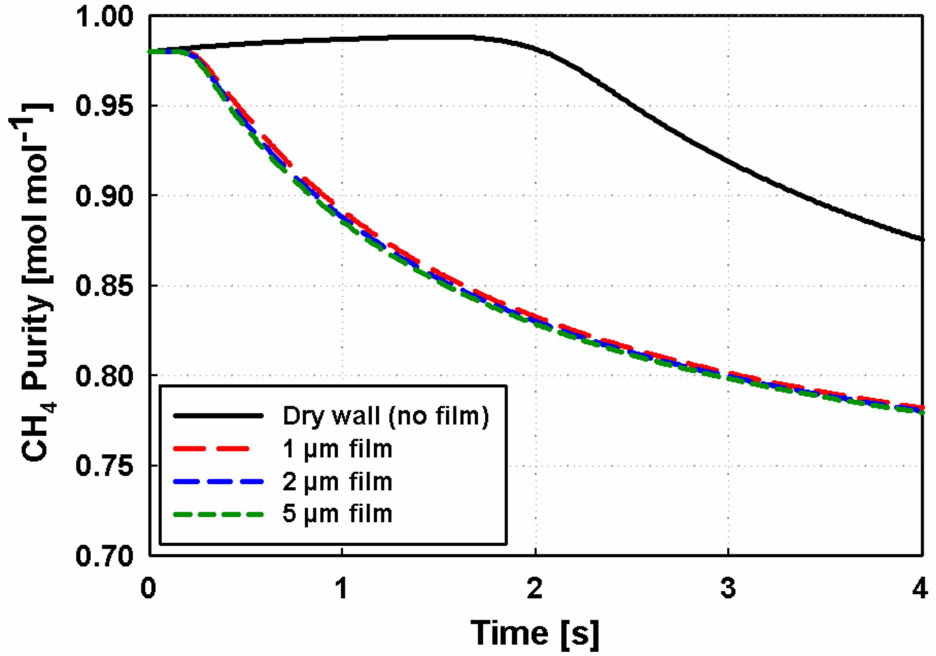

Figure 3.28: Methane outlet purity versus time for a range of residual film thickness.

The results in Fig. 3.28 clearly demonstrate the importance of understanding the multiphase flow phenomena at work in the displacement processes, and the need for the flow visualization experiments discussed in the following chapter. While a small amount of residual liquid may prove tolerable from a process standpoint, inability to mitigate or eliminate the effects of residual films in the channel could have significant impacts on overall system performance.

CHAPTER 4

EXPERIMENTS

The experimental work performed was comprised of a high-speed multiphase flow visualization study with quantitative image analysis to determine average liquid film thickness and interface velocity during air-water displacement flow in 200 µm channels. This section will outline the experimental facility design and specifications, test procedures, and the methods used for data analysis and reduction.

4.1 Experimental facility

Visualization experiments were performed by flowing air and water through transparent circular tubes with inner diameters of 203 µm, and recording video of the fluid motion using high-speed video equipment and magnifying lenses. Flow conditions were controlled by varying the driving pressure drop over a wide range (3.5 to 83 kPa), which in turn provides a range of fluid velocities over which to observe the flow behavior. Videos obtained during the course of these experiments were analyzed both qualitatively for flow pattern identification and quantitatively for void fraction, film thickness, and interface velocity estimation.

Test sections were fabricated using sections of borosilicate glass capillary channel tubing approximately 180 mm in length. Specifications for these microchannel tubes can be found in Table 4.1. The glass tubes [1] were fixed at the ends within stainless steel tubing [2] and encased within transparent plastic casing [3] in the observation area using fast-drying epoxy for structural support. The stainless steel tubes were also fitted with Swagelok fittings for simple connection to fluid lines and pressure taps. A sample test section is shown in Fig. 4.1. The steel tubing and fittings shown are ¼” (6.35 mm)

Swagelok fittings. This tubing size was chosen because it was the smallest tube size that would accommodate the outer diameter of the glass capillary channels, which have outer diameters of 3 mm (wall thickness of 1.4 mm). A stainless steel tee fitting [4] is attached to the steel tubing to allow evacuation of the region between the channel and the protective shell via the perpendicular connection; this is useful for the removal of condensation on the glass tube outer surface, which is detrimental to visualization.

Table 4.1: Specifications for glass channel tubing

Channel manufacturer	Friedrich and Dimmock, Inc
Product number	HWP-20330
Inner diameter	203 ± 7.6 μm
Outer diameter	3000 ± 127 μm
Wall thickness	1399 μm

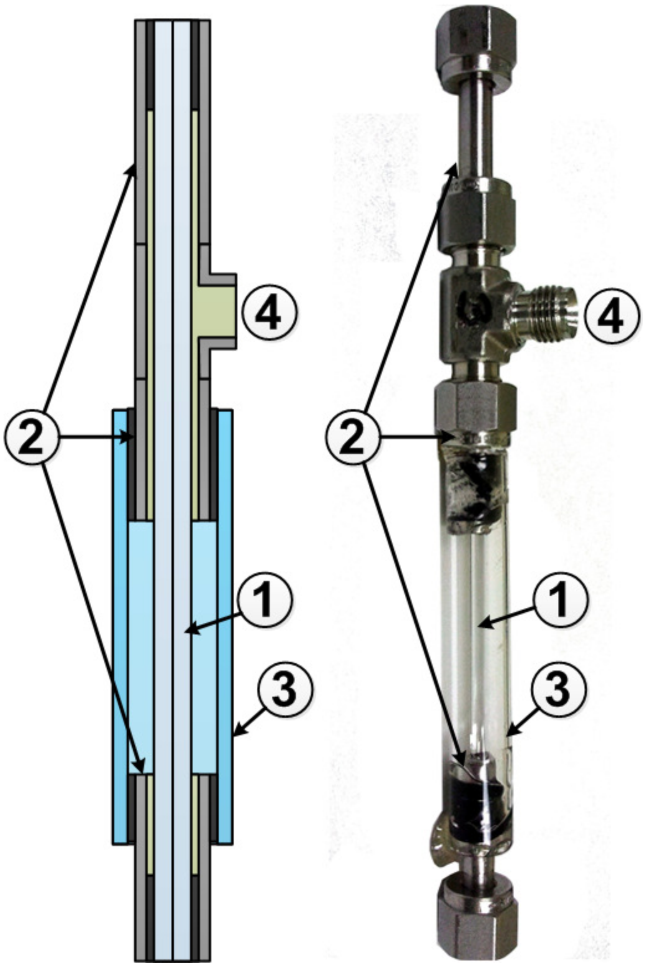

Figure 4.1: Microchannel test section diagram and an actual test section used in the displacment flow visualization study.

Because the glass capillary channels and plastic casings used were prone to breakage and scratching, several test sections were fabricated. Two such test sections were used in the present study. To properly validate the fluid flow model described in the previous chapter, gas-liquid interface velocities were observed at two axial locations for each test section. The total lengths and measurement locations of the test sections used are given in Table 4.2.

Table 4.2: Test section dimensions

Test Section	L_{total} (mm)	L_1 (mm)	L_2 (mm)
#1	178.0	87.4	140.5
#2	184.0	102.0	143.6

A compressed air line [A] is split at the system inlet to provide pressure to both the gas [B] and liquid [C] lines. Liquid is held in a 1-liter stainless steel sample cylinder [D], which is pressurized by the compressed air so that liquid is forced out of the cylinder bottom and to the test section [E]. A solenoid-controlled, pneumatically actuated T-valve [F] at the test section inlet alternates quickly between gas and liquid supply lines. The average measured valve actuation time was 38 ms; this ensures a rapid, clean displacement of one phase with another and helps to minimize mixing effects in the test section header. The test section and header are oriented vertically with flow moving downward in order to further reduce header effects, though it should be noted that in the literature it was found that channel orientation had no effect on two-phase flow behavior in the channel. A schematic of the facility is shown in Fig. 4.2 below.

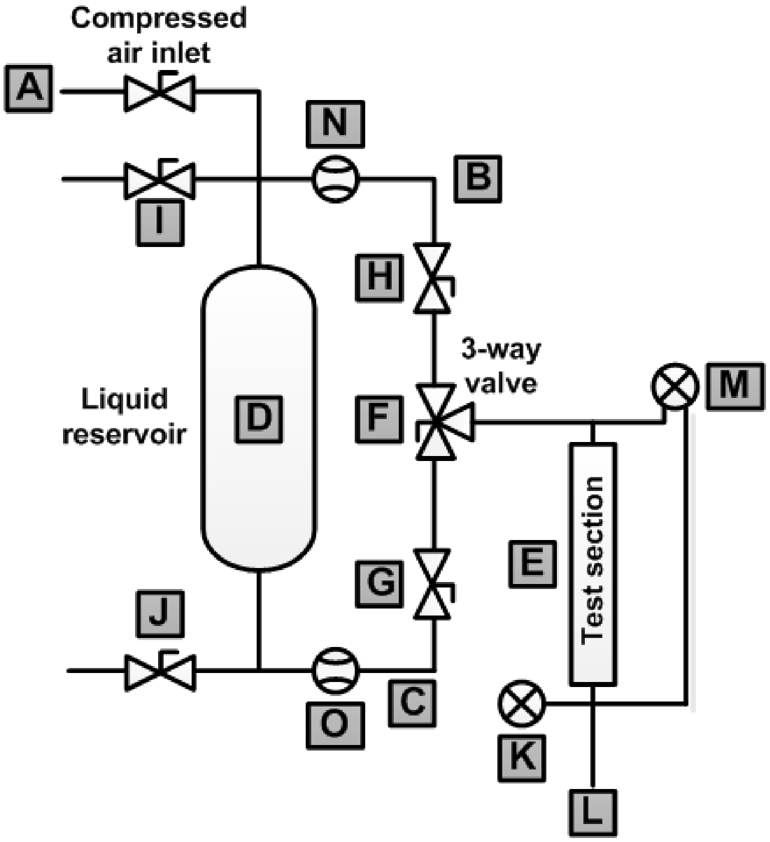

Figure 4.2: Schematic of the flow visualization facility; compressed air is used to provide both gas and liquid flow to the test section.

As shown in Fig. 4.2, the system also includes ball valves and needle valves to shut off and restrict flow through both fluid lines [G,H], and ball valves for isolation and filling of the liquid reservoir [I,J]. Tee fittings are installed at the test section inlet and outlet to provide ports for the measurement of pressure at either end of the test section. The port at the test section outlet is connected to a Rosemount 2088 transducer [K] for the measurement of gage pressure at the test section outlet [L]. A Rosemount 3051T transducer [M] measures the pressure drop across the channel. Mass flow meters [N,O] are installed on the gas and liquid lines (Omega FMA-1616A and FLR-1616A, respectively); however, the response time of these instruments proved to be too slow to obtain useful flow rate data during the transient experiments. Instrument specifications are shown in Table 4.3.

Table 4.3: Instrument specifications for flow visualization facility.

Instrument	**Type**	**Range [Span]**	**Uncertainty**
Rosemount 3051T	Differential pressure	0-250 kPa [0-172 kPa]	±0.15%
Rosemount 2088	Absolute pressure	0-5500 kPa [0-275 kPa]	±0.15%
Omega FMA-1616A	Mass flow (gas)	0-20 mL min^{-1} [0-20 mL min^{-1}]	±(0.8% of reading + 1.0% full scale)
Omega FLR-1616A	Mass flow (liquid)	0-20 mL min^{-1} [0-20 mL min^{-1}]	±2.0% of range

The analog outputs from each of these instruments were monitored using a National Instruments SCXI-1000 data acquisition system via a 32-channel SCXI-1102 card module. In addition to the pressure and flow rate measurements, the SCXI-1102 also receives a 5-volt on/off signal from the high-speed camera to indicate when the camera is recording. This signal is used within LabView to synchronize data collection with camera operation, so that the flow conditions can be precisely monitored during the transient process. Solenoid valve operation was controlled by the same data acquisition system using a SCXI-1161 power relay switch module. The SCXI-1000 system was connected via USB to a PC running a LabView VI, which was responsible for synchronization of data collection with camera operation, data collection, and file save operations.

A Photron Fastcam model SA-4 was used for the high-speed video recording. This camera is capable of capturing full-resolution (1024×1024 pixel) images at up to 3600 frames per second (fps), and, with reduced resolutions, can record at up to 500,000 fps. For the experiments performed here, videos were captured between 1000 and 2000 frames per second, with exposure times between 2×10^{-4} (1/5000) and 1×10^{-5} (1/10000) seconds. A Navitar 12X series lens with adjustable aperture and magnification, along with a 2X and 0.75X removable adapters was attached to the camera. In combination, this configuration provided variable optical magnification from 4× to 8×. To achieve fine adjustments and focus, the camera was mounted on a Newport Optics model 423 linear translation stage with a 100 thread-per-inch axial adjustment screw. Illumination of the test section was provided by three 500 watt incandescent lamps aimed at a semi-cylindrical diffuser placed concentrically around the test section. The diffuser was placed approximately 50 mm away from the test section surface. A schematic of this configuration is shown in Figure 4.3.

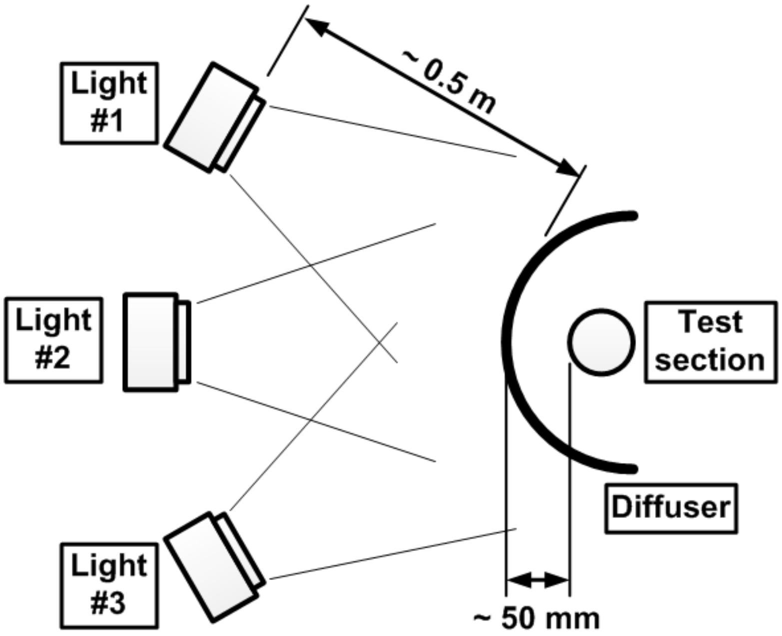

Figure 4.3: Schematic of the lighting configuration used in flow visualization experiments.

The camera was connected to the data acquisition PC by CAT6 Ethernet connection, and connected (as mentioned previously) to the data acquisition system through one of the camera's hardware voltage outputs for camera trigger synchronization. To eliminate the lag associated with operating the camera trigger using the camera software (which is routed through the Ethernet connection), the camera trigger was slaved to a hard-wired on/off voltage input, which could be controlled either by hand or though the switch module on the data acquisition system. The camera was placed in end-trigger mode (continuous recording though a first-in-first-out buffer) to record the behavior of the liquid-gas interface and subsequent two-phase flow phenomena after initial displacement. Due to camera memory constraints at high frame rates and resolutions, all flow visualization video samples were analyzed for void fraction over a one second interval. A picture of the full test facility is shown in Fig. 4.4.

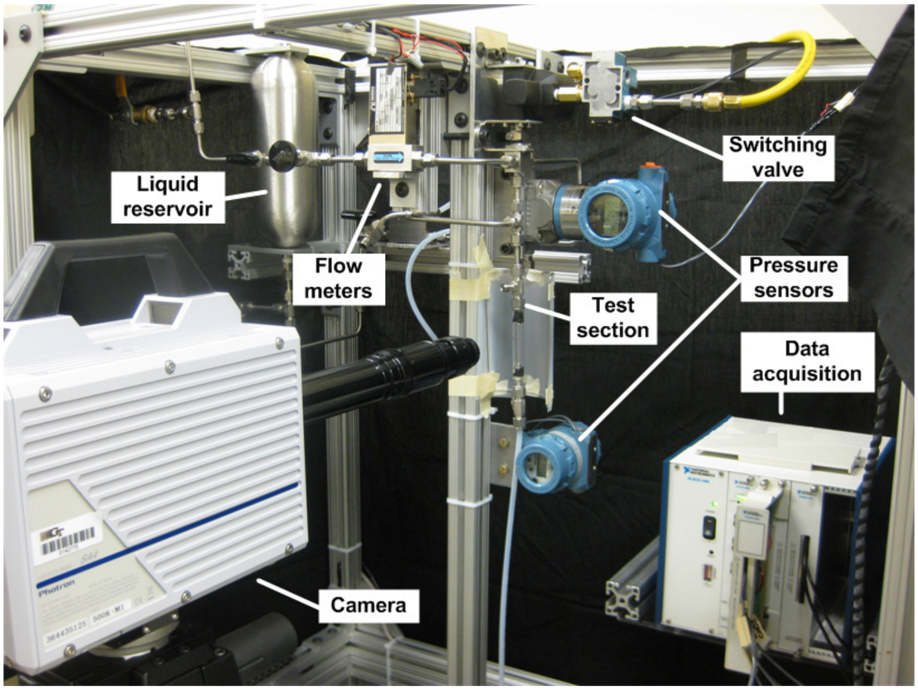

Figure 4.4: Photograph of the flow visualization test facility

Tests were performed over a range of driving pressure gradients from 20 kPa m^{-1} to 500 kPa m^{-1}. Video and pressure data were recorded for the displacement of gas by liquid and the displacement of liquid by gas; 30 samples were obtained for gas displacement and 33 samples were obtained for liquid displacement. Video was analyzed for liquid-gas interface velocity and for channel void fraction, which was used to calculate film thickness. Interface velocity was measured using the channel diameter and camera frame rate as references for distance and time. The data and image analysis procedures for void fraction and film thickness are discussed in subsequent sections.

The complete test matrix used in the present study is shown in Table 4.4.

Table 4.4: Test matrix for the present study.

		~100 kPa m^{-1}		~150 kPa m-1		~200 kPa m-1		~250 kPa m-1		~300 kPa m-1		350 kPa m-1	
		dP/dx [kPa m^{-1}]	v [m s^{-1}]	dP/dx [kPa m^{-1}]	v [m s^{-1}]	dP/dx [kPa m^{-1}]	v [m s^{-1}]	dP/dx [kPa m^{-1}]	v [m s^{-1}]	dP/dx [kPa m^{-1}]	v [m s^{-1}]	dP/dx [kPa m^{-1}]	v [m s^{-1}]
Displacement of Liquid by Gas	Axial Location #1	59.9	0.20	173.0	0.55	198.9	0.82	207.7	0.61	287.1	0.64	371.3	0.75
		75.5	0.28	175.2	0.49	204.2	0.64	237.6	0.74	300.8	0.86	384.8	0.44
		116.8	0.42	175.9	0.42							391.4	0.67
												491.3	0.90
	Axial Location #2	19.9	0.16	121.3	0.58	168.8	0.92	252.3	1.16	307.7	1.68	367.5	1.65
		66.1	0.33	122.5	0.58	234.8	1.05	286.7	0.91	330.2	1.43	389.1	1.44
		77.3	0.47	168.5	0.73							411.9	2.13
		87.2	0.41									437.1	1.79
Displacement of Gas by Liquid	Axial Location #1	28.0	0.09	95.6	0.28	175.6	0.39	248.7	0.65	367.4	0.63	440.6	0.88
		37.1	0.18	125.7	0.37	200.0	0.48	249.9	0.59	383.6	0.65	465.4	1.00
				141.7	0.44	235.9	0.59						
	Axial Location #2	43.6	0.07	138.3	0.25	157.2	0.25	221.8	0.28	282.9	0.34	347.2	0.45
		75.1	0.11	146.6	0.21	170.7	0.17	282.5	0.32	305.8	0.37	352.2	0.48
		86.5	0.13	153.7	0.22	214.7	0.27						
		107.9	0.16										

4.2 Flow patterns observed

Although displacement of a single phase by another phase is distinct from the modes of flow for two-phase flow investigations in the literature, similar trends were observed. As observed in the literature, different multiphase flow patterns appear as the flow rates of the liquid and gas phases are increased or decreased. For the displacement of liquid, the flow regimes observed were dry/thin film, ring-film intermittent flow (slug flow), and rivulet flow. For the displacement of gas, regardless of velocity, only one flow pattern appeared: a stable slug of liquid cleanly displacing the gas in the channel. This section will describes the flow patterns observed in the present study.

4.2.1 Displacement of liquid – Dry/thin film flow

At low velocities (less than 0.7 m s^{-1}), the incoming gas displaces the liquid in the channel smoothly, leaving little or no liquid behind on the channel walls. As noted by Zhao (2001) and Serizawa *et al.* (2002), in channels with diameters on the order of 200 μm, the surface tension forces are sufficiently dominant that stationary gas bubbles in the channel were observed having dry contact with the channel walls; no liquid film was observed between the gas slug and the wall.

A similar phenomenon was observed in the present study in displacement flow samples obtained at low velocities. In several of these samples, the incoming gas slug appears to occupy the entire channel cross section, leaving behind dry channel walls or extremely thin liquid films. At these low fluid velocities, the influence of viscous forces, which are roughly proportional to ρv^2, has not yet overtaken the influence of surface tension forces at the liquid-gas interface, which remain constant with varying velocity. As a result, very little liquid is left behind on the channel walls, although in some cases thin liquid rings were observed moving axially down the channel. A time-lapse sequence of sample images for thin/dry film flow is shown in Fig. 4.5.

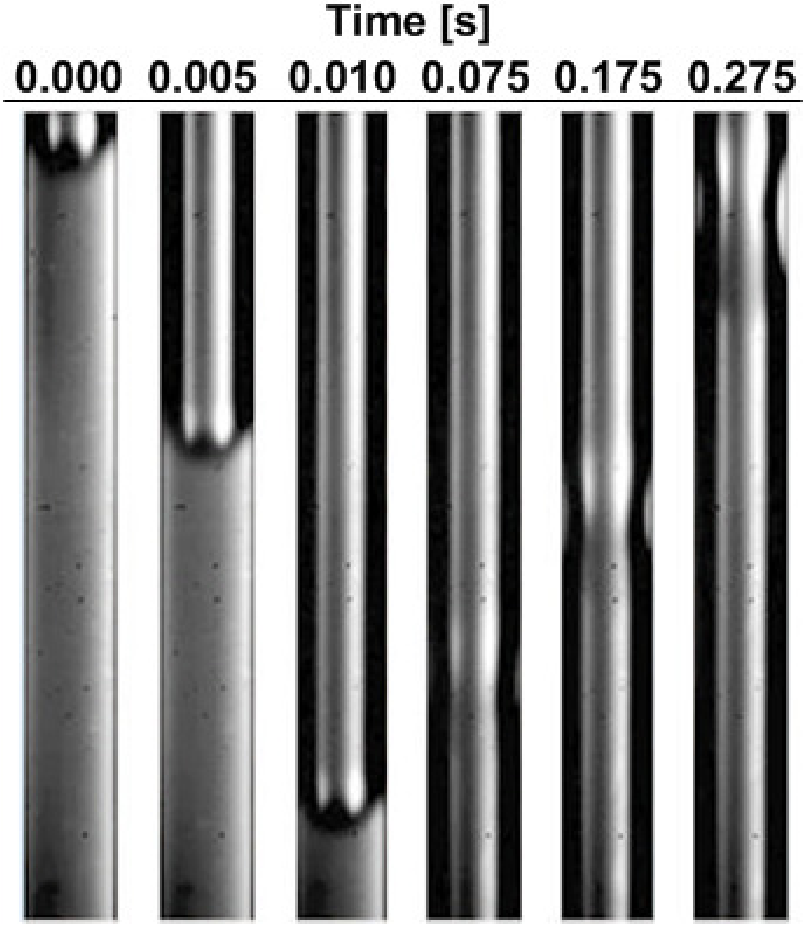

Figure 4.5: Time-lapse images of liquid displacement leaving a partially dry wall. Sample obtained with an interface velocity of 0.16 m s^{-1}. After the initial displacement small liquid rings were observed flowing through the channel.

For the adsorption process under consideration, this flow pattern is desirable from a mass transfer standpoint, but increases process time. The presence of dry channel wall area or extremely thin liquid films provides low mass transfer resistance for the diffusion of channel gases into the walls. However, to obtain these favorable mass transfer characteristics, the fluid velocity must remain fairly low, increasing process time. In addition, if liquid is retained on the channel walls, these relatively low gas velocities will do little to remove the residual liquid from the channel, thus increasing mass transfer resistances.

4.2.2 Displacement of liquid – Ring-film flow

As the fluid velocity in the channel increases, the magnitude of viscous forces increase proportionally to ρv^2. Because a stable liquid-gas interface is maintained by surface tension forces, which remain essentially constant with changing flow conditions, the front of the incoming gas slug deforms and elongates. Eventually, the bubble front elongates to the point where liquid on the walls slips around the edges of the gas slug, remaining on the channel walls and forming a continuous liquid film. At moderate to high interface velocities (0.4 to 1.4 m s^{-1}), this residual liquid film is easily visible as the gas slug passes through the channel and is identical to the annular or "liquid ring" flow patterns identified in the literature.

In this flow pattern, the fluid velocity in the gas core is greater than the velocity of the liquid on the channel walls. The interfacial shear forces between the gas and liquid phases drives the liquid in the annular films down the channel. These shear forces also cause liquid to gather into wrinkles or rings, forming a wavy continuous film on the channel wall. This creates the wavy behavior shown in the time-lapse images in Fig. 4.6.

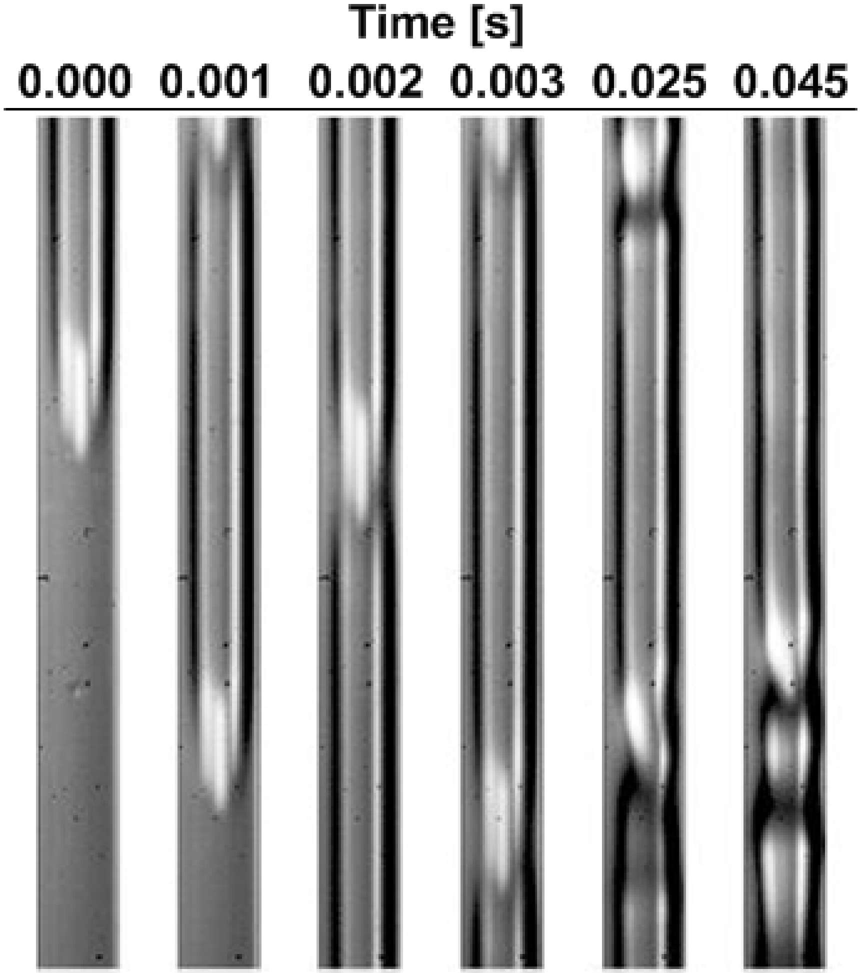

Figure 4.6: Time-lapse images of displacement with liquid ring-films, obtained at an interface velocity of 1.79 m s^{-1}. The initial liquid-gas interface is highly deformed and the wavy films that follow are easily visible on the walls.

The ring-film flow pattern is the most detrimental flow pattern for system mass transfer performance. Because the entire interior wall surface is coated with liquid, the diffusion mass transfer resistances for water and the wall polymer are in series. As discussed previously, the diffusion mass transfer resistance of liquid water is orders of magnitude greater than that of the wall polymer. The observed liquid films are easily visible in the video frames, with film thicknesses in excess of 10 μm. As demonstrated in the modeling section, these thick films will severely inhibit diffusion and adsorption of the gaseous contaminants into the channel walls.

4.2.3 Displacement of liquid – Rivulet flow

At high interface velocities (greater than 1.0 m s^{-1}), or as the supply of liquid on the channel walls is depleted as it is sheared down the channel, liquid on the walls is driven into rivulets or droplets. These rivulets can be axially continuous, but do not cover the entire channel surface. Interfacial shear between the gas and the liquid rivulet surface drives flow of liquid down the channel through the rivulet, also in most cases causing the rivulet to change its course. As the flow of gas continues, the liquid continues to be driven down the channel, depleting the supply of liquid upstream and causing the rivulets to become smaller. When the liquid becomes scarce enough, the rivulets may turn into discrete droplets stuck to the channel walls. These droplets are also carried down the channel by the flow of gas until eventually the channel is dry. Fig. 4.7 shows a time-lapse sample of rivulet flow developing from ring-film flow.

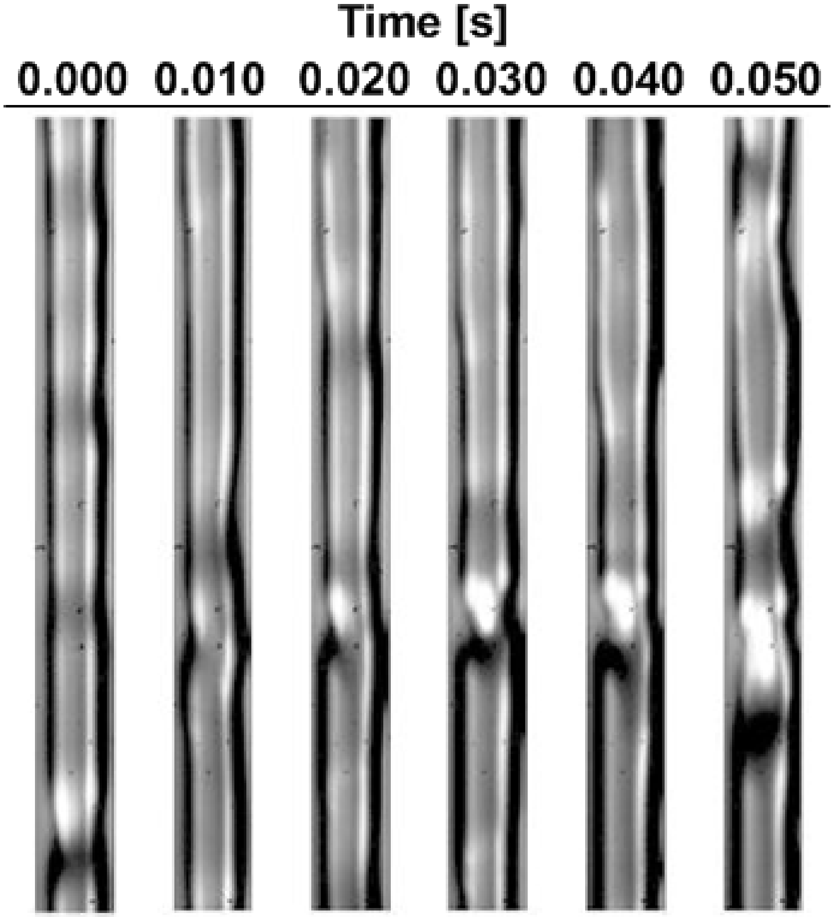

Figure 4.7: Time-lapse images of rivulet flow. The flow begins as a ring-film, but transitions into liquid flow as the liquid supply is depleted. Portions of dry wall are visible and liquid gathers into asymmetric rings and droplets on the walls.

Rivulet and droplet flows are desirable from a process mass transfer perspective because despite the presence of residual liquid on the channel walls a significant amount of dry wall surface area is available for diffusion. In contrast to flow patterns with continuous annular films, which place the film diffusion resistance in series with the wall diffusion resistance, rivulet flow places dry portions of the channel wall in parallel with the liquid-coated portions, as shown in Figure 4.8.

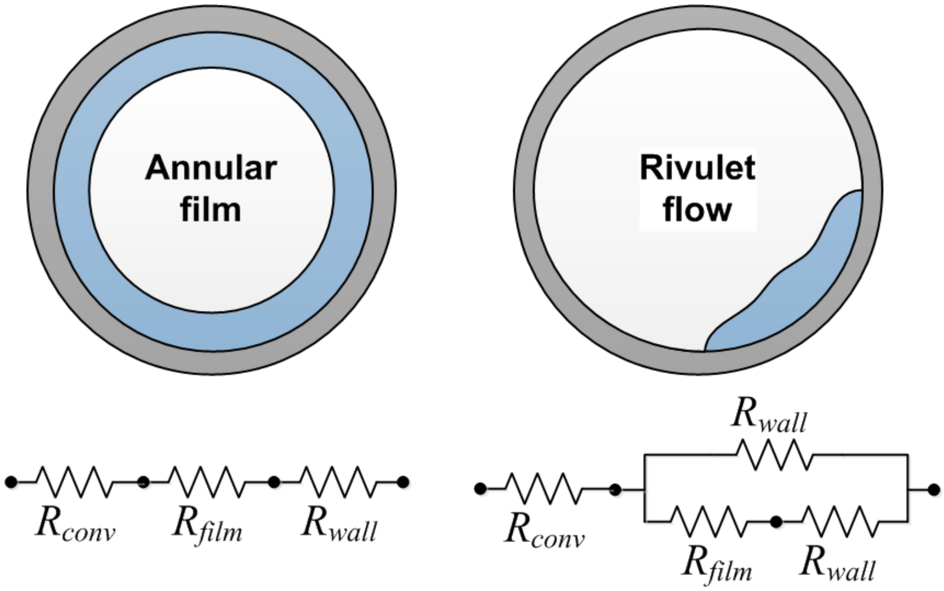

Figure 4.8: Schematic of heat and mass transfer resistances in annular and rivulet flow patterns.

In the scenario shown in Figure 4.9 on the right, the resistance for the liquid-coated wall area is placed in parallel with the resistance for the dry wall area, allowing gaseous contaminants a path of lower resistance into the adsorbent region. In addition, the high gas flow rates associated with rivulet flow will purge liquid from the channel more quickly, but this fast flow of gas may also create a less distinct concentration front in the adsorbent and may ultimately decrease adsorbent utilization, as the feed gas mixture residence time in the adsorbent is lower.

4.2.4 Displacement of liquid – Intermittent flow

In some cases at moderate interface velocities (0.4 to 1.4 m s^{-1}), the existence of separate liquid slugs (instead of a single continuous incoming slug) was observed. In Fig. 4.6, these slugs appear to be departing from the main incoming gas region, and seem to be formed as the magnitude of surface waves in the wall film increases to a point where continuous liquid bridges can be formed within the gas region. Fig. 4.9 shows a time-lapse sequence in which the main incoming gas slug is preceded by smaller gas slugs. Thick ring-films are present on the walls within the main gas region, and near the front of the main slug, these waves in the film are shown coalescing into a continuous liquid bridge. As gas flow continues and the main gas slug moves down the channel, the frequency and magnitude of the surface waves decrease as the supply of liquid on the walls is diminished and no new slugs are formed.

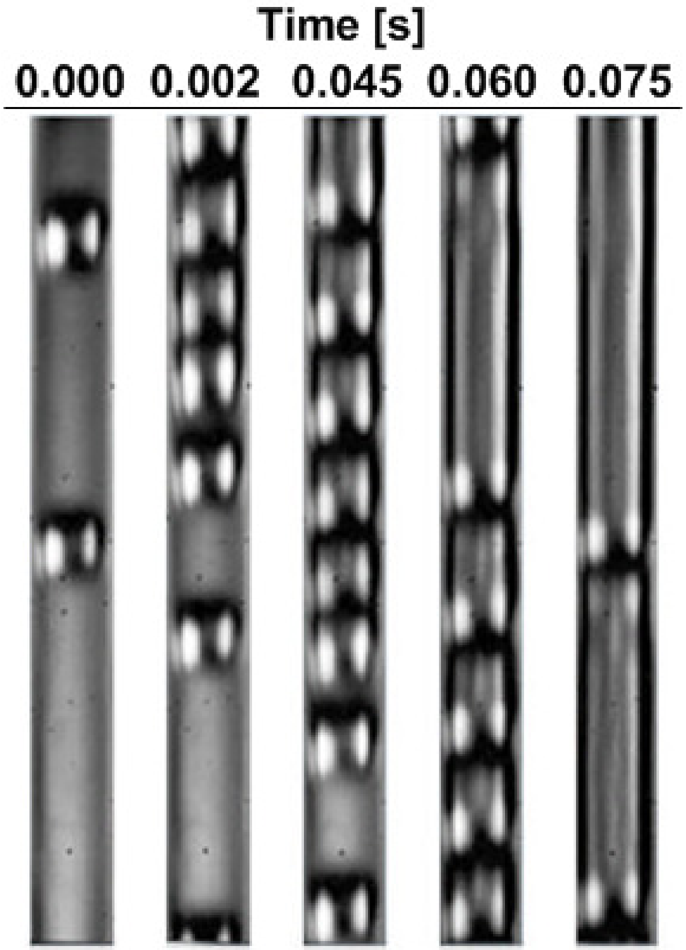

Figure 4.9: Displacement of liquid with an intermittent flow pattern. Slugs shown are moving at 0.897 m s^{-1}. Separate slugs are seen forming at the front of the incoming gas due to waves in the surface film. A thick wavy film pattern follows the initial slugs.

It is important to note that this flow pattern was rarely seen; of the 17 liquid displacement samples observed in this velocity range, only four exhibited this intermittent flow behavior. Furthermore, this phenomenon was only observed at the first channel location, which may indicate that the existence of separate gas slugs may be an entrance or header phenomenon, or that the individual slugs may re-coalesce with the main gas region as the gas travels down the channel.

From a process mass transfer perspective, the intermittent flow pattern is undesirable. There are observable liquid films surrounding each of the gas slugs, and as gas flow continues and the liquid supply is diminished, this flow pattern transitions into ring-film flow. Mass transfer resistances in this flow pattern are very high, and significant amounts of liquid remain on the channel walls.

As discussed in the review of the literature, flow patterns in channels on the order of 100 μm are seldom constant, and at a given set of flow conditions, any number of flow patterns can be observed. It is for this reason that studies such as those of Chung *et al.* (2004) and Kawahara *et al.* (2002) identify flow regimes in terms of time-averaged probability of flow pattern appearance.

The results of this study are consistent with those from these previous studies; in a given 1-second sample video, the flow pattern was often observed to alternate between ring-films and rivulet flows, or from dry walls to rivulets and thin films as droplets or liquid rings passed through. Fig. 4.10 shows the occurrence of each flow pattern in terms of the recorded interface velocity. As the figure demonstrates, there are significant regions of overlap between the two patterns, presenting challenges for the accurate prediction of flow pattern occurrence.

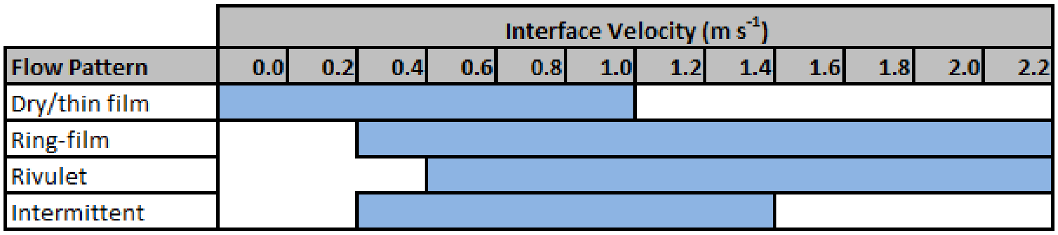

	Interface Velocity (m s^{-1})											
Flow Pattern	**0.0**	**0.2**	**0.4**	**0.6**	**0.8**	**1.0**	**1.2**	**1.4**	**1.6**	**1.8**	**2.0**	**2.2**
Dry/thin film	🟦	🟦	🟦	🟦	🟦	🟦						
Ring-film			🟦	🟦	🟦	🟦	🟦	🟦	🟦	🟦	🟦	🟦
Rivulet				🟦	🟦	🟦	🟦	🟦	🟦	🟦	🟦	🟦
Intermittent			🟦	🟦	🟦	🟦	🟦	🟦				

Figure 4.10: Flow pattern appearance shown in terms of observed interface velocity.

4.2.5 Displacement of gas

As mentioned previously, only one flow pattern was observed during the displacement of gas by liquid, a clean displacement with a single continuous slug of liquid pushing the gas out of the channel. A time-lapse sequence of the liquid interface movement is shown in Fig. 4.11. Because the purpose of this displacement step is simply to transfer heat from the liquid to the adsorbent wall layer, and because the liquid is in direct contact with the wall regardless of the flow conditions, the two-phase flow characteristics present in the displacement of gas have little effect on the overall performance of the system.

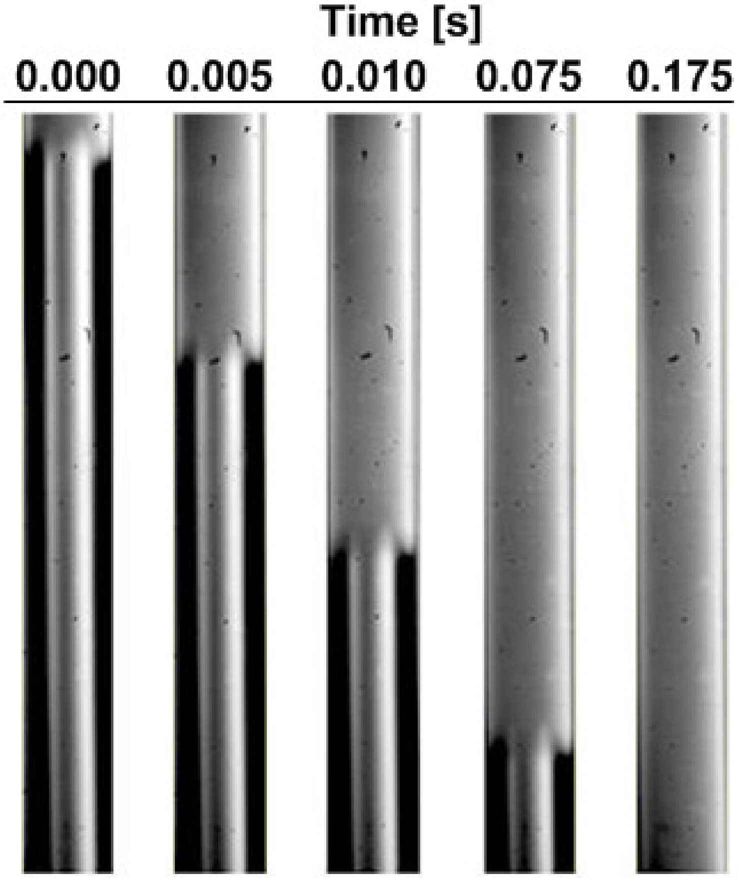

Figure 4.11: Time-lapse images from displacement of gas, captured for an interface velocity of 0.11 m s^{-1}. A continuous slug of liquid smoothly displaces the gas in the channel.

4.3 Data reduction and analysis

4.3.1 Image analysis

Because of the need to precisely determine film thickness, it was necessary to use a method that would accurately determine liquid-gas interface locations and infer three-dimensional information about the flow from these two-dimensional interface locations. To accomplish this, a program was developed using the image processing and edge detection capabilities built into MATLAB. Originally developed for the observation of falling films and droplets, the edge detection program was then modified for use in the calculation of vapor bubble parameters and void fraction in condensing flow through small hydraulic diameter tubes (Killion and Garimella, 2004; Keinath and Garimella, 2010). A brief description of the operation of the image analysis tool is provided below; additional details are available in Killion and Garimella (2004).

The program allows video files to be loaded into a graphical user interface (GUI) and observed frame by frame as stationary images. In each frame, the user defines a region of interest (ROI) by providing graphical input near visible liquid-gas interface locations. The program then performs a spline fit over the user-defined points, taking the ROI to be within a user-defined pixel distance of the calculated spline. The program searches within the ROI using the Canny edge detection algorithm to find liquid-gas interface locations.

The Canny algorithm is comprised of multiple steps (Canny, 1986). First, a Gaussian smoothing filter is applied to the data in the ROI to remove image noise and undesirable textures. Next, the data in the ROI are analyzed using the Sobel operator, which performs vector calculations on image intensity data to yield the direction and magnitude of the opposite of the image intensity gradient at each point. Essentially, this computation allows for the identification of the largest spatial derivatives from light to dark at each point. The user defines threshold values for these derivatives, and any computed result larger than these threshold values is considered to be an edge point. The user may also define edge points not detected by the Canny algorithm based on visual identification of edges if needed, and the spatial interval for edge detection can be reduced or increased to emphasize fine edge detail or computational efficiency. Once all the desired edge points have been identified, a cubic spline fit is once again performed to find the smoothest spline fit within a user-defined tolerance of the detected edge points. These spline data are saved in a matrix that provides a two-dimensional image of the features in the channel. These images are shown in Fig. 4.12.

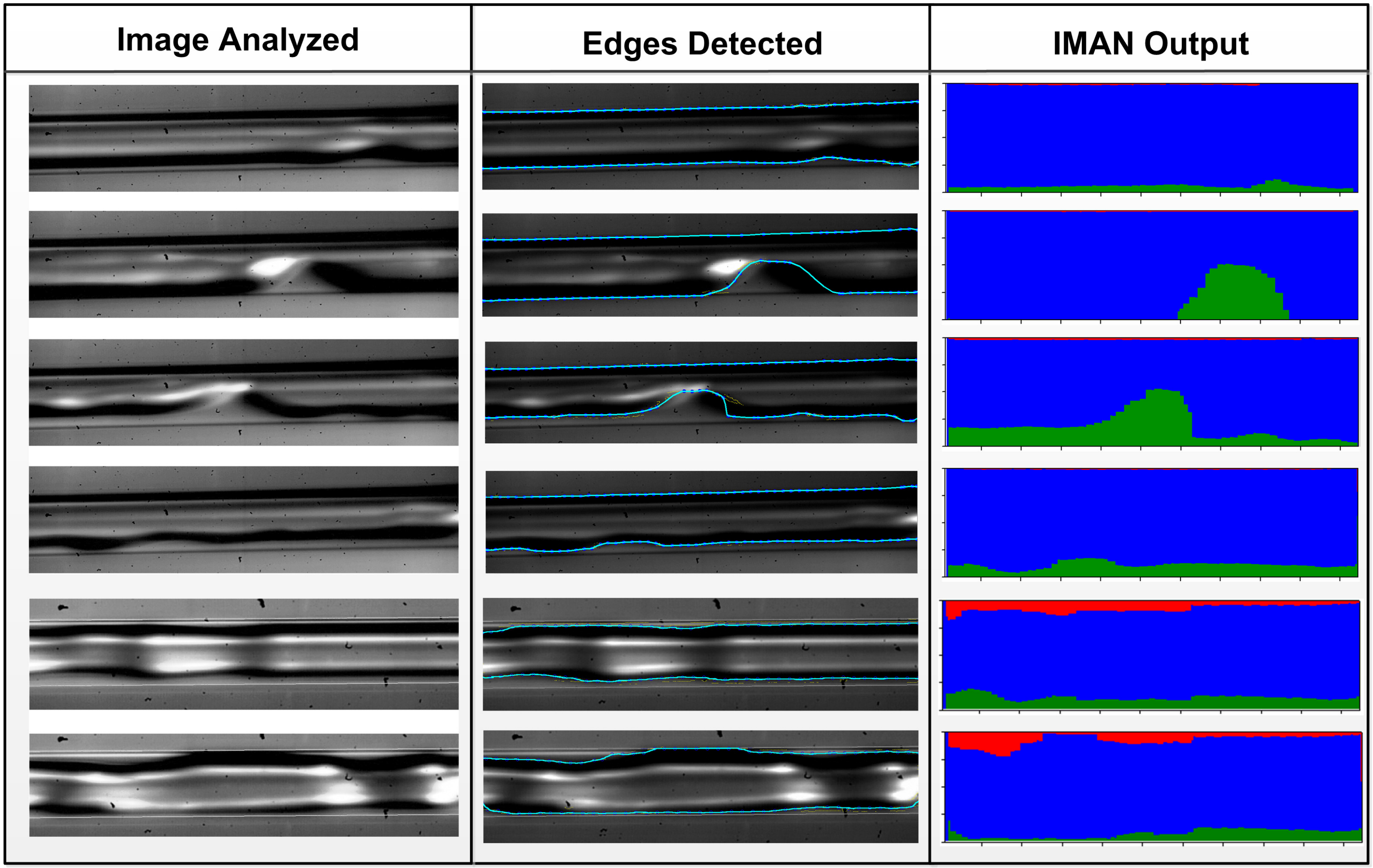

Figure 4.12: Sample flow visualization images (left column), their corresponding detected edges (center column), and program output (right column).

The spline described previously is the basis for calculation of bubble parameters, void fraction, and film thickness. For example, the maximum bubble or gas core diameter is taken to be the maximum vertical distance between any two spline points at the same axial location. Bubble length is taken to be the difference between the position of the right-most and left-most spline points. These measurements are taken in terms of pixels and are converted to lengths using the known channel diameter as the reference length. Interface velocities are computed simply using the change in position of the right-most or left-most point in a spline between consecutive frames, using the known camera frame rate as a time reference.

For void fraction calculations, three-dimensional geometries are assumed based on the general characteristics of the flow so that the void volume can be accurately estimated. The void volume can be assumed to have one of two geometries: cylindrical and partial-cylindrical. Schematic representations of these assumptions are shown in Fig. 4.13.

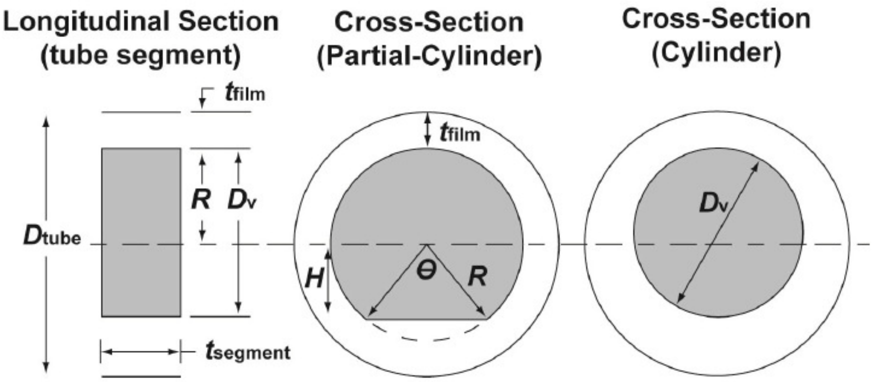

Figure 4.13: Schematic representation of geometric assumptions used in void fraction calculations (Keinath and Garimella, 2010).

A cylindrical geometry assumes that the void region in the channel has a roughly circular cross section, and therefore that the calculated bubble or gas core diameter $D_{g,i}$ is the diameter of a cylinder. The cross-sectional area $A_{cs,i}$ of the gas region at any axial location is given by:

$$A_{cs,i} = \frac{\pi}{4} D_{g,i}{}^{2} \tag{4.1}$$

Total gas volume is then calculated by summing the volumes of finite cylinders over the axial domain. This cylindrical assumption is generally valid for flows in small tubes, in which gravity has little effect on flow pattern, and in flow regimes such as annular or intermittent flow. This assumption was used for flow images containing dry/thin film, ring-film, and intermittent flow patterns.

In the rivulet flow regime, thick asymmetric films occupy the radial limits of the channel and leave portions of the wall dry. In these cases, the partial-cylindrical assumption provides a more accurate representation of the channel void fraction, as shown in Figure 4.14.

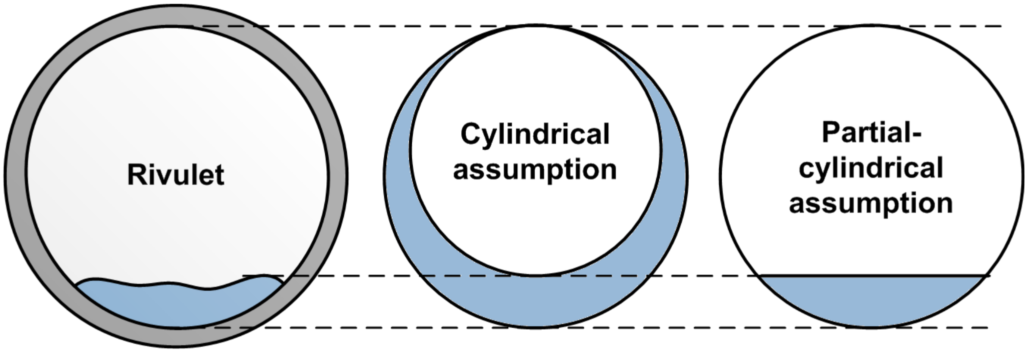

Figure 4.14: Schematic of void fraction calculations for a rivulet using the cylindrical and partial cylindrical assumptions.

The partial-cylindrical assumption takes into account the film thickness at the top of the tube, which is calculated using the distance between the top of the spline and the channel wall. This film thickness is used to calculate a reduced inner radius of the partial-cylinder.

$$R_{reduced} = \frac{D_{tube}}{2} - t_{film} \tag{4.2}$$

There are two separate equations used to calculate the gas region cross section from this reduced radius, depending on the liquid height.

$$A_{cs,i} = \begin{cases} \frac{1}{2}R^2\left(\theta - \sin\left(\theta\right)\right) & H > 0 \\ \frac{1}{2}R^2\left(2\pi - \theta - 2\sin\left(\theta\right)\right) & H < 0 \end{cases} \tag{4.3}$$

$$\theta = 2\arctan\left(\frac{R}{H}\right) \tag{4.4}$$

As in the case of the cylindrical assumption, the total gas volume is obtained by summing the volumes of each of these discrete partial-cylindrical volumes along the axial domain. Void fraction is computed by dividing the total gas volume by the visible channel volume. This void fraction reading is spatially averaged over the entire visible axial domain, and is referred to as the total void fraction.

$$\alpha = \frac{4V_g}{\pi {D_h}^2 L_v} \tag{4.5}$$

Void fraction values were also measured at the axial centerpoint of the viewed portion of the channel, as shown in Figure 4.15. This measurement takes only the gas-occupied area at the center location into account rather than calculating void fraction over the entire visible channel length. Due to the fact that this void fraction reading is not averaged over the axial length, the centerpoint void fraction reading is more sensitive to individual droplets, waves, and other flow features that pass through the channel. This reading provides a more rapidly varying response, capturing fast transient flow behavior in more detail than the total void fraction reading. The centerpoint void fraction is calculated according to Equation (4.6).

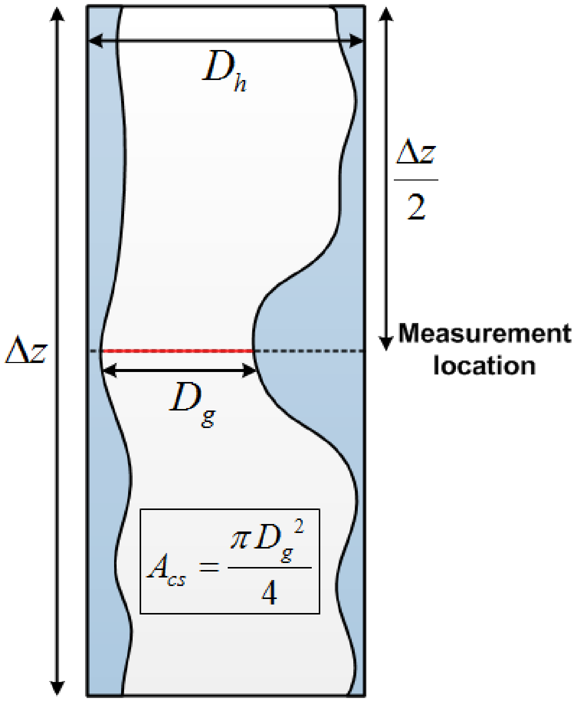

Figure 4.15: Diagram illustrating centerpoint void fraction measurement.

$$\alpha_{center} = \frac{4A_{cs,i}}{\pi D_h^2} \tag{4.6}$$

Finally, average film thickness can be calculated from these void fraction readings by assuming an annular flow profile, a cylindrical gas core with uniform film thickness. From the void fraction and the hydraulic diameter of the channel, average liquid film thickness can be calculated according to Equation (4.7).

$$t_f = \frac{D_h}{2}\left(1-\sqrt{\alpha}\right) \tag{4.7}$$

4.3.2 Uncertainty analysis

Experimental uncertainties were estimated for film thickness, pressure measurements, and velocity measurements. Because the data for film thickness and velocity rely on image analysis results, the uncertainty of the image analysis process itself must be analyzed. First, the sensitivity of the image analysis data to the sample interval was evaluated. This was accomplished by analyzing every frame of a 1.0 second sample video (a total of 1000 frames) for average and centerpoint void fraction. Having obtained void fraction results for each frame, it was possible to observe the effect of the sample interval. Fig. 4.16 shows sample void fraction data plotted at sampling intervals from 5 to 100 ms. As sample interval increases, the plots lose resolution and the void fraction deviates from the values obtained at larger sampling frequencies.

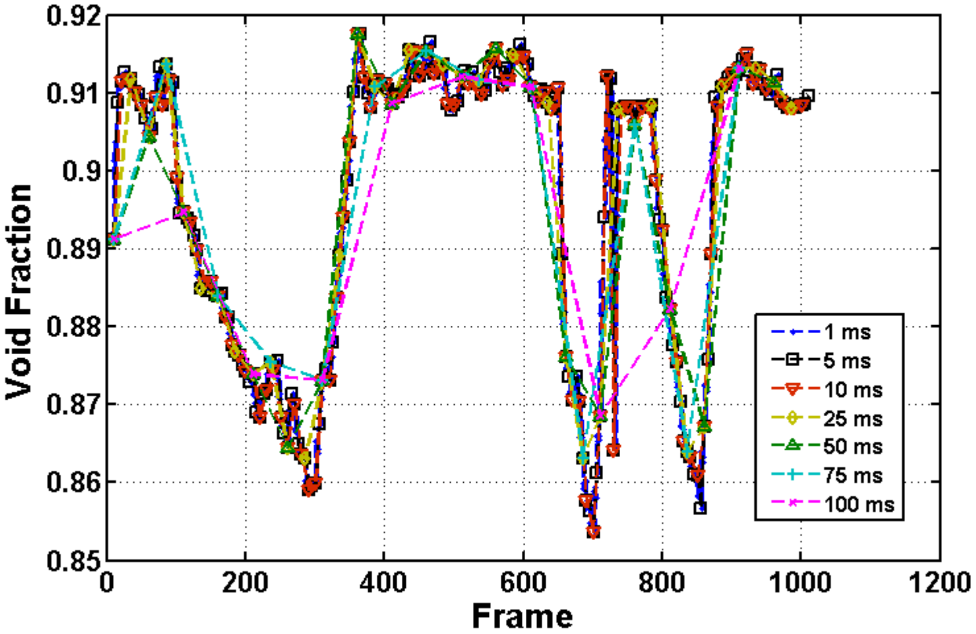

Figure 4.16: Void fraction data for a sample video captured at 20 kPa m^{-1}, containing thin film and ring film flow patterns. Data are plotted at several sample intervals.

The void fraction results were averaged over time for each of the sample intervals to quantify the effect of increased sample interval on the deviation from the true average value.

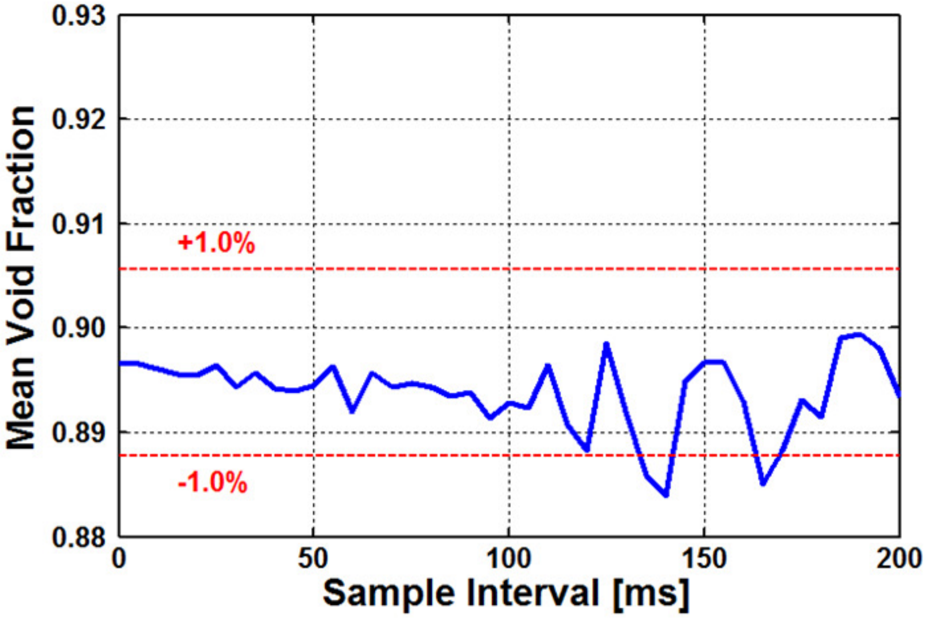

Figure 4.17: Time-averaged values of spatially-averaged void fraction for a sample video captured at 20 kPa m^{-1}. Average values remain within 1% of the true average value for all sample intervals less than 135 ms.

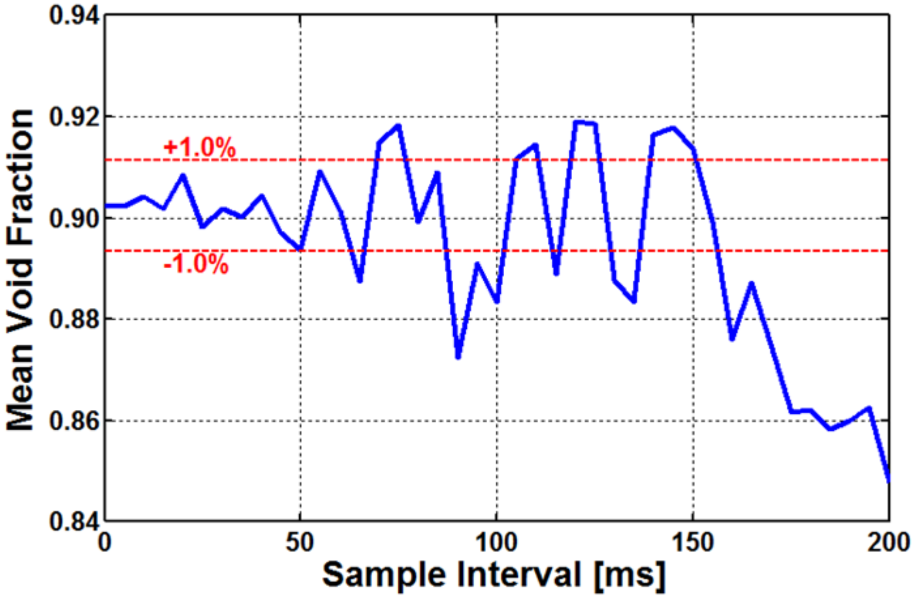

Figure 4.18: Time-averaged values of centerpoint void fraction for a sample video captured at 20 kPa m^{-1}. Average values remain within 1% of the true average value for all sample intervals less than 65 ms.

Fig. 4.17 shows that the time-averaged values of total void fraction remain within 1.0% of the true average value for sample intervals less than 135 ms. The time-averaged local centerpoint void fraction data shown in Fig. 4.18 vary much more. The time-averaged centerpoint void fraction values remain within 1.0% of the value obtained at the highest sampling frequency for sample intervals less than 65 ms. Based on this analysis, a sampling interval of 50 ms was used for all void fraction analyses, equivalent to analyzing every 50 frames at 1000 fps, or every 100 frames at 2000 fps. This sampling interval minimizes the computational time required for void fraction calculation while maintaining low uncertainty values. The resulting uncertainty due to sample interval is found to be 0.25% for the spatially averaged void fraction and 0.99% for the centerpoint void fraction.

The repeatability of the void fraction and velocity readings was also analyzed. This was accomplished by analyzing the same 10 consecutive frames for spatially averaged and centerpoint void fraction and velocity using the process described previously, and repeating this process 5 separate times. For each frame, the standard deviation over the 5 repeated analyses was determined. These values were then used to calculate the pooled standard deviation for the entire data set according to Equation (4.8), in which ν_i and σ_i represent the degrees of freedom and reading standard deviation for an individual frame.

$$\sigma_{pooled} = \sqrt{\frac{\sum \nu_i \sigma_i}{\sum \nu_i}} \tag{4.8}$$

The uncertainty due to repeatability was then calculated using equation (4.9). It is known that 99.6% of readings deviate from the mean value by less than $3\sigma_{pooled}$, effectively making this the maximum deviation. This maximum deviation is divided by the overall mean value of the measurement of interest, averaged over all frames and repetitions. The uncertainties due to repeatability for total void fraction, centerpoint void fraction, and interface velocity for the cylindrical assumption were determined to be 3.45%, 3.62%, and 4.59%, respectively.

$$U_{repeatability} = \frac{3\sigma_{pooled}}{\bar{s}} \tag{4.9}$$

The total uncertainty for void fraction measurements is calculated using equation (4.10), which accounts for contributions from repeatability and sampling frequency. The total uncertainties for the spatially averaged and centerpoint void fraction readings using the cylindrical assumption were found to be 3.46% and 3.75%, respectively.

$$U_{\alpha,combined} = \sqrt{U_{\alpha,repeatability}^{\ 2} + U_{\alpha,sensitivity}^{\ 2}} \tag{4.10}$$

The uncertainty in film thickness readings for thin film, ring film, and intermittent flows was calculated by accounting for the void fraction uncertainty and the manufacturing tolerances on the diameter of the glass microchannels (±0.0076 mm). Film thicknesses and their uncertainties were calculated with uncertainty for void fraction values from 0.1 to 1.0. These film thickness values and their uncertainties are plotted in Fig. 4.19. The average uncertainty for the values obtained in the present study was found to be 1.9 μm. A sample calculation is shown for a data point with calculated void fraction of 0.863.

$$t_{film} = \frac{D_h}{2}\left(1-\sqrt{\alpha}\right) = \frac{\left(203.0 \pm 7.6\ \mu\text{m}\right)}{2}\left(1-\sqrt{0.863 \pm 0.032}\right) = 7.22 \pm 1.78\ \mu\text{m} \tag{4.11}$$

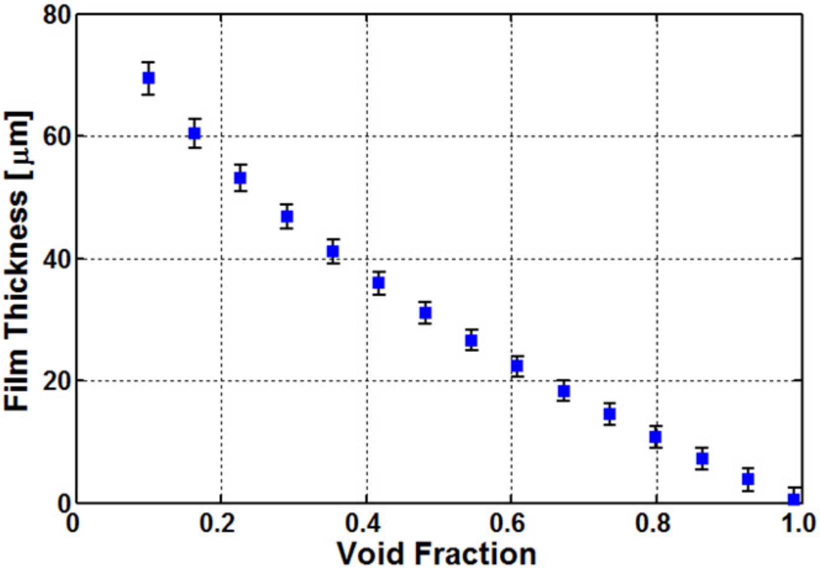

Figure 4.19: Calculated film thickness, shown with uncertainty, for sample void fractions from 0.1 to 1.0.

Because the calculation of void fraction from image data differs between cases using the cylindrical and semi-cylindrical assumptions, the above process was repeated using the semi-cylindrical assumption, which is used in rivulet flow. The uncertainties due to repeatability in spatially averaged and centerpoint void fraction measurements were found to be 4.12% and 4.51%, respectively. These values were used in the calculation shown in Equation (4.11), and the uncertainty in film thickness for rivulet flow was determined to be 2.21 μm.

The uncertainty associated with the measurement of pressure was calculated from the instrument specifications. For both the Rosemount 3051T and 2088 pressure transmitters, the uncertainty is reported by the vendor to be 0.15% of span. For the experiments performed, the span was set from 0 to 172 kPa; therefore, the absolute error was computed to be 0.26 kPa. The maximum uncertainty, computed from the minimum recorded pressure value for the experiments conducted in this study (3.65 kPa), was found to be 6.6%. However the average uncertainty in pressure readings, averaged over all pressure measurements taken, was 0.9%. The uncertainty values discussed above are summarized in Table 5.

Table 4.5: Uncertainty values for experimental variables, averaged over the entire test matrix.

Value	Thin film, ring film, & intermittent flows	Rivulet flow
$U_{sensitivity}$, Centerpoint void fraction	0.99%	
$U_{sensitivity}$, Spatially averaged void fraction	0.25%	
$U_{repeatability}$, Centerpoint void fraction	3.62%	4.51%
$U_{repeatability}$, Spatially averaged void fraction	3.45%	4.12%
Interface velocity (u_i)	±4.59%	
Pressure (P, ΔP)	±0.26 kPa	
Film thickness (t_f)	±1.9 µm	±2.2 µm

Finally, it should be noted that Kawahara *et al.* (2002) found that there is some uncertainty in the measurement of film thickness due to optical distortion from the cylindrical channel walls, but that the extent of this distortion is difficult to quantify. They attempted to correct the optical distortion, only to note that several of the films observable without correction were not observable with correction, implying that distortion has a magnifying effect in the radial direction. From this result it is possible that the film thickness results obtained in this study are artificially high, although it is difficult to quantify this difference.

4.4 Image analysis results

4.4.1 Interface velocity

Interface velocity was calculated using the method described above. In total, interface velocity was calculated for 63 data points. The reported results for interface velocity are averaged over all the observed frames in a given sample. Velocity was observed at two axial locations on each test section used to capture the acceleration and deceleration of the interface as one phase displaces another. Velocity results for the displacement of liquid by gas are shown in Fig. 4.20, and results for the displacement of gas are shown in Fig. 4.21.

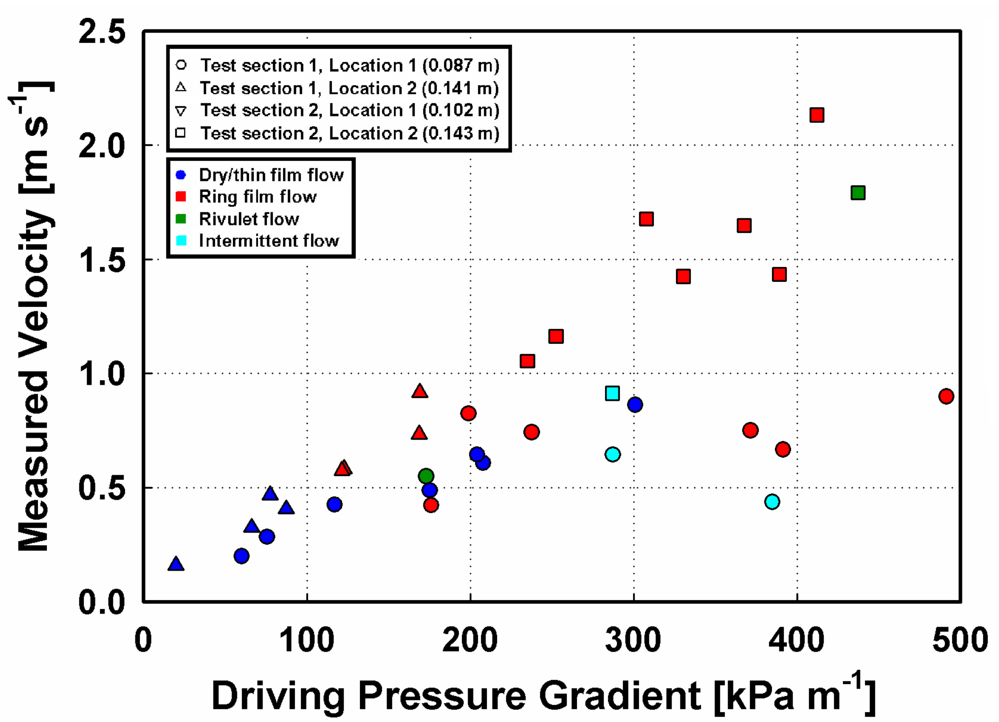

Figure 4.20: Interface velocity results for the displacement of liquid by gas.

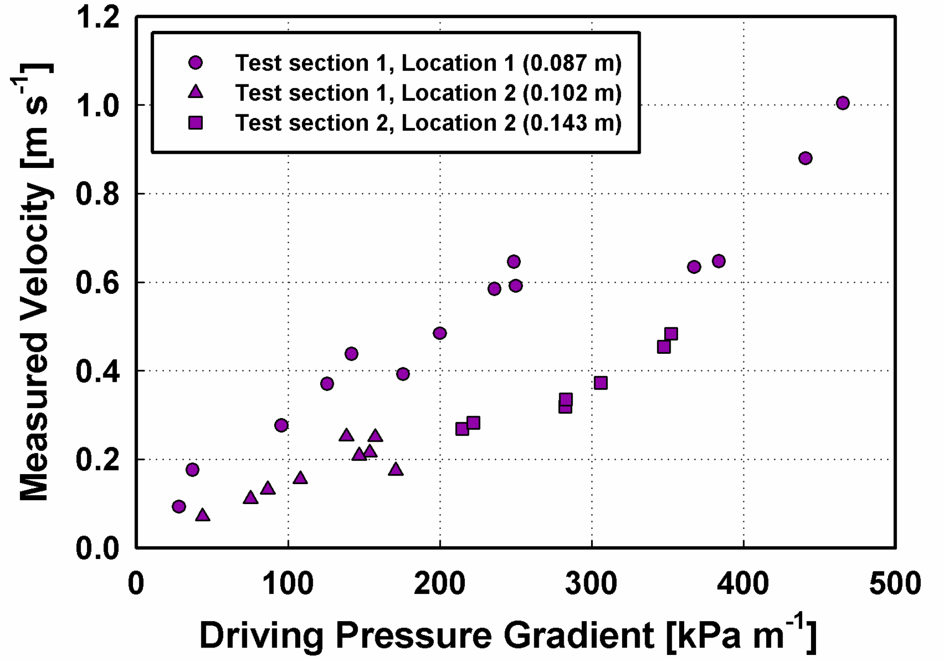

Figure 4.21: Interface velocity results for the displacement of gas with liquid. Only one flow pattern was observed for the displacement of gas by liquid.

As expected, liquid-gas interface velocity increases with driving pressure in a roughly linear fashion. The velocity of the liquid gas interface increases as liquid is removed from the channel; this is evident from the fact that in the displacement of liquid the velocities recorded at axial location 2 (approximately 45 mm further downstream in the channel) are higher than those recorded at location one. The opposite is true for the displacement of gas: as the incoming liquid occupies more of the channel length, the flow slows down due to the larger pressure gradient in the liquid region. These qualitative observations are consistent with the predictions of both the compressible and incompressible fluid flow models. More detailed comparison of the data with the modeling predictions can be found in Chapter 5.

Another observable trend is that the velocities are much more scattered for the displacement of liquid than for the displacement of gas. This is largely due to the presence of multiple flow regimes and interface behaviors during the displacement of liquid by gas. As opposed to the displacement of gas, in which the incoming liquid interface is not significantly affected by changes in velocity, the incoming gas slug displacing liquid is subject to elongation and deformation, the presence of liquid films, and in some cases, separation into separate slugs. These phenomena account for the less coherent flow velocity data for the displacement of liquid by gas.

4.4.2 Void fraction and liquid film thickness

Spatially averaged and centerpoint void fraction were calculated in the manner described previously, by performing edge-detection image analysis and subsequent geometric calculations every 50 ms for each of the 33 video samples. The results of these void fraction analyses are shown in Fig. 4.22. In addition to spatially averaged and centerpoint void fractions, the difference between these two readings was also plotted to observe the differences between the averaged values and the more spatially sensitive centerpoint measurement. Once void fraction data were obtained, the calculation from Equation (4.7) was performed for all data points and a similar series of plots was generated for the resulting liquid film thickness data. These results are shown in Figure 4.23.

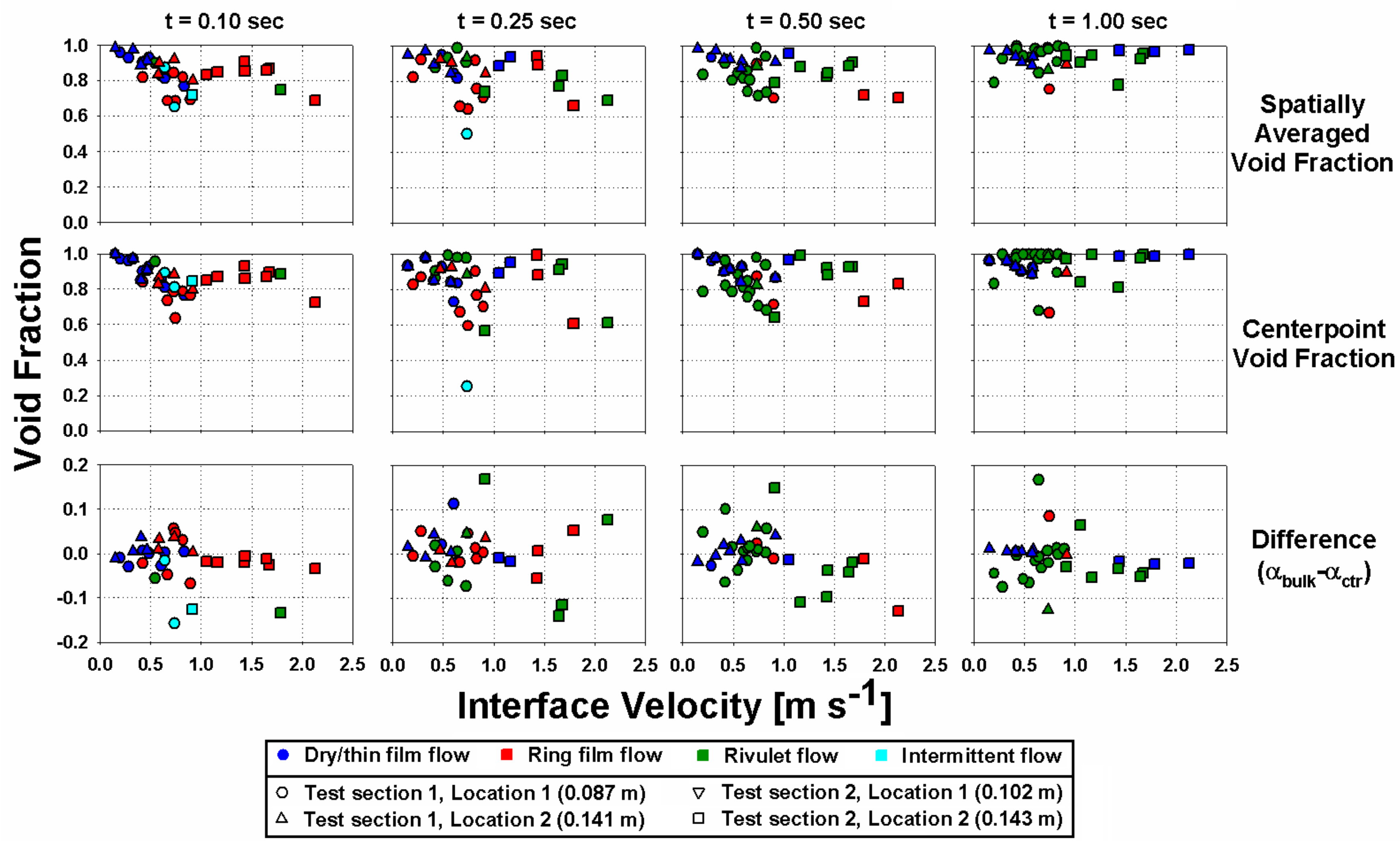

Figure 4.22: Void fraction versus interface velocity for four time steps.

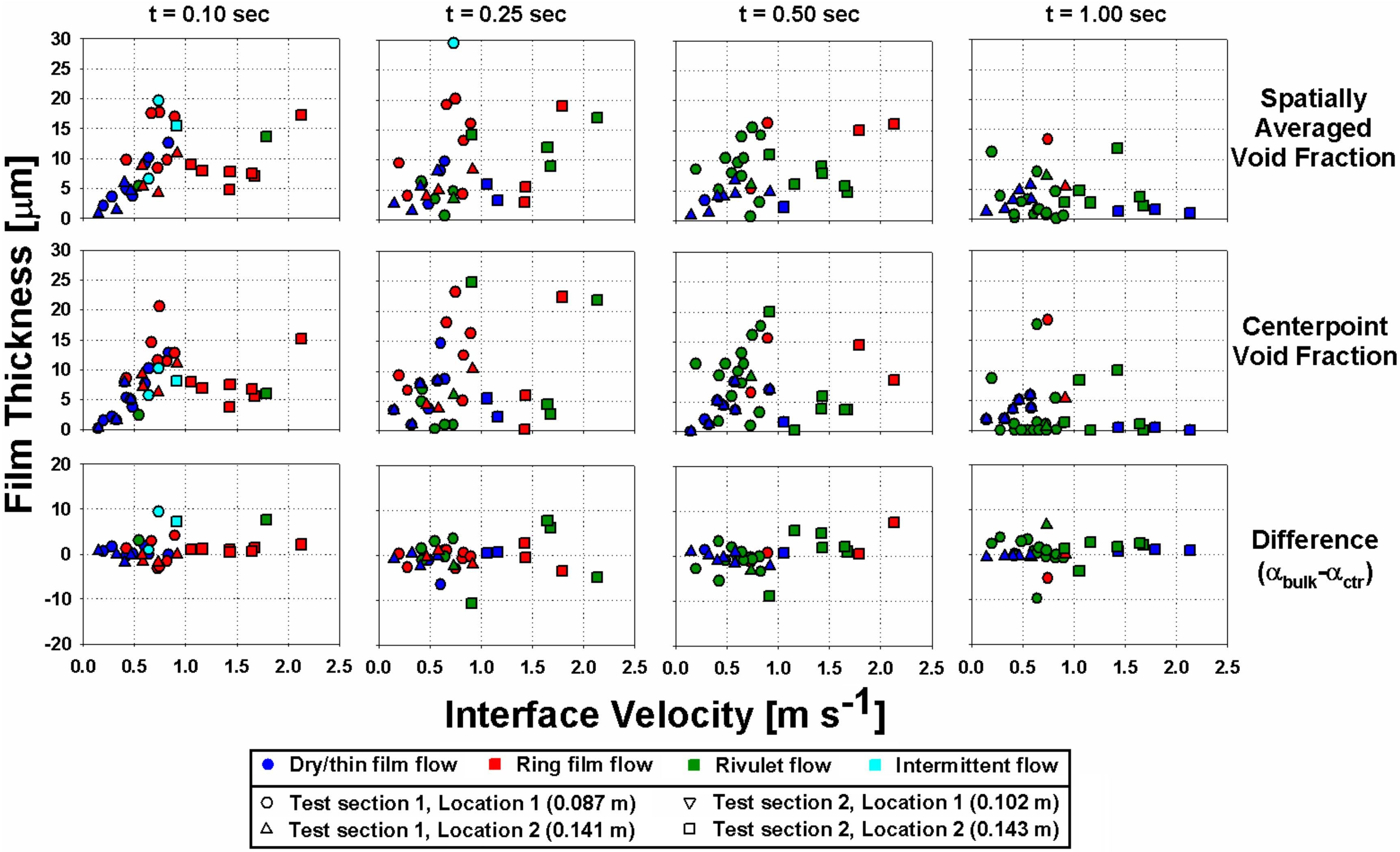

Figure 4.23: Calculated average film thickness versus interface velocity for four time steps.

Several observations can be made from the data shown in Figs. 4.22 and 4.23. As expected, the residual liquid film thickness decreases with time as gas flow continues to shear the remaining liquid down the channel. This is also consistent with the increased occurrence of rivulet flow with time; with diminished liquid supply, rivulet flow is more likely to occur. In several samples, the spatially-averaged film thickness approaches zero by the end of the 1-second observation interval, meaning that the walls are dry or nearly dry after one second of sustained gas flow down the channel. Also of interest is the fact that in many of these cases, while the spatially averaged film thickness is still slightly greater than zero, the centerpoint film thickness was measured to be zero, indicating the existence of local dry wall areas despite the presence of liquid in the channel. This serves as a quantitative indication of rivulet flow, where liquid adheres to the channel wall without continuously covering its surface.

Conversely, when the centerpoint film thickness is observed to be greater than zero and approximately equal to the spatially averaged film thickness, it is likely that a continuous and relatively smooth film exists on the channel walls. When centerpoint film thickness is observed to be larger than the spatially averaged film thickness, it can indicate either the presence of a wavy continuous film or the presence of large droplets or thick rivulets at the channel centerpoint.

The four observed cases of intermittent flow are identified in the first spatially averaged void fraction plot by the four blue points with significantly lower void fraction (and higher calculated film thickness) than the rest of the data. This plot is shown in greater detail in the calculated film thickness plot in Fig. 4.24.

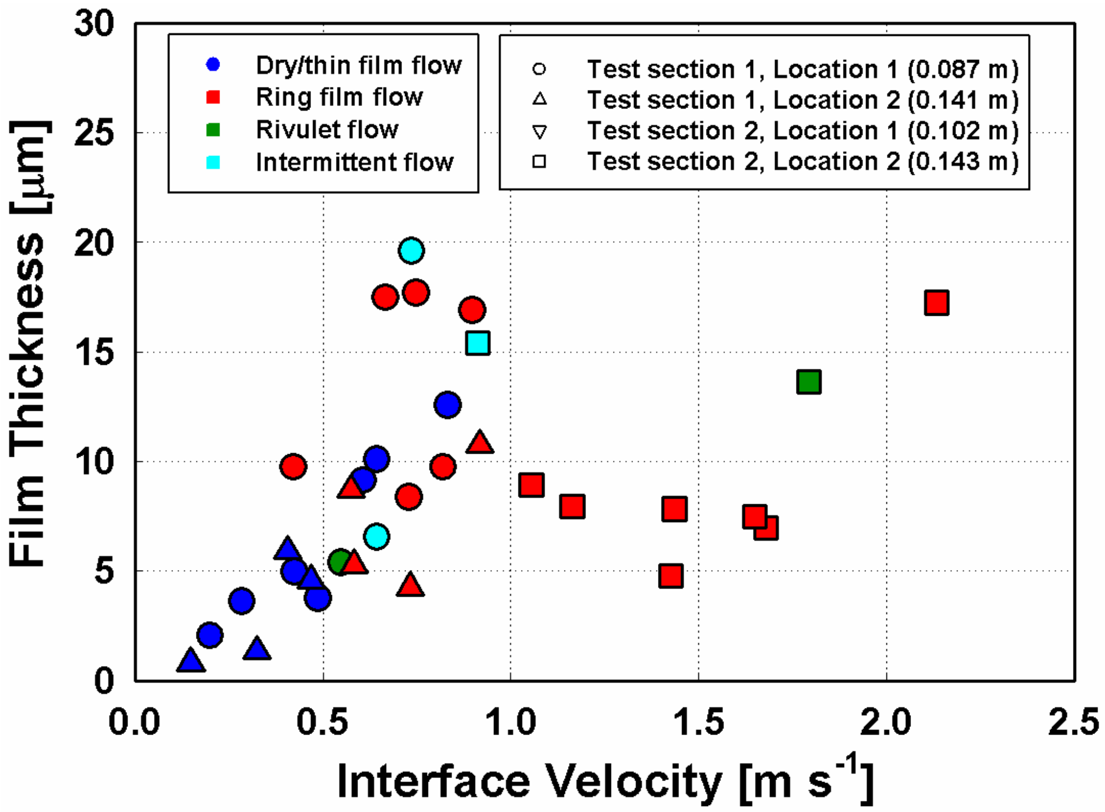

Figure 4.24: Spatially averaged film thickness versus interface velocity at 0.1 seconds after displacement. Points indicating intermittent flow are indicated by the circled region.

Also seen in Fig 4.24 is an apparent trend in the film thickness observed immediately after the displacement of liquid. Liquid film thickness increases with interface velocity until about 1.0 m s^{-1} due to the deformation of the liquid-gas interface as viscous forces become more dominant. These increased viscous forces cause the front of the bubble to elongate and become narrower, leading to a thicker liquid film between the bubble and the wall. From 1.0 m s^{-1} to approximately 1.7 m s^{-1}, the liquid film thickness appears to decrease slightly, possibly due to the fact that higher gas velocities produce more interfacial shear at the film surface, increasing the liquid flow rate within the film and reducing its thickness. From 1.7 m s^{-1} to 2.2 m s^{-1}, the measured film thickness increases again as the incoming gas-liquid interface deforms still further to resemble a thick-film annular or wavy annular flow pattern.

While these trends are qualitatively apparent in the data immediately after displacement, the data are still highly scattered, making quantitative identification of trends very difficult. The unstable and overlapping nature of flow patterns in such small channels and the highly transient nature of the liquid displacement process causes the data to become still more scattered in subsequent time steps. No discernible trends in void fraction or film thickness are visible beyond the first 100 ms after displacement occurs.

CHAPTER 5

RESULTS AND DISCUSSION

5.1 Model validation

The compressible fluid flow model described in Chapter 3 was modified for application to the experimental conditions. The validity of the model was assessed using the channel dimensions, pressures, and fluid temperature recorded during the experiments and comparing the model predictions with the experimental results. The first key parameters used for accurate simulation of the experimental conditions are the dimensions of the test sections. The test sections were fabricated using channels with inner diameters of 203 μm. Due to problems with test section breakage and optical obstruction, two different test sections were used for the experiments. In each of these test sections, the flow phenomena were observed at two separate axial locations to more accurately record the acceleration and deceleration of the liquid-gas interface. The test section lengths and observation locations are shown in Table 5.1. Air and water properties for simulation were calculated at 25°C, and the channel inlet and outlet pressures used were those recorded at the time of measurement.

Table 5.1: Test section dimensions and observation locations.

Test Section	L_{total} (mm)	L_1 (mm)	L_2 (mm)
#1	178.0	87.4	140.5
#2	184.0	102.0	143.6

The displacement of gas by liquid and the displacement of liquid by gas were simulated for each of the experimental conditions recorded. Figures 5.1 and 5.2 show the modeling results plotted against the experimental results for comparison.

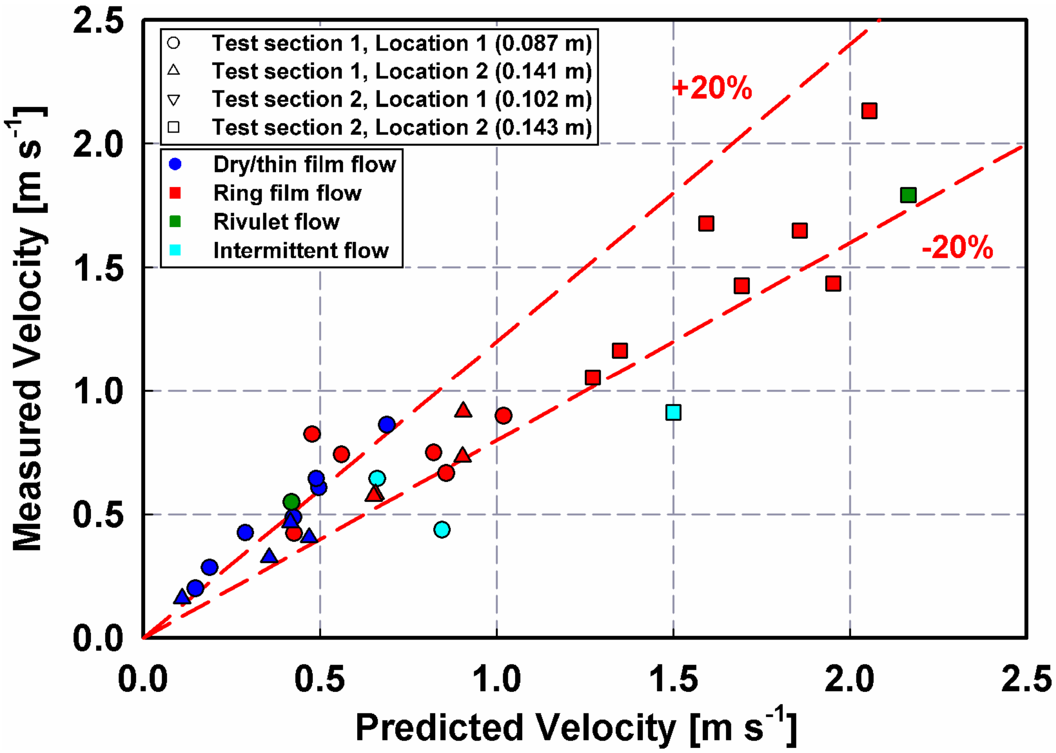

Figure 5.1: Comparison of model predictions with experimental results for the displacement of gas by liquid.

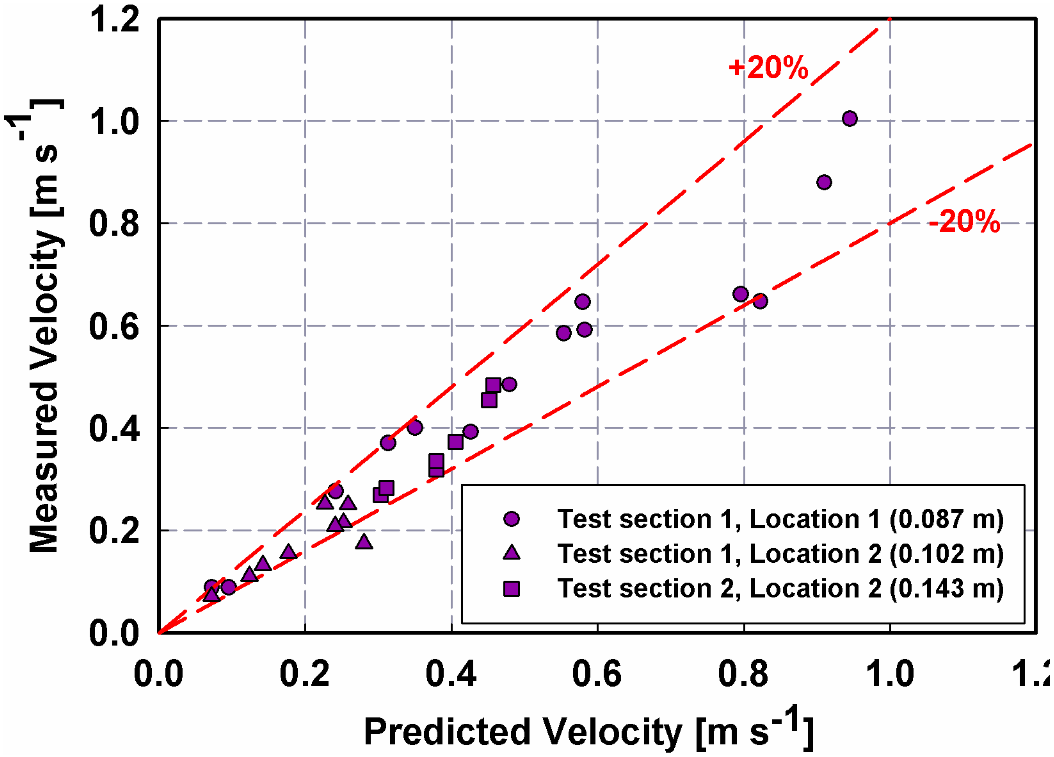

Figure 5.2: Comparison of model predictions with experimental results for the displacement of liquid by gas.

Good agreement was found between the model and the experiments for the displacement of gas by liquid, shown in Fig. 5.1. In this data set, 90% of the data points are within 20% of the predicted values. The mean and median average error values were 3.4% and 5.2%, and absolute error percentages were found to be 11% and 10%, respectively.

Agreement between the model and experiments for the displacement of liquid by gas was not as close as that of the displacement of gas by liquid, as shown in Fig. 5.2. In this data set, only 64% of the points are within 20% of the predicted values, and the mean and median average error values were found to be 4.6% and 2.9%. Mean and median absolute error values were 20% and 15%, respectively. The errors for both data sets are summarized in Table 5.2.

Table 5.2: Results from model validation comparisons.

Case	Error	Average	Absolute
Displacement of gas by liquid	Mean	3.4%	11%
	Median	5.2%	10%
	Within 20%	90%	
Displacement of liquid by gas	Mean	4.6%	20%
	Median	2.9%	15%
	Within 20%	64%	

Model agreement was much better for the displacement of gas by liquid, due in a large part to the highly predictable behavior of the liquid-gas interface during displacement. The gas was displaced from the channel by a continuous slug of liquid, regardless of the driving flow conditions, implying that the piston-displacement assumption (no mixing at the interface) used for bulk fluid modeling was representative of the actual flow behavior. In the displacement of liquid by gas, the interface behavior varied significantly across the range of driving flow conditions, reflected in the high degree of scatter in the film thickness and velocity data.

5.2 Flow pattern and film thickness

With a few exceptions, the flow pattern data showed agreement with several of the trends and phenomena described in microchannel flow literature. At low interface velocities (0 to 0.25 m s^{-1}), incoming gas bubbles often appeared to have dry wall contact. This was consistent with the observations of Serizawa *et al.* (2002) for air-water flow in 100 μm tubes. However, at slightly higher velocities (≥0.3 m s^{-1}), it was clear that the nose of the incoming gas slug was significantly deformed, and visible liquid films were seen between the incoming gas and the channel wall. Figure 5.3 shows sample images of slugs with and without dry walls. This agrees with the results presented by Serizawa *et al.* (2002), who reported the existence of dry wall area within long gas bubbles at low velocity, but the formation of films between gas bubbles and the channel wall for clean channel surfaces at higher velocities. While Serizawa *et al.* noted the formation of these films only at very high superficial gas velocities and carefully maintained surface conditions, this apparent disagreement may be attributed to the larger channel diameter used in this study, which would decrease the confinement and rigidity of the incoming gas bubble, allowing it to be more easily deformed. It is apparent from this result that for air and water, 200 μm channels display a mix of characteristics noted in studies of both smaller and larger channels, with surface tension forces having a strong influence on flow behavior, though not as strong as those observed in channels from 25 to 100 μm in diameter.

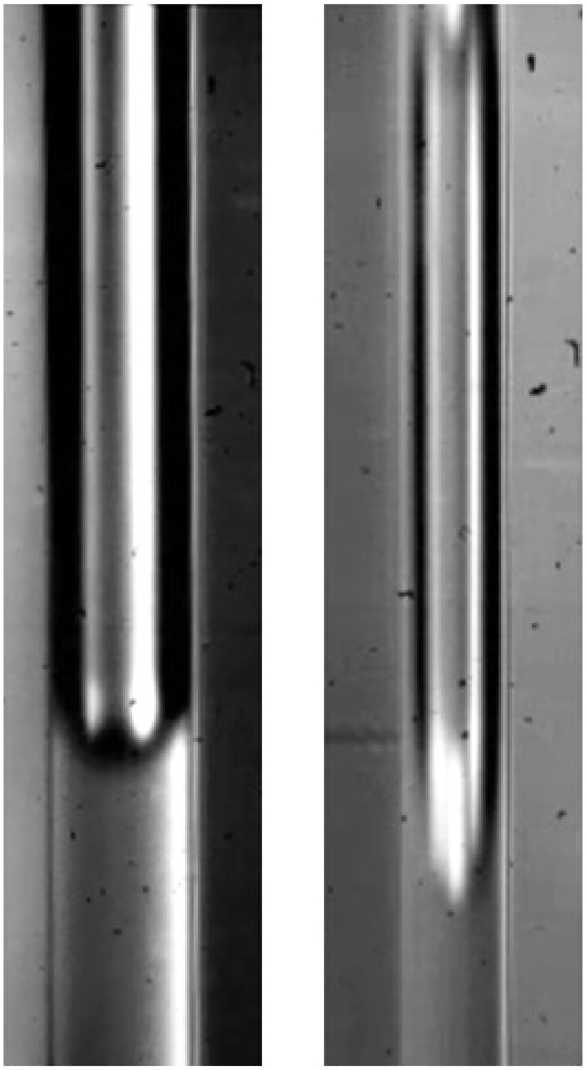

Figure 5.3: Incoming gas slugs with dry walls (left) and with surrounding liquid film (right) during displacement of liquid. The dry slug sample was captured at a velocity of 0.16 m s^{-1} and the film sample was captured at a velocity of 1.79 m s^{-1}.

The liquid ring flow pattern, in which a continuous film of liquid accumulates on the walls in thick symmetrical rings, was often observed at higher gas velocities ($\geq$ 0.4 m s^{-1}). However, while Serizawa *et al.* (2002) observed that the liquid ring flow pattern was relatively stable, the flow pattern in this study was frequently observed alternating back and forth between rivulet and liquid ring flow. This key difference is probably due to the transient nature of the displacement process, which effectively causes an unsteady liquid supply upstream as the remaining liquid in the channel is forced downstream by interfacial shear from the gas. On the other hand, this rapid alternation between flow regimes is consistent with the findings of Kawahara *et al.* (2002), who formulated probabilistic flow regime definitions because flow pattern instability made the use of more conventional flow pattern definitions less meaningful.

The flow pattern designated as "liquid lump flow" by Serizawa *et al.* (2002) is virtually indistinguishable from the rivulet flow pattern observed in this study and that in Barajas and Panton (1993). Barajas and Panton even note that the liquid lumps are connected to films "just like rivulets". Similar to both of these studies, in the present study this flow pattern occurred at high gas flow rates and featured partially-continuous liquid films being driven down the channel by the flow of gas. High interfacial shear and wall-liquid interactions prevented the formation of a fully continuous liquid film. The liquid rivulets typically accumulated into larger droplets on the walls in a manner similar to that of liquid ring flow, with the rivulet film serving as the liquid supply. Transition to rivulet flow occurred at much lower gas velocities than reported in either Serizawa *et al.* (2002) or Barajas and Panton (1993), both of which observed the rivulet flow transition at superficial gas velocities ≥ 10 m s^{-1}. This apparent difference is probably due to the fact that in the present study, the liquid supply was not replenished, making continuous films more difficult to sustain the longer the gas flow continues. The minimum superficial liquid velocity observed in either Serizawa *et al.* or Barajas and Panton was around 0.1 m s^{-1}, which was still sufficient to maintain a continuous liquid film for gas velocities up to approximately 10 m s^{-1}. The scenario investigated in the present study represents the limit in which the liquid superficial velocity approaches zero; reduction of the liquid superficial velocity below 0.1 m s^{-1} would probably have produced rivulet flow at lower gas velocities. This is supported by the fact that the rivulet flow transition line plotted by Barajas and Panton does not occur at a constant gas flow rate.

Bubbly flow, or the existence of small bubbles with effective diameters much smaller than the channel diameter, was never observed in the present study. This result disagrees with Serizawa *et al.* (2002) but is consistent with the findings of Kawahara *et al.* (2002), who noted that the laminarizing effect of channels on the order of 100 μm tends to suppress the turbulent breakup of larger bubbles; at the highest interface velocity recorded in this study the liquid Reynolds number was only about 400, indicating that the flow was laminar. It is also worth noting that many of the bubbles classified as examples of bubbly flow by Serizawa *et al.* have diameters close to the channel diameter, and could be considered as short-aspect-ratio slug bubbles.

The film thickness data obtained from image analysis of the initial displacement and subsequent liquid-gas interactions showed considerable fluctuation. As was shown in Figure 4.19 in the previous chapter, the data for every point in time was highly scattered, and beyond the initial displacement, no patterns were discernible. The plot of initial film thickness is shown again in Fig. 5.4.

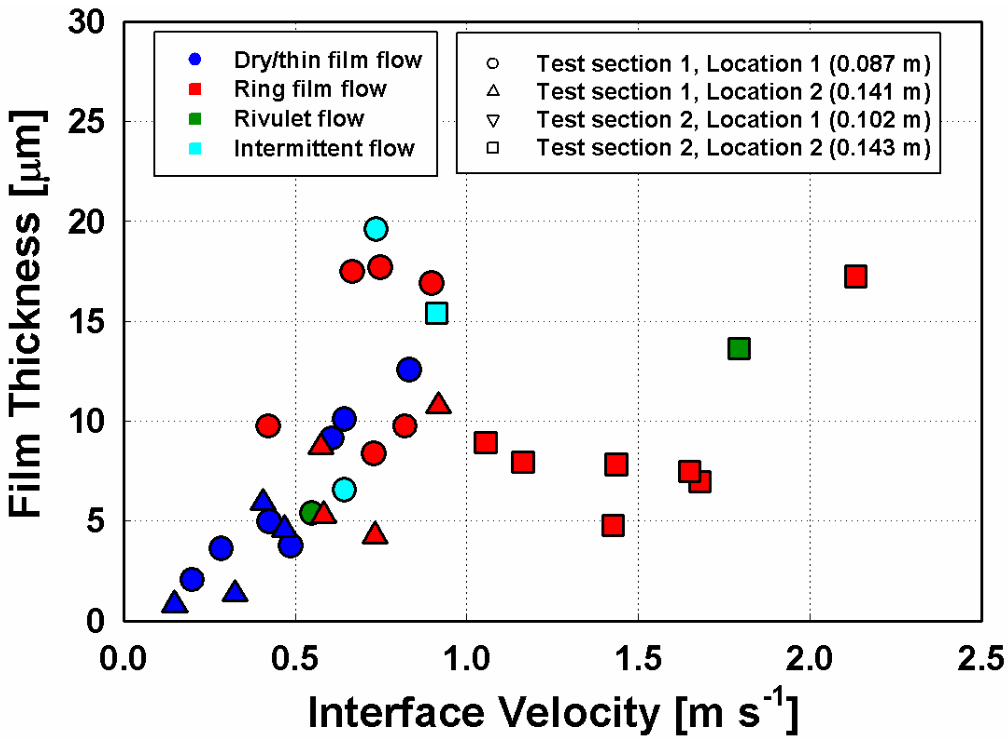

Figure 5.4: Spatially-averaged liquid film thickness on the channel walls, recorded immediately after initial displacement.

Excluding the points corresponding to intermittent flow, the initial film thickness data appear to follow an approximate trend with a local maximum at about 0.9 m s^{-1} and a local minimum at 1.5 m s^{-1}, although the data are still scattered, especially between velocities of 0.25 and 0.75 m s^{-1}. Satisfactory explanations for these trends could not be found in the present study. Therefore, correlating expressions for film thickness based on dimensionless groups such as the capillary number (the ratio of viscous forces to surface tension forces) and the Weber number (the ratio of inertial forces to surface tension forces could not be developed in the present study.

The film thickness results shown in Figure 5.4 are in apparent qualitative disagreement with the film thickness results observed by Fukano and Kariyasaki (1993), who observed thicknesses of liquid films surrounding gas slugs in horizontal air-water flow in tubes from 1 to 9 mm. These results are shown in Fig. 5.5.

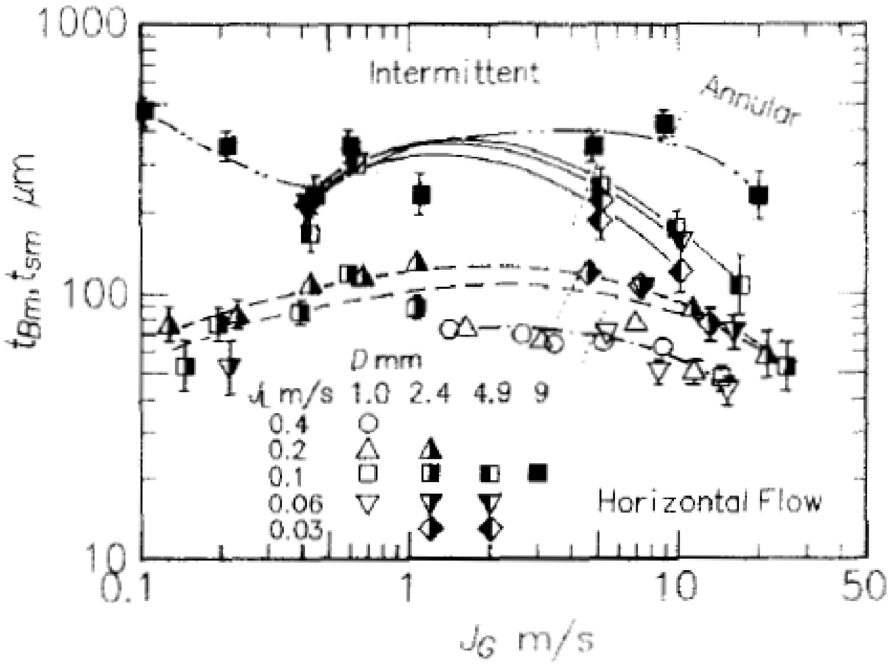

Figure 5.5: Film thickness results from Fukano and Kariyasaki (1993) (reproduced with permission).

The differences between the results of the present study and those of Fukano and Kariyasaki (1993) can be explained by the differences in tube size, the horizontal flow orientation, and the fully mixed, simultaneously supplied flow configuration. For example, while their 9 mm diameter tube results exhibit an approximately opposite trend in film thickness in comparison to those from the present study, this apparent discrepancy can be explained by the effects of flow stratification on the elongated gas bubbles in the channel. In the 9 mm diameter tube, they found the film thickness initially decreased with increased gas flow rate because of the increase in bubble diameter with increased gas flow rate in horizontal flow. However in 200 μm channels, gas bubbles are known to occupy nearly the entire channel diameter at all conditions, and an increase in gas flow rate causes deformation of the nose of the bubble, which in turn allows for thicker films between the bubble and the wall.

In the smaller diameter tubes (1.0 mm and 2.4 mm), they found film thickness to decrease in the annular regime as a result of increased interfacial shear between the liquid and gas, causing a reduction in film thickness as liquid velocity in the film was increased. An approximately opposite trend can be observed in Fig 5.4, in which liquid films are found to be thicker at higher velocities. This is attributable to the differences in flow configuration and the mechanisms at work in these two cases. Whereas the transition to annular flow in 1.0 mm and 2.4 mm tubes occurs as bubbles elongate and coalesce to form a continuous gas core, in the displacement flow configuration, the incoming gas bubble nose elongates without the possibility of coalescing with another bubble downstream, essentially piercing through the liquid and leading to thick films around the edges of the incoming gas bubble. From the film thickness results shown in Fig. 5.4, as well as from the heat and mass transfer modeling results shown in Chapter 2 (reproduced in Fig. 5.6), it appears that for overall process modeling, the correlation of film thickness data for use in coupled displacement and mass transfer modeling may not be particularly important, because continuous liquid films as thin as 1 μm are thick enough to seriously impede mass transfer.

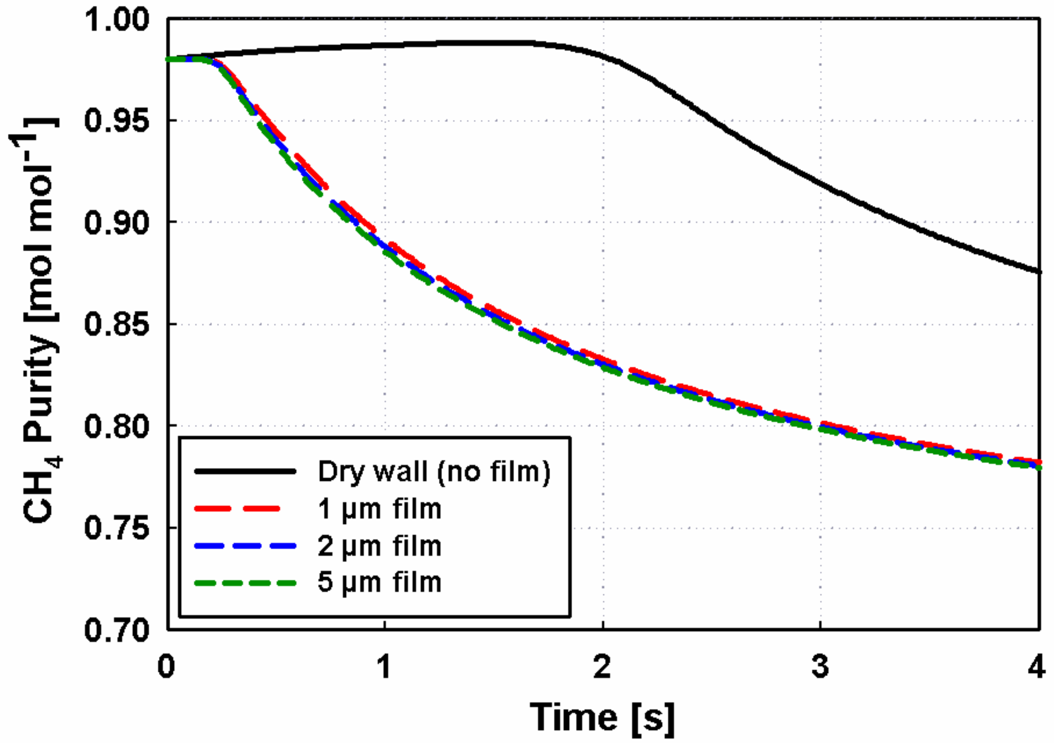

Figure 5.6: Channel output purity vs. time for several simulated liquid film thickness values.

As demonstrated by the modeling results in Fig. 5.6, the presence of any continuous liquid films will seriously impair the ability of the system to purify methane. Referring once again to the data in Fig. 5.4, film thickness was found to be as high as 19 µm in the first 0.1 seconds following displacement (and as high as 25 to 30 µm in the first 0.25 seconds following displacement). While the results of Serizawa *et al.* (2002) indicate that it may be possible to maintain a dry channel wall at very low velocities, in the present study it was found that to maintain a residual film thickness of less than 1 µm, the interface velocity during displacement should not exceed 0.16 m s^{-1}. This means that, at a minimum, the displacement of liquid from a 1-meter channel would take 6.25 seconds. This restriction on interface velocity may represent a penalty on process time and overall output (full process modeling is needed to comprehensively evaluate these effects), and would also require precise control of driving pressure at the channel inlet. In addition, given the rapidly fluctuating flow pattern behavior noted in this study, manufacturing tolerances on channel diameter or variations in surface characteristics across the entire microchannel monolith should be carefully controlled, because they could significantly affect both interface velocities and displacement times.

A useful alternative to this slow displacement process could be the incorporation of an extra process step for the purging of residual liquid from the channel. As discussed in the literature review, similar process steps are often incorporated in PSA systems to increase the overall recovery of adsorption processes (Cen *et al.*, 1985; Kapoor and Yang, 1989; Olajossy *et al.*, 2003). A purge step in this case could consist of displacement of liquid by gas using purified methane captured from other channel monoliths operating out of phase with one another. Instead of displacing the liquid in the channel with the contaminated feed gas, the initial displacement would be achieved using the flow of purified methane. This flow of methane would be continued so that the remaining liquid on the channel walls could be driven down the channel and removed, at which point the flow of feed gas would begin. This process would preserve the mass transfer performance of the channel during the adsorption step, and because the purge gas used is purified methane, it can be captured at the channel outlet along with the newly purified methane, either for storage or for use in other purge phases.

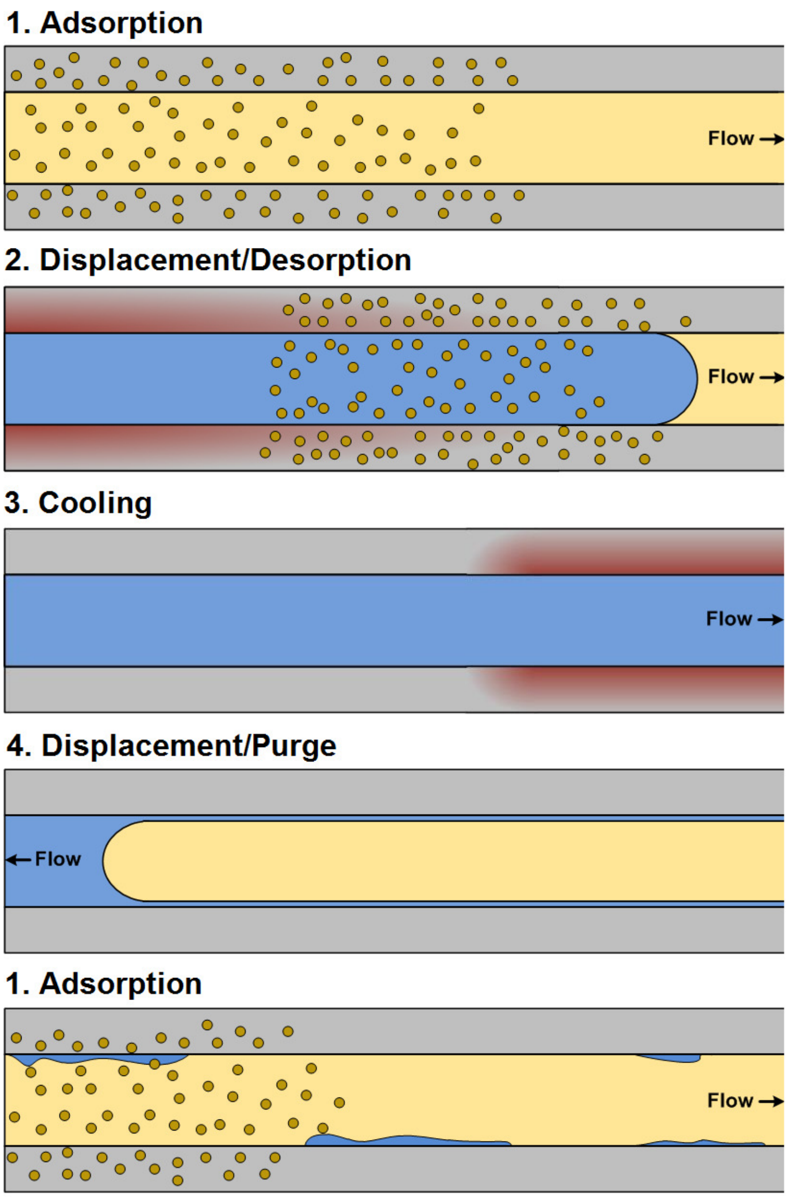

1. Adsorption

2. Displacement/Desorption

3. Cooling

4. Displacement/Purge

1. Adsorption

Figure 5.7: Schematic of a microchannel adsorption process with a countercurrent purge step.

It is important to note that a purge step such as the one described above may not need to completely remove all the liquid from the channel to preserve the mass transfer performance of the system. As discussed in Chapter 4, the achievement of a rivulet flow regime may be sufficient to reduce the mass transfer resistance in the channel to acceptable levels. Because significant portions of dry wall exist in rivulet flow, the mass transfer resistance in the liquid-covered portion of the wall is placed in parallel to that of the dry wall, decreasing overall mass transfer resistance relative to the case of complete wall coverage by liquid. An example of this case is shown in Figure 5.8. The heat and mass transfer models discussed in Chapter 3 were modified to simulate the existence of a channel wall with a surface area partially covered by a liquid film assumed to be 10 μm thick (based on the observed film thicknesses). Results are shown for the dry wall, a continuous 5 μm film, and 10 μm rivulets assumed to cover 50% and 25% of the channel wall surface, respectively. Resistances for the rivulet cases were computed according to the Equation (5.1) below. Representative values for the wet, dry, and total resistances in each of these cases are shown in Table 5.3, along with the corresponding mass transfer rates. Mass transfer rates were calculated assuming a driving concentration difference of 620 mol m^{-3}, which is the difference between the CO_2 concentrations in the feed and the wall at the beginning of the process.

$$\begin{gathered} R_{wet} = \frac{1}{h_m A_{wet}} + \frac{\delta_{film}}{D_{H_2O} A_{wet}} + \frac{\delta_{wall}}{D_{wall} A_{wet}} \\ R_{dry} = \frac{1}{h_m A_{dry}} + \frac{\delta_{wall}}{D_{wall} A_{dry}} \\ R_{eq} = \left(\frac{1}{R_{dry}} + \frac{1}{R_{wet}} \right)^{-1} \end{gathered} \tag{5.1}$$

Table 5.3: Sample resistance calculations for the three cases shown in Figure 5.8.

	5 μm continuous film	10 μm rivulet (25% coverage)	10 μm rivulet (50% coverage)
R_{wet} (s m^{-3})	1.18×10^{11}	4.7×10^{11}	2.35×10^{11}
R_{dry} (s m^{-3})	n/a	3.62×10^{10}	5.43×10^{10}
R_{eq} (s m^{-3})	1.18×10^{11}	3.36×10^{10}	4.41×10^{10}
$\dot{m}$ (mol s^{-1})	1.05×10^{-4}	3.69×10^{-4}	2.81×10^{-4}

Calculation Parameters			
h_m (m s^{-1})	4.1×10^{-3}	D_{wall} (m^2 s^{-1})	8.21×10^{-8}
D_{H_2O} (kg s^{-1})	1.76×10^{-9}	δ_{wall} (m)	50×10^{-6}
Δc (mol m^{-3})	620	D_h (m)	200×10^{-6}
L (m)	1.0		

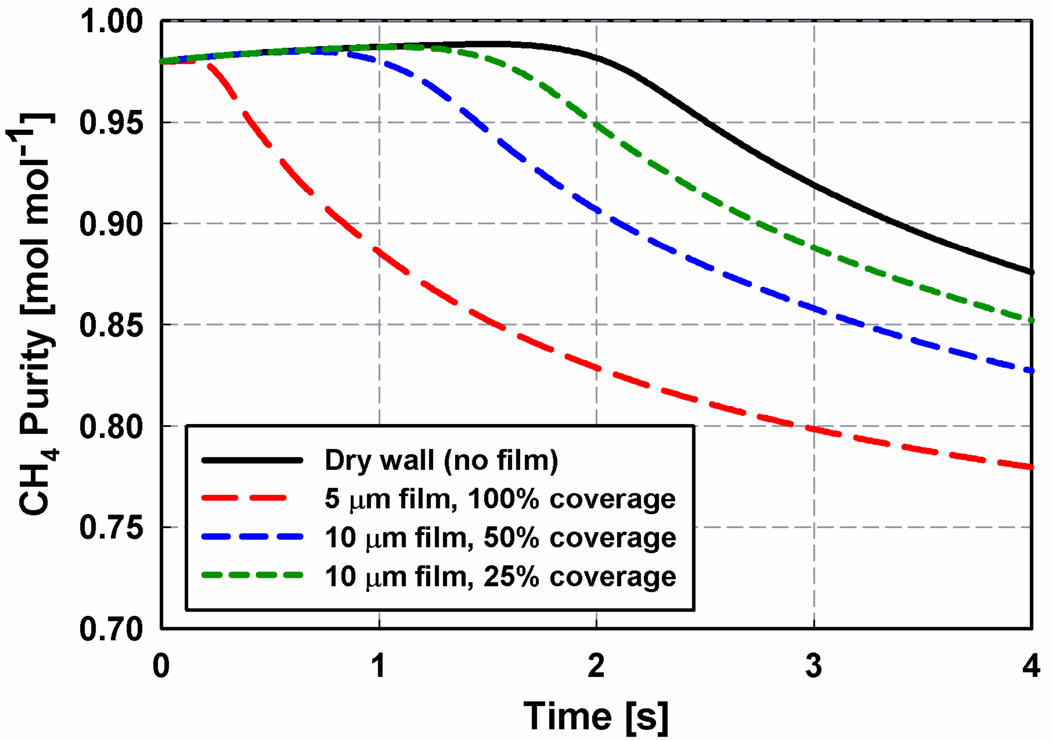

Figure 5.8: Outlet methane purity vs time for a dry wall, a 5 μm continuous film, and 10 μm thick rivulets assumed to cover 50% and 25% of the channel wall surface.

Figure 5.8 clearly shows that the existence of rivulets on the channel walls is preferable to the existence of continuous annular films. While the methane purity drops almost instantaneously in the presence of a continuous 5 μm film, the existence of liquid rivulets on the channel walls results in a comparatively small penalty in mass transfer performance. In the case of the rivulet covering 25% of the channel surface area, the methane purity remains in excess of 95% for 1.99 seconds, a 20% reduction in comparison to the dry wall simulation, which is still in excess of 98% at this time. In the case of the rivulet covering 50% of the wall, 95% purity is maintained for 1.45 seconds, a 42% reduction compared to the dry wall simulation. Furthermore, the comparatively low resistance for diffusion into the wall governs the calculation in Equation (5.1), making the mass transfer performance relatively insensitive to the thickness of a rivulet. As long as the purge step leaves a significant portion of area dry, acceptable mass transfer performance may be maintained.

The literature on microchannel flow patterns and surface-liquid interactions in multiphase flow indicates that creation of rivulets in the channel will be strongly dependent on the specific surface properties and geometry of the channel. Thus, the specifics of a liquid purge step (time required, gas flow rate, driving pressure, etc.) should be determined using actual adsorbent-coated channels, and several important issues must be investigated on channel monolith prototypes to find optimal conditions for a liquid purge. One such issue is the strength of the polymer-wall adhesion, and the maximum fluid flow rates that can be accommodated without shearing the adsorbent layer off the monolith walls. Another key issue to consider is whether precise control of fluid velocity is necessary or possible, or if it is sufficient to simply force purge gas through the channel as quickly as possible to decrease displacement time and increase interfacial shear for clearing the channel.

While these issues must be investigated on actual adsorbent channels, the results of this study and the survey of the literature provide several valuable insights into the creation of rivulet flow in the channel. For one, the results from Chung *et al.* (2004) indicate that increased capillary forces in the corners of the square channels will tend to draw liquid there, aiding in the disruption of continuous liquid films, providing dry wall area. The results reported by Barajas and Panton (1993) indicate that the use of hydrophobic polymers or surface imperfections, such as zeolite particles protruding from the polymer layer, will similarly aid in the breakup of continuous films into rivulets. The flow pattern observation results from this study indicate that relatively high gas velocities (≥ 1.5 m s^{-1}) facilitate the transition from annular-type flows, such as liquid ring or smooth film flow, to rivulet flow once the liquid supply on the channel walls is sufficiently diminished.

CHAPTER 6

CONCLUSIONS AND RECOMMENDATIONS

6.1 Conclusions

A study of two-phase displacement flow in a microchannel temperature swing adsorption system was performed. A model for bulk fluid displacement in 200 μm channels was developed using a one-dimensional dynamically meshed domain in which equations for momentum and species conservation were solved along with the fluid property calculations to determine the location and velocity of the liquid-gas interface during the displacement processes. This model was validated using data from an air-water flow visualization study performed on glass microchannel test sections with a hydraulic diameter of 203 μm. High-speed video recording was used to observe displacement samples at two separate channel locations for both the displacement of gas and liquid, and for driving pressure gradients from 19 to 450 kPa m^{-1}; a total of 63 samples. Interface velocities, void fractions, and film thicknesses were determined using image analysis software that detected the liquid-gas interface locations based on the Canny edge detection algorithm.

The bulk fluid displacement models for fluid velocity were found to be in good agreement with experimental results for the displacement of gas by liquid, with a mean and median error of 11% and 10%, respectively. For this displacement case, 90% of the predicted interface velocities were within 20% of the experimentally observed values. For the displacement of liquid by gas, the model error values were higher, with mean and median errors of 20% and 15%, respectively. In this case, only 64% of the predicted points were within 20% of the experimental values. This decrease in model accuracy for the displacement of liquid is attributed to liquid-gas interface deformation and the presence of several different flow patterns at the liquid-gas interface.

The flow patterns observed in the displacement of liquid by gas were dry wall, thin film, ring film, intermittent, and rivulet flows. In the displacement of gas by liquid, only one flow pattern was observed, in which a single liquid slug cleanly displaced the gas in the channel with little interaction at the liquid-gas interface. For each sample, spatially-averaged and centerpoint liquid film thicknesses were measured at 50 millisecond intervals over a 1 second time interval following displacement. Liquid film behavior was found to fluctuate rapidly due to the transient nature of the displacement process, with the incoming gas bubble deforming significantly at higher velocities and the upstream liquid supply being constantly diminished as gas flow sheared liquid films down the channel. Liquid films were observed with thicknesses as large as 30 μm. Film thickness data was highly scattered, and no systematic patterns or trends in the thicknesses were discernible beyond initial displacement. Immediately after displacement (up to 0.1 sec), the film thickness data were more coherent, but were not amenable to correlation based on dimensionless parameters. It was found that in order to ensure a dry channel wall after displacement, which would provide optimal conditions for system mass transfer, the maximum allowable interface velocity would be relatively low, 0.16 m s^{-1}.

A coupled 2-D heat and mass transfer model was devised for simulation of the adsorption process in an adsorbent-laden microchannel 1.0 meter in length. This model was used to evaluate the impact of residual liquid films on system mass transfer during the adsorption process. Continuous annular liquid films thicker than 1 μm were found to have a significant detrimental impact on system mass transfer, decreasing the mass of purified methane (considered to be in excess of 95% on a molar basis) by more than 80%. Mass transfer in the presence of non-continuous rivulet films was simulated using an approach that treated the mass transfer resistances of the wet and dry portions of the wall as resistances in series. It was determined that the presence of liquid rivulets on the channel wall is highly preferable to the presence of continuous films, and that in the case of rivulet flow, mass transfer performance is less sensitive to film thickness. From heat and mass transfer model predictions, it was determined that rivulet flow will preserve the mass transfer performance of the channel even in the presence of large amounts of residual liquid, with a 10 μm film covering 25% of the channel causing only a 20% reduction in the mass of purified methane. This is in contrast to the 5 μm continuous film, which decreases the mass of purified methane by nearly 85%.

It was determined that an additional process step for the purge of liquid from the channel could benefit overall system operation. This purge phase will remove significant amounts of residual liquid from the channel and by causing the onset of rivulet flow in the channel. The existence of dry wall area, which is characteristic of rivulet flow, improves system mass transfer performance in the presence of residual liquid.

6.2 Recommendations

As discussed in Chapter 5, the determination of the specific parameters of the recommended purge phase requires further experiments that must be performed on actual adsorbent channel monolith prototypes. These experimental investigations will be crucial to the optimization of system performance. These experiments will also be necessary to determine the effects of channel geometry and surface characteristics on displacement and liquid purging, the effects of flow maldistribution due to manufacturing tolerances and defects, and the fluid velocity limitations imposed by polymer adhesion to the monolith wall.

In addition, the actual heat and mass transfer performance of the adsorbent-laden channels should be investigated experimentally for the purpose of heat and mass transfer model validation, and the refinement of process modeling efforts. Fully-coupled models for heat, mass, and momentum transfer are currently being developed, and future work should include the time-coupling of the adsorption, desorption, displacement, and purge processes. The ultimate goal of this modeling effort is the determination of cyclic steady-state performance of the microchannel TSA gas separation system.

Further investigation into mixed-matrix (polymer-zeolite) materials and fabrication technology is needed for the successful realization of the microchannel TSA process. While adsorbent-laden channels currently exist for use in PSA and prototype TSA systems, none of these systems have had to contend with the difficulties associated with exposing the strongly hydrophilic adsorbent materials to water. Because the adsorbent materials used for the separation of CO_2 and H_2S from the methane feed mixture also strongly adsorb H_2O, the incorporation of these molecular sieve materials into strongly hydrophobic polymer materials is necessary for the viability of the process. With current hollow fiber fabrication technology, the waterproofing of the adsorbent layer remains a challenge, and the zeolites strongly adsorb and hold water once exposed to it, effectively reducing the capacity of the adsorbent in subsequent cycles. The resolution of these fabrication and material issues are critical to the viability of the microchannel TSA process.

Finally, the literature on flow pattern and film thickness in microchannels in the range of 200 μm is limited, and the few available studies can either be conflicting or difficult to interpret due to the lack of uniformity in flow pattern nomenclature and regime definitions. More studies concerning multiphase flow patterns and films in channels between 25 and 250 μm diameter would improve the understanding of the findings of this study, and would serve to resolve or explain the apparent disagreements with the information in the existing literature. Furthermore, few studies have investigated transient phenomena in multiphase flow in microchannels, and none address the sequential displacement of one phase with another. Further work in these areas would be valuable, both for validation of the results presented here and for the further development of microchannel TSA systems in the case that the present gas separation concept achieves large-scale use.

APPENDIX A – Correlations used

Correlation (source)	**Equation**
Friction factor (Churchill, 1977)	$$\frac{1}{f}=\left(\frac{1}{\left[\left(\frac{8}{Re}\right)^{10}+\left(\frac{Re}{36500}\right)^{20}\right]^{\frac{1}{2}}}+\left(2.21\ln\left(\frac{Re}{7}\right)\right)^{10}\right)^{\frac{1}{5}}$$ Adjustment for square channel geometry: $$Re_{lam}=Re\left[\frac{2}{3}+\frac{11}{24}\alpha\left(2-\alpha\right)\right]=57$$
Nusselt number – forced convection (Churchill, 1977)	$$\left(Nu\right)^{10}=\left(Nu_l\right)^{10}+\left[\frac{e^{\frac{(2200-Re)}{365}}}{\left(Nu_l\right)^2}+\left(\frac{1}{Nu_0+\frac{0.079Re\sqrt{f}\,Pr}{\left(1+Pr^{4/5}\right)^{5/6}}}\right)^2\right]^{-5}$$ $Nu_0=5.76$ for UWT

Sherwood number – forced convection (Churchill, 1977)	$Sh = Sh\left(Re, Sc\right)$ using the heat, mass, and momentum analogy $(Sh)^{10} = (Sh_l)^{10} + \left[\frac{e^{\frac{(2200-Re)}{365}}}{(Sh_l)^2} + \left(\frac{1}{Sh_0 + \frac{0.079 Re\sqrt{f}\,Sc}{\left(1+Sc^{4/5}\right)^{5/6}}} \right)^2 \right]^{-5}$
Free convection (McAdams, 1954)	Upper surface of hot plate, lower surface of cold plate: $Nu_L = 0.54 Ra_L^{1/4} \qquad \left(10^4 \le Ra_L < 10^7\right)$ $Nu_L = 0.15 Ra_L^{1/3} \qquad \left(10^7 < Ra_L \le 10^{11}\right)$ Lower surface of hot plate, upper surface of cold plate $Nu_L = 0.27 Ra_L^{1/4} \qquad \left(10^5 \le Ra_L \le 10^{10}\right)$
Free convection (Goldstein *et al.*, 1973)	$Sh = 0.960\left(Ra_m\right)^{1/6} \qquad 1 < Ra_m < 10^2$ $Sh = 0.590\left(Ra_m\right)^{1/4} \qquad 2\times10^2 < Ra_m < 8\times10^3$ $Ra_m = \frac{g\left(\rho_w - \rho_\infty\right)L^3}{\rho_\infty v^2} Sc$ Mass transfer Rayleigh number

Dual-Site Langmuir Equation (adsorbed equilibrium concentration) (Mathias *et al.*, 1996)	$C_{A,Eq,i} = \rho_{ads}\left(M_B \frac{B \cdot P_i}{1 + B \cdot P_i} + M_D \frac{D \cdot P_i}{1 + D \cdot P_i}\right)$ $B = b_0 \exp\left(\frac{-Q_B}{RT}\right) \qquad D = d_0 \exp\left(\frac{-Q_D}{RT}\right)$
Real gas equation of state (Peng and Robinson, 1976)	$P = \frac{RT}{V_m - b} - \frac{a\alpha}{{V_m}^2 + 2bV_m - b^2}$ $a = \frac{0.457235\, R^2 {T_c}^2}{P_c} \qquad b = \frac{0.077796\, R \cdot T_c}{P_c} \qquad T_r = \frac{T}{T_c}$ $\alpha = \left(1 + \kappa\left(1 - {T_r}^{0.5}\right)\right)^2 \qquad \kappa = 0.37464 + 1.54226\omega - 0.26992\omega^2$
Mixture viscosity (Pedersen and Fredenslund, 1984)	$\mu_{mix} = \frac{\sum_i C_i \mu_i \sqrt{M_i}}{\sum_i C_i \sqrt{M_i}}$

Appendix B – Sample calculations

B.1 – Incompressible flow modeling and literature predictions

Input	**Equations**	**Output**
Sample point calculations – 0.5 seconds after process start		
P_{avg} = 5450 kPa C_{CH4} = 0.7 mol mol^{-1} C_{CO2} = 0.1 mol mol^{-1} C_{H2S} = 0.2 mol mol^{-1} M_{CH4} = 16.04 kg mol^{-1} M_{CO2} = 44.01 kg mol^{-1} M_{H2S} = 34.08 kg mol^{-1} μ_{CH4} = 16.04 kg mol^{-1} μ_{CO2} = 44.01 kg mol^{-1} μ_{H2S} = 34.08 kg mol^{-1}	$\rho_{mixture} = \frac{P_{avg}\left(C_{CH_4}M_{CH_4} + C_{CO_2}M_{CO_2} + C_{H_2S}M_{H_2S}\right)}{R_U T}$	ρ_{mixture} = 50.68 kg m^{-3}
	$\mu_{mixture} = \frac{\sum C_n \mu_n \left(M_n\right)^{1/2}}{\sum C_n \left(M_n\right)^{1/2}} = 3.95\times10^{-5}\ \text{kg}\cdot\text{m}^{-1}\text{s}^{-1}$	μ_{mixture} = 3.95×10^{-5} m^{-1} s^{-1}
ΔP_{total} = 100 kPa e = 1×10^{-6} m	$Re_L = \frac{\rho_L v D_h}{\mu_L} = 30.3$	Re_L = 30.3

$D_h = 200\times10^{-6}$ m $\rho_L = 999.9$ kg m^{-3} $\rho_G = 50.68$ kg m^{-3} $x_i^{t=0} = 0$ m $x_i^t = 0.868$ m $v^{t=0} = 0$ m s^{-1} $v^t = 0.1517$ m s^{-1} $\Delta t = 0.01$ s	$f_L = f_{Churchill}\left(Re_L, e, D_h\right)$	$f_L = 2.133$
	$Re_G = \dfrac{\rho_G v D_h}{\mu_G} = 38.9$ $f_G = f_{Churchill}\left(Re_G, e, D_h\right)$	$Re_G = 38.9$ $f_G = 1.641$
	$\left(\dfrac{dP}{dx}\right)_L = f_L \dfrac{\rho_L\left(v^{t+\Delta t}\right)^2}{2D_h}$	$\left(\dfrac{dP}{dx}\right)_L = 123.4$ kPa m^{-1}
	$\left(\dfrac{dP}{dx}\right)_G = f_G \dfrac{\rho_G\left(v^{t+\Delta t}\right)^2}{2D_h}$	$\left(\dfrac{dP}{dx}\right)_L = 48.7$ kPa m^{-1}
	$\Delta P_{total}^{\ \ t+\Delta t} = \left(\dfrac{dP}{dx}\right)_L\left(x_i^t + v^{t+\Delta t}\cdot\Delta t\right) + \left(\dfrac{dP}{dx}\right)_G\left(L - \left(x_i^t + v^{t+\Delta t}\cdot\Delta t\right)\right)$	$v^{t+\Delta t} = 0.1521$
$u_G^S = 0.25$ m s^{-1} $u_G^S = 0.25$ m s^{-1} $\rho_L = 999.9$ kg m^{-3} $\rho_G = 50.68$ kg m^{-3}	$Bo = \dfrac{\left(\rho_L - \rho_G\right) g\cdot {D_h}^2}{\sigma}$	$Bo = 5.116\times10^{-3}$
	$Bo_{crit} = \left[\left(\dfrac{\rho_L}{\rho_L - \rho_G}\right) - \dfrac{\pi}{4}\right]^{-1}$ (Coleman and Garimella, 1999)	$Bo_{crit} = 3.731$

$g = 9.81$ m s^{-2} $D_h = 200\times10^{-6}$ m $\sigma = 7.28\times10^{-2}$ N m^{-1}	$We_G = \dfrac{\rho_G u_G^S D_h}{\sigma}$	$We_G = 0.0212$
	$X_{tt} = \sqrt{\dfrac{\Delta P_l}{\Delta P_g}} \approx \sqrt{\dfrac{\rho_l v^2}{\rho_g v^2}} = \dfrac{\dot{m}_l}{\dot{m}_g}\sqrt{\dfrac{\rho_g}{\rho_l}}$ (Nema, 2007)	$X_{tt} = 4.442$
	$X_{tt,slug} = \begin{cases} X_{tt} & \text{if} \quad Bo \le Bo_{crit} \\ X_{tt,0} + \dfrac{X_{tt}\left(Bo - Bo_{crit}\right)}{Bo - Bo_{crit} + e} & \text{if} \quad Bo > Bo_{crit} \end{cases}$	$X_{tt,slug} = 4.442$
	$X_{tt,mod} = X_{tt} - X_{tt,slug}$	$X_{tt,mod} = 0$

B.2 – Compressible flow modeling

Input	**Equations**	**Output**
Inlet state calculations		
C_{CH4} = 0.7 mol mol^{-1} C_{CO2} = 0.1 mol mol^{-1} C_{H2S} = 0.2 mol mol^{-1} P_i = 5500 kPa T_i = 23 °C	$\rho_i = \rho_{Peng-Robinson}\left(P_i, T_i, C_{CH_4,i}, C_{CO_2,i}, C_{H_2S,i}\right)$	ρ_i = 50.68 kg m^{-3}
	$\mu_i = \mu_{Peng-Robinson}\left(P_i, T_i, C_{CH_4,i}, C_{CO_2,i}, C_{H_2S,i}\right)$	μ_i = 3.95×10^{-5} Pa s
Sample point calculations – Node 2 of 50 at 0.01 seconds after process start		
ρ_i^{t-1} = 50.68 kg m^{-3} ρ_{i-1}^{t} = 50.68 kg m^{-3} ρ_{i+1}^{t} = 50.68 kg m^{-3} v_i^{t-1} = 2.139×10^{-2} m s^{-1} v_{i-1}^{t} = 2.447×10^{-2} m s^{-1} v_{i+1}^{t} = 2.448×10^{-2} m s^{-1}	$\frac{\partial \rho}{\partial t} = -\frac{\partial(\rho v)}{\partial x} + \frac{\dot{m}_{in}}{V_{CV}} \quad \rightarrow$ $\frac{\rho_i^t - \rho_i^{t-1}}{\Delta t} = -\frac{\rho_i^t v_i^t - \rho_{i-1}^t v_{i-1}^t}{\Delta x} + \frac{\dot{m}_i^t}{A_C \cdot \Delta x}$	v_i^t = 0.0245 m s^{-1} (by iteration)
	$\frac{\partial c_A}{\partial t} = -\frac{\partial(c_A v)}{\partial x} + \frac{\dot{m}_A}{V_{CV}} \quad \rightarrow$ $\frac{c_{A,i}^t - c_{A,i}^{t-1}}{\Delta t} = \frac{v_{i-1}^{t-1} c_{A,i-1}^{t-1} - v_{i+1}^{t-1} c_{A,i+1}^{t-1}}{\Delta x} + \frac{\dot{m}_{A,i}^t}{A_C \cdot \Delta x}$	$c_{CH_4,i}^t$ = 36.58 kg m^{-3} (by iteration) $c_{CO_2,i}^t$ = 10.54 kg m^{-3} (by iteration) $c_{H_2S,i}^t$ = 3.56 kg m^{-3} (by iteration)

$\Delta x^{t-\Delta t}$ = 0.0002 m $\Delta t = 0.01$ sec D_h = 2.03 ×10^{-4} m ε = 1×10^{-6} m	$Re_i^t = \dfrac{\rho_i^t v_i^t D_h}{\mu_i^t}$	Re_i^t = 6.287
	$f_i^t = f_{Churchill}\left(Re_i^t,\, \varepsilon,\, D_h\right)$	f_i^t = 10.17
	$-\dfrac{\partial P}{\partial x} = \dfrac{\partial(\rho v)}{\partial t} + v\dfrac{\partial(\rho v)}{\partial x} + f\,\dfrac{\rho v^2}{2D_h} \quad \rightarrow$ $-\left(\dfrac{P_i^t - P_{i-1}^t}{\Delta x}\right) = \dfrac{\rho_i^t v_i^t - \rho_i^{t-1} v_i^{t-1}}{\Delta t} + \dfrac{\rho_{i+1}^t v_{i+1}^t - \rho_{i-1}^t v_{i-1}^t}{2\Delta x} + f_i^t\,\dfrac{\rho_i^t \left(v_i^t\right)^2}{2D_h}$	P_i^t = 5499.99 kPa (by iteration)
	$\rho_i^t = \rho_{Peng-Robinson}\left(P_i^t\,,\, c_{CH_4,i}^t\,,\, c_{CO_2,i}^t\,,\, c_{H_2S,i}^t\right)$	ρ_i^t = 50.68 kg m^{-3}
	$X_{A,i}^t = \dfrac{c_{A,i}^t}{\rho_i^t}$	$X_{CH_4,i}^t$ = 0.72 kg kg^{-1} $X_{CO_2,i}^t$ = 0.21 kg kg^{-1} $X_{H_2S,i}^t$ = 0.07 kg kg^{-1}
	$C_{A,i}^t = \dfrac{X_{A,i}^t M_C + \dfrac{X_{A,i}^t X_{B,i}^t M_C \left(M_B - M_C\right)}{M_B - X_{B,i}^t\left(M_B - M_C\right)}}{M_A - X_{A,i}^t\left(M_A - M_C\right) - \dfrac{X_{A,i}^t X_{B,i}^t \left(M_A - M_C\right)\left(M_B - M_C\right)}{M_B - X_{B,i}^t\left(M_B - M_C\right)}}$	$C_{CH_4,i}^t$ = 0.70 mol mol^{-1} $C_{CH_4,i}^t$ = 0.10 mol mol^{-1} $C_{CH_4,i}^t$ = 0.20 mol mol^{-1}
$v_{N_x-1}^t$ = 2.448×10^{-2} m s^{-1}	$v_L^t = v_{N_x-1}^t$	v_L^t = 2.448×10^{-2} m s^{-1} (by iteration)

	$\frac{\partial L_G}{\partial t} = v_L$	L_G^t = 0.027 m (by iteration)
N_x = 50	$\Delta x^t = \frac{L_G}{N_x}$	Δx^t = 0.00055 m

B.3 – Heat and mass transfer modeling

Input	**Equations**	**Output**
Sample point calculations – 0.05 m from channel inlet, 0.01 seconds after process start		
M_{CH4} = 16.04 kg mol^{-1} M_{CO2} = 44.01 kg mol^{-1} M_{H2S} = 34.08 kg mol^{-1} $c^t_{g,CH_4,i-1}$ = 28.5 kg m^{-3} $c^t_{g,CH_4,i+1}$ =38.7 kg m^{-3} $c^{t-\Delta t}_{g,CH_4,i}$ = 38.8 kg m^{-3} $c^t_{g,CO_2,i-1}$ = 36.91 kg m^{-3} $c^t_{g,CO_2,i+1}$ = 1×10^{-4} kg m^{-3} $c^{t-\Delta t}_{g,CO_2,i}$ = 0.791 kg m^{-3} P^t_{i-1} = 5500 kPa	$\frac{\partial c_{g,i}}{\partial t} + u\frac{\partial c_{g,i}}{\partial z} = -h_{m,conv}\frac{Per}{A_{CS}}\left(c_{g,i} - c_{w,i}\right) \rightarrow$ $\frac{c^t_{g,A,i} - c^{t-\Delta t}_{g,A,i}}{\Delta t} + v^t_i\frac{c^t_{g,A,i+1} - c^t_{g,A,i-1}}{\Delta z} = -h_{m,conv}\frac{Per}{A_{CS}}\left(c^t_{g,A,i} - c^t_{w,A,i}\right)$	$c^t_{g,CH_4,i}$ = 38.76 kg m^{-3} (by iteration) $c^t_{g,CO_2,i}$ = 1.16×10^{-4} kg m^{-3} (by iteration) $v^t_{g,i}$ = 4.32 m s^{-1} (by iteration)
	$\rho^t_{g,i} = \rho_{Peng-Robinson}\left(P^t_i\,,\, C^t_{CH_4,i}\,,\, C^t_{CO_2,i}\,,\, C^t_{H_2S,i}\right)$	$\rho^t_{g,i}$ = 39.6 kg m^{-3}
	$X^t_{g,A,i} = \frac{c^t_{A,i}}{\rho^t_i}$	$X^t_{g,CH_4,i}$ = 0.999 kg kg^{-1} $X^t_{g,CO_2,i}$ = 2.99 × 10^{-6} kg kg^{-1}
	$C^t_{g,A,i} = \frac{X^t_{A,i}M_C + \frac{X^t_{A,i}X^t_{B,i}M_C\left(M_B - M_C\right)}{M_B - X^t_{B,i}\left(M_B - M_C\right)}}{M_A - X^t_{A,i}\left(M_A - M_C\right) - \frac{X^t_{A,i}X^t_{B,i}\left(M_A - M_C\right)\left(M_B - M_C\right)}{M_B - X^t_{B,i}\left(M_B - M_C\right)}}$	$C^t_{g,CH_4,i}$ = 0.999 kg kg^{-1} $C^t_{g,CO_2,i}$ = 1.0 × 10^{-6} mol mol^{-1}

P_{i+1}^{t} = 5490 kPa $T_{g,i-1}^{t}$ = 25.09 °C $T_{g,i+1}^{t}$ = 25.08 °C $T_{g,i}^{t-\Delta t}$ = 24.85 °C $c_{CH_4,i-1,j}^{t}$ = 28.51 kg m^{-3} $c_{CH_4,i+1,j}^{t}$ = 38.76 kg m^{-3} $c_{CH_4,i,j-1}^{t}$ = 38.77 kg m^{-3} $c_{CH_4,i,j+1}^{t}$ = 38.77 kg m^{-3} $c_{CH_4,i,j}^{t-\Delta t}$ = 38.72 kg m^{-3} $c_{CO_2,i-1,j}^{t}$ = 36.91 kg m^{-3} $c_{CO_2,i+1,j}^{t}$ = 1×10^{-4} kg m^{-3} $c_{CO_2,i,j-1}^{t}$ = 0.791 kg m^{-3} $c_{CO_2,i,j+1}^{t}$ = 0.789 kg m^{-3}	$\rho u\frac{\partial u}{\partial z}-\sum\dot{S}_i'''u=-\frac{\partial P}{\partial z}+\frac{4}{3}\mu\frac{\partial^2 u}{\partial z^2}-f\frac{\rho u^2}{2D_h}\rightarrow$ $\rho_i^t u_i^t\frac{\rho_{i+1}^t u_{i+1}^t-\rho_{i-1}^t u_{i-1}^t}{\Delta z}-\sum\dot{S}_i^t{}'''u_i^t=$ $-\frac{P_{i+1}^t-P_{i-1}^t}{\Delta z}+\frac{4}{3}\mu_i^t\frac{\rho_{i+1}^t u_{i+1}^t-2\rho_i^t u_i^t+\rho_{i-1}^t u_{i-1}^t}{\left(\Delta z\right)^2}-f_i^t\frac{\rho_i^t\left(u_i^t\right)^2}{2D_h}$	P_i^t = 5495 kPa
	$\rho_g c_{p,g}\frac{\partial T_g}{\partial t}+\rho_g c_{p,g}u\frac{\partial T_g}{\partial z}=-h_{T,conv}\frac{Per}{A_{cs}}\left(T_g-T_w\right)\rightarrow$ $\rho_{g,i}^t c_{p,g,i}^t\frac{T_{g,i}^t-T_{g,i}^{t-\Delta t}}{\Delta t}+\rho_{g,i}^t c_{p,g,i}^t u_i^t\frac{T_{g,i+1}^t-T_{g,i-1}^t}{\Delta z}=-h_{T,conv}\frac{Per}{A_{cs}}\left(T_{g,i}^t-T_{w,i}^t\right)$	$T_{g,i}^t$ = 25.05 °C (by iteration)
	$\frac{\partial c_{w,i}}{\partial t}+\frac{\omega}{\varepsilon}\frac{\partial c_{Ads,i}}{\partial t}=D\nabla^2 c_{w,i}\rightarrow$ $\frac{c_{w,A,i,j}^t-c_{w,A,i,j}^{t-\Delta t}}{\Delta t}+\frac{\omega}{\varepsilon}\frac{c_{Ads,A,i,j}^t-c_{Ads,A,i,j}^{t-\Delta t}}{\Delta t}=$ $D\left[\left(\frac{c_{w,A,i+1,j}^t-2c_{w,A,i,j}^t+c_{w,A,i+1,j}^t}{\left(\Delta z\right)^2}\right)+\frac{1}{r}\left(\frac{c_{w,A,i,j+1}^t-2c_{w,A,i,j}^t+c_{w,A,i,j-1}^t}{\left(\Delta r\right)^2}\right)\right]$	$c_{w,CH_4,i,j}^t$ = 38.77 kg m^{-3} (by iteration) $c_{w,CO_2,i,j}^t$ = 0.79 kg m^{-3} (by iteration)
	$\rho_{i,j}^t=\rho_{Peng-Robinson}\left(P_{i,j}^t,\ C_{CH_4,i,j}^t,\ C_{CO_2,i,j}^t,\ C_{H_2S,i,j}^t\right)$	$\rho_{i,j}^t$ = 39.559 kg m^{-3} (by iteration)

$c^{t-\Delta t}_{CO_2,i,j} = 0.791$ kg m^{-3} $T^t_{i-1,j} = 24.85$ °C $T^t_{i+1,j} = 25.05$ °C $T^t_{i,j+1} = 25.05$ °C $T^t_{i+1,j} = 25.05$ °C $T^{t-\Delta t}_{i,j} = 24.85$ °C $D = 8.21\times10^{-6}$ m^2 s $k_m = 64$ W m^{-1} K^{-1} $\Delta h_{ads,CO_2} = 36$ kJ mol^{-1} $h_{T,conv} = 7887$ W m^{-2} K	$X^t_{A,i,j} = \frac{c^t_{A,i,j}}{\rho^t_{i,j}}$	$X^t_{CH_4,i,j} = 0.980$ kg kg^{-1} $X^t_{CO_2,i,j} = 0.020$ kg kg^{-1}
	$C^t_{A,i,j} = \frac{X^t_{A,i,j}M_C + \frac{X^t_{A,i,j}X^t_{B,i,j}M_C\left(M_B-M_C\right)}{M_B - X^t_{B,i,j}\left(M_B-M_C\right)}}{M_A - X^t_{A,i,j}\left(M_A-M_C\right) - \frac{X^t_{A,i,j}X^t_{B,i,j}\left(M_A-M_C\right)\left(M_B-M_C\right)}{M_B - X^t_{B,i,j}\left(M_B-M_C\right)}}$	$C^t_{CH_4,i,j} = 0.993$ mol mol^{-1} $C^t_{CO_2,i,j} = 7.38\times10^{-3}$ mol mol^{-1}
	$\dot{m}''_{z,CO_2,i,j} = D\left(\frac{c^t_{w,CO_2,i-1,j} - c^t_{w,CO_2,i+1,j}}{\Delta z}\right)$ $\dot{m}''_{r,CO_2,i,j} = \frac{1}{r}D\left(\frac{c^t_{w,CO_2,i-1,j} - c^t_{w,CO_2,i+1,j}}{\ln\left(r+\Delta r/r\right)}\right)$	$\dot{m}''_{z,CO_2,i,j} = 6.06\times10^{-3}$ kg m^{-2} s^{-1} $\dot{m}''_{r,CO_2,i,j} = 8.88\times10^{-4}$ kg m^{-2} s^{-1}
	$C^t_{ads,A,i,j} = C_{EQ,Langmuir}\left(T^t_{i,j},\ P^t_{i,j}\right)$	$C^t_{ads,CO_2,i,j} = 4950.1$ mol m^{-3}

$c_{p,m}$ = 1108 J kg^{-1} K^{-1} ω = 0.211 f = 0.06 Δz = 0.05 m $\Delta r = 2 \times 10^{-5}$ m Δt = 0.01 sec	$\rho_m c_{p,m}\frac{\partial T}{\partial t} = k_m \nabla^2 T + \sum \omega \cdot h_{ads,A,i}\frac{\partial c_{Ads,A}}{\partial t} \quad \rightarrow$ $\rho^t_{i,j} c^t_{p,i,j}\frac{T^t_{i,j} - T^{t-\Delta t}_{i,j}}{\Delta t} = k_m \left[\left(\frac{T^t_{i+1,j} - 2T^t_{i,j} + T^t_{i-1,j}}{(\Delta z)^2} \right) + \frac{1}{r}\left(\frac{T^t_{i,j+1} - 2T^t_{i,j} + T^t_{i,j-1}}{(\Delta r)^2} \right) \right]$ $+\sum \omega \cdot h_{ads,A,i}\left(\frac{c^t_{Ads,A,i,j} - c^{t-\Delta t}_{Ads,A,i,j}}{\Delta t} \right)$	$T^t_{i,j}$ = 25.15 °C (by iteration)
	$q''_{z,i,j} = k\left(\frac{T^t_{i-1,j} - T^t_{i+1,j}}{\Delta z} \right)$ $q''_{r,i,j} = \frac{1}{r}k\left(\frac{T^t_{i-1,j} - T^t_{i+1,j}}{\ln\left(r + \Delta r / r \right)} \right)$ $q'''_{ads,i,j} = \frac{dC_{Ads,i,j}}{dx}\Delta h_{ads}$	$q''_{z,i,j}$ = 256.0 W m^{-2} K^{-1} $q''_{r,i,j}$ = 380.6 W m^{-2} K^{-1} $q'''_{ads,i,j} = 4.68 \times 10^6$ W m^{-3} K^{-1}

B.4 – Void fraction and film thickness calculations

Input	Equations	Output
$D_h = 2.03 \times 10^{-4}$ m $D_{g,i} = 1.72 \times 10^{-4}$ m $t_{f,upper} = 1.0 \times 10^{-5}$ m $H = -9.13 \times 10^{-5}$ m $L_V = 1.62 \times 10^{-3}$ m $V_g = 4.79 \times 10^{-11}$ m^3	$A_{cs,i} = \frac{\pi}{4} D_{g,i}^{\ 2}$	$A_{cs} = 2.32 \times 10^{-8}$ m
	$R_{reduced} = \frac{D_{tube}}{2} - t_{f,upper}$	$R_{reduced} = 9.15 \times 10^{-5}$ m
	$\theta = 2\arccos\left(\frac{H}{R_{reduced}}\right)$	$\theta = 7.58°$
	$A_{cs,g,i} = \begin{cases} \frac{1}{2} R_{reduced}^{\ 2}\left(\theta - \sin(\theta)\right) & H > 0 \\ \frac{1}{2} R_{reduced}^{\ 2}\left(2\pi - \theta - 2\sin(\theta)\right) & H < 0 \end{cases}$	$A_{cs,i} = 1.32 \times 10^{-8}$ m
	$\alpha_{center} = \frac{4A_{cs,g,i}}{\pi D_h^{\ 2}}$	$\alpha_{center} = 0.569$
	$\alpha = \frac{4V_g}{\pi D_h^{\ 2} L_v}$	$\alpha = 0.914$
	$t_f = \frac{D_h}{2}\left(1 - \sqrt{\alpha}\right)$	$t_f = 4.49 \times 10^{-6}$ m

REFERENCES

Aaron, D. and C. Tsouris (2011), "Separation of Co2 from Flue Gas: A Review," *Separation Science and Technology* Vol. 40 pp. 321-348.

Abatzoglou, N. and S. Boivin (2009), "A Review of Biogas Purification Processes," *Biofuels, Bioproducts, and Biorefining* Vol. 3 pp. 42-71.

Baker, R. W. (2002), "Future Directions of Membrane Gas Separation Technology," *Industrial & Engineering Chemical Research*(41) pp. 1393-1411.

Barajas, A. M. and R. L. Panton (1993), "The Effects of Contact Angle on Two-Phase Flow in Capillary Tubes," *International Journal of Multiphase Flow* Vol. 19(2) pp. 337-346.

Barnea, D., Y. Luninski and Y. Taitel (1983), "Flow Pattern in Horizontal and Vertical Two-Phase Flow in Small Diameter Tubes," *Canadian Journal of Chemical Engineering* Vol. 61(5) pp. 617-620.

Bernardo, P., E. Drioli and G. Golemme (2009), "Membrane Gas Separation: A Review/State of the Art," *Industrial & Engineering Chemical Research* Vol. 48 pp. 4638-4663.

Bhide, B. D., A. Voskericyan and S. A. Stem (1998), "Hybrid Processes for the Removal of Acid Gas from Natural Gas," *Journal of Membrane Science* Vol. 140(1) pp. 27-49.

Canny, J. (1986), "A Computational Approach to Edge Detection," *IEEE Trans. Pattern Analysis and Machine Intelligence* Vol. 8(6) pp. 679-698.

Cavenati, S., C. A. Grande and A. E. Rodriques (2004), "Adsorption Equilibrium of Methane, Carbon Dioxide, and Nitrogen on Zeolite 13x at High Pressures," *Journal of Chemical Engineering Data*(49) pp. 1095-1101.

Cen, P.-L., W.-N. Chen and R. T. Yang (1985), "Ternary Gas Mixture Separation by Pressure Swing Adsorption: A Combined Hydrogen-Methane Separation and Acid Gas Removal Process," *Industrial & Engineering Chemistry Process Design and Development*(24) pp. 1201-1208.

Chakma, A. and P. Tontiwachwuthikul (1999), "Co2 Separation from Combustion Gas Streams by Chemically Reactive Solvents," *Online Library: Combustion Canada*.

Chapel, D., J. Ernest and C. Mariz (1999), "Recovery of Co2 from Flue Gases: Commercial Trends," *Canadian Society of Chemical Engineers Annual Meeting*, Saskatchewan, Canada

Chung, P. M. Y. and M. Kawaji (2004), "The Effect of Channel Diameter on Adiabatic Two-Phase Flow Characteristics in Microchannels," *International Journal of Multiphase Flow* Vol. 30 pp. 735-761.

Chung, P. M. Y., M. Kawaji, A. Kawahara and Y. Shibata (2004), "Two-Phase Flow through Square and Circular Microchannels- Effects of Channel Geometry," *Transactions of the ASME* Vol. 126 pp. 546-552.

Churchill, S. W. (1977), "Comprehensive Correlating Equations for Heat, Mass, and Momentum Transfer in Fully Developed Flow in Smooth Tubes," *Industrial & Engineering Chemistry Fundamentals* Vol. 16(1) pp. 109-116.

Coleman, J. and S. Garimella (1999), "Characterization of Two-Phase Flow Patterns in Small Diameter Round and Rectangular Tubes," *International Journal of Heat and Mass Transfer* Vol. 42 pp. 2869-2881.

Cubaud, T. and C. Ho (2004), "Transport of Bubbles in Square Microchannels," *Physics of Fluids* Vol. 16(12).

Damianides, C. and J. Westwater (1988), "Two-Phase Flow Patterns in a Compact Heat Exchanger and in Small Tubes," *Second UK National Conference on Heat Transfer*, Glasgow, Scotland, pp. 1257-1268.

Determan, M. D., D. C. Hoysall, S. Garimella, R. Lenz and D. P. Leta (2012), "Carbon Dioxide Capture Using Sorbent-Loaded Hollow Fiber Modules with Integrated Heat Recovery (in Preparation)."

Engineering, O. (2012). *Omega-Flo 2-Way High Pressure Solenoid Valves*. I. Omega Engineering. Stamford, CT.

Fukano, T. (1998), "Measurement of Time Varying Thickness of Liquid Film Flowing with High Speed Gas Flow by a Constant Electric Current Method (Cecm)," *Nuclear Engineering and Design* Vol. 184 pp. 363-377.

Fukano, T. and A. Kariyasaki (1993), "Characteristics of Gas-Liquid Two-Phase Flow in a Capillary Tube," *Nuclear Engineering and Design*(141) pp. 59-68.

Fukano, T. and A. Ousaka (1989), "Prediction of the Circumferential Distribution of Film Thickness in Horizontal and near Horizontal Gas-Liquid Annular Flows," *International Journal of Multiphase Flow* Vol. 15(3) pp. 403-419.

Ghiaasiaan, S. M. (2008). *Two-Phase Flow, Boiling, and Condensation in Conventional and Miniature Systems*. 1st Ed. New York, NY, Cambridge University Press.

Goldstein, R., E. Sparrow and D. Jones (1973), "Natural Convection Mass Transfer Adjacent to Horizontal Plates," *International Journal of Heat and Mass Transfer* Vol. 16 pp. 1025-1035.

Gottlicher, G. and R. Pruschek (1997), "Comparison of Co2 Removal Systems for Fossil Fuel Power Plant Processes," *Energy Conversion and Management* Vol. 38(Suppl.) pp. S173-S178.

Griffith, P. and G. B. Wallis (1961), "Two-Phase Slug Flow," *Journal of Heat Transfer* Vol. 83(307).

Hines, A. and R. Maddox (1985). *Mass Transfer Fundamentals and Applications*. Upper Saddle River, NJ, USA, Prentice-Hall.

Hirschfelder, J., R. Bird and E. Spotz (1949), "The Transport Properties of Gases and Gaseous Mixtures Ii," *Chemical Reviews* Vol. 44(1) pp. 205-231.

Hu, E. J., D. S. Zhu, X. Y. Sang, L. Wang and Y. K. Tan (1997), "Enhancement of Thermal Conductivity by Using Polymer-Zeolite in Solid Adsorption Heat Pumps," *Journal of Heat Transfer* Vol. 119(3) pp. 627-630.

Ide, H., H. Matsamura and T. Fukano (1995), "Velocity Characteristics of Liquid Lumps and Its Relation to Flow Patterns in Gas-Liquid Two-Phase Flow in Vertical Capillary Tubes," *ASME/JSME Fluids Engineering and Laster Anemometry Coference and Exhibition*, Hilton Head, SC

Kandlikar, S., S. Garimella, D. Li, S. Colin and M. King (2006). *Heat Transfer and Fluid Flow in Minichannels and Microchannels*. 1 Ed. Oxford, Elsevier Ltd.

Kapoor, A. and R. T. Yang (1989), "Kinetic Separation of Methane-Carbon Dioxide Mixture by Adsorption on Molecular Sieve Carbon," *Chemical Engineering Science* Vol. 44(8) pp. 1723-1733.

Kawahara, A., P. Chung, M. Kawaji (2002), "Investigation of Two-Phase Flow Pattern, Void Fraction, and Pressure Drop in a Microchannel," *International Journal of Multiphase Flow* Vol. 28 pp. 1411-1435.

Kawahara, A., M. Sadatomi, K. Okayama, M. Kawaji, P. M. Y. Chung and R. W. Baker (2005), "Effects of Channel Diameter and Liquid Properties on Void Fraction in Adiabatic Two-Phase Flow through Microchannels," *Heat Transfer Engineering* Vol. 26(3) pp. 13-19.

Kawaji, M. and P. M. Y. Chung (2004), "Adiabatic Gas-Liquid Flow in Microchannels," *Microscale Thermophysical Engineering* Vol. 8(3) pp. 239-257.

Keinath, B. and S. Garimella (2010), "Bubble and Film Dynamics During Condensation of Refrigerants in Minichannels," *International Heat Transfer Conference*, Washington, DC, USA

Kew, P. and K. Cornwell (1997), "Correlations for the Prediction of Boiling Heat Transfer in Small-Diameter Channels," *Applied Thermal Engineering* Vol. 17 pp. 705-715.

Killion, J. D. and S. Garimella (2004), "Pendant Droplet Motion for Absorption on Horizontal Tube Banks," *International Journal of Heat and Mass Transfer* Vol. 47(19-20) pp. 4403-4414.

Klein, S. (1992-2012). *Engineering Equation Solver*, F-Chart Software.

Koros, W. J. and R. Mahajan (2000), "Pushing the Limits on Possibilities for Large Scale Gas Separation: Which Strategies?," *Journal of Membrane Science*(175) pp. 181-196.

Li, G., P. Xiao and P. Webley (2009), "Competition of Co2/H2o in Adsorption Based Co2 Capture," *Energy Procedia* Vol. 1(1) pp. 1123-1130.

Lively, R. P., M. E. Dose, L. Xu, J. T. Vaughn, J. R. Johnson, J. A. Thompson, K. Zhang, M. E. Lydon, J.-S. Lee, L. Liu, Z. Hu, O. Karvan, M. J. Realff and W. J. Koros (2012), "A High-Flux Polyimide Hollow Fiber Membrane to Minimize Footprint and Energy Penalty for Co2 Recovery from Flue Gas," *Journal of Membrane Science* Vol. [online only].

Lively, R. P., J. A. Mysona, R. R. Chance and W. J. Koros (2011), "Formation of Defect-Free Latex Films on Porous Fiber Supports," *ACS Applied Materials and Interfaces* Vol. 3(9) pp. 3568-3582.

Mandhane, J. M., G. A. Gregory and K. Aziz (1974), "A Flow Pattern Map for Gas-Liquid Flow in Horizontal Pipes," *International Journal of Multiphase Flow* Vol. 1 pp. 537-553.

Mathias, P. M., R. Kumar, J. J. Douglas Moyer, J. M. Schork, S. R. Srinivasan, S. R. Auvil and O. Talu (1996), "Correlation of Multicomponent Gas Adsorption by the Dual-Site Langmuir Model. Application to Nitrogen/Oxygen Adsorption on 5a-Zeolite," *Industrial & Engineering Chemical Research* Vol. 35(7) pp. 2477-2483.

McAdams, W. (1954). *Heat Transmission*. 3rd Ed. New York, McGraw Hill.

Miles, D. J., D. M. Sanborn, G. A. Nowakowski and S. V. Shelton (1993), "Gas Fired Sorption Heat Pump Development," *Heat Recovery Systems & CHP* Vol. 13(4) pp. 347-351.

Mishima, K. and T. Hibiki (1996), "Some Characteristics of Air-Water Two-Phase Flow in Small Diameter Vertical Tubes," *International Journal of Multiphase Flow* Vol. 22(4) pp. 703-712.

Mishima, K. and M. Ishii (1984), "Flow Regime Transition Criteria for Two-Phase Flow in Vertical Tubes," *International Journal of Heat and Mass Transfer* Vol. 27(5) pp. 723-737.

Nema, G. (2007). *Flow Regime Transitions During Condensation in Microchannels*. Mechanical Engineering. Atlanta, GA, Georgia Institute of Technology p. 129.

Olajossy, A., A. Gawdzik, Z. Budner and J. Dula (2003), "Methane Separation from Coal Mine Methane Gas by Vacuum Pressure Swing Adsorption," *Chemical Engineering Research and Design* Vol. 81(4) pp. 474-481.

Parkera, M. E., S. Northropb, J. A. Valenciab, R. E. Foglesonga and W. T. Duncana (2011), "Co2 Management at Exxonmobil's Labarge Field, Wyoming, USA," *Energy Procedia* Vol. 4 pp. 5455–5470.

Pedersen, K. S. and A. Fredenslund (1984), "Viscosity of Crude Oils," *Chemical Engineering Science* Vol. 39(6) pp. 1011-1016.

Peng, D. Y. and D. Robinson (1976), "A New Two-Constant Equation of State," *Industrial & Engineering Chemical Fundamentals* Vol. 15(1) pp. 59-64.

Pons, M. (1997), "Global Analysis of Refrigerative Adsorption Cycles with Thermal Regeneration," *International Journal of Refrigeration* Vol. 20(6) pp. 411-420.

Process Systems Enterprise, I. (1997-2009). *Gproms*, Process Systems Enterprise.

Riemer, P. W. F., I. C. Webster, W. G. Omerod and H. Audus (1994), "Results and Full Fuel Cycle Study Plans from the Iea Greenhouse Gas Research and Development Programme," *Fuel* Vol. 73(7).

Ritter, J. A. and R. T. Yang (1991), "Pressure Swing Adsorption: Experimental and Theoretical Study on Air Purification and Vapor Recovery," *Industrial & Engineering Chemical Research* Vol. 30(5) pp. 1023-1032.

Robinson, D. B., D.-Y. Peng and S. Y.-K. Chung (1985), "The Development of the Peng - Robinson Equation and Its Application to Phase Equilibrium in a System Containing Methanol," *Fluid Phase Equilibria* Vol. 24(1-2) pp. 25-41.

Serizawa, A., Z. Feng and Z. Kawara (2002), "Two-Phase Flow in Microchannels," *Experimental Thermal and Fluid Science* Vol. 26 pp. 703-714.

Tabatabai, A. and A. Faghri (2001), "A New Two-Phase Flow Map and Transition Boundary Accounting for Surface Tension Effects in Horizontal Miniature and Micro Tubes," *Journal of Heat Transfer* Vol. 123(5) pp. 958-969.

Taitel, Y. and D. Barnea (1982), "Counter-Current Gas-Liquid Vertical Flow: Model for Flow Pattern and Pressure Drop," *International Journal of Multiphase Flow* Vol. 9(6) pp. 637-647.

Taitel, Y., D. Barnea and A. E. Dukler (1980), "Modeling Flow Pattern Transitions for Steady Upward Gas-Liquid Flow in Vertical Tubes," *AIChE Journal* Vol. 26 pp. 345-354.

Taitel, Y. and A. E. Dukler (1976), "A Model for Predicting Flow Regime Transitions in Horizontal and near-Horizontal Gas-Liquid Flow," *AIChE Journal* Vol. 22 pp. 47-55.

Tamimi, A., E. Rinker and O. Sandall (1994), "Diffusion Coefficients for Hydrogen Sulfide, Carbon Dioxide, and Nitrous Oxide in Water over the Temperature Range 293-368 K," *Journal of Chemical Engineering Data* Vol. 39 pp. 330-332.

Thome, J. R., V. Duponta and A. M. Jacobi (2004), "Heat Transfer Model for Evaporation in Microchannels. Part I: Presentation of the Model," *International Journal of Heat and Mass Transfer* Vol. 47(14-16) pp. 3375-3385.

Weisman, J., D. Duncan, J. Gibson and T. Crawford (1979), "Effects of Fluid Properties and Pipe Diameter on Two-Phase Flow Patterns in Horizontal Tubes," *International Journal of Multiphase Flow* Vol. 5 pp. 437-462.

Wong, Y. L., D. C. Groenveld and S. C. Cheng (1990), "Chf Prediction for Horizontal Tubes," *International Journal of Multiphase Flow* Vol. 16(1) pp. 123-138.

Xu, J. L., P. Cheng and T. S. Zhao (1999), "Gas-Liquid Two-Phase Flow Regimes in Rectangular Channels with Mini/Micro Gaps," *International Journal of Multiphase Flow* Vol. 25 pp. 411-432.

Yang, H., Z. Xu, M. Fan, R. Gupta, R. B. Slimane, A. E. Bland and I. Wright (2008), "Progress in Carbon Dioxide Separation and Capture: A Review," *Journal of Environmental Sciences*(20) pp. 14-27.

Zhao, T. S. and Q. C. Bi (2001), "Co-Current Air-Water Two-Phase Flow Patterns in Vertical Triangular Microchannels," *International Journal of Multiphase Flow* Vol. 27 pp. 765-782.